

MICROHARDNESS, STRENGTH AND STRAIN FIELD CHARACTERIZATION  
OF SELF-REACTING FRICTION STIR AND PLUG WELDS  
OF DISSIMILAR ALUMINUM ALLOYS

by

KARLA RENEE HORTON

A DISSERTATION

Submitted in partial fulfillment of the requirements  
for the degree of Doctor of Philosophy in the  
Department of Interdisciplinary Studies  
in the Graduate School of  
The University of Alabama

TUSCALOOSA, ALABAMA

2011

Copyright Karla Renee Horton 2011  
ALL RIGHTS RESERVED

## **ABSTRACT**

Friction stir welding (FSW) is a solid state welding process with potential advantages for aerospace and automotive industries dealing with light alloys. Self-reacting friction stir welding (SR-FSW) is one variation of the FSW process being developed at the National Aeronautics and Space Administration (NASA) for use in the fabrication of propellant tanks. Friction plug welding is used to seal the exit hole that remains in a circumferential SR-FSW. This work reports on material properties and strain patterns developed in a SR-FSW with a friction plug weld. Specifically, this study examines the behavior of a SR-FSW formed between an AA 2014-T6 plate on the advancing side and an AA 2219-T87 plate on the retreating side and a SR-FSW (AA 2014-T6 to AA 2219-T87) with a 2219-T87 plug weld. This study presents the results of a characterization of the micro-hardness, joint strength, and strain field characterization of SR-FSW and FPW joints tested at room temperature and cryogenic temperatures.

The initial weld microstructure analysis showed a nugget region with fine grains and a displaced weld seam from the advancing side past the thermo-mechanical affected zone (TMAZ) into the nugget region. The displaced material shared the same hardness as the parent material. Dynamic recrystallization was observed in the SR-FSW zone and the displaced weld seam region. The welds revealed a fine grain structure in the SR-FSW zone with a sharp demarcation seen on the advancing side and fairly diffuse flow observed on the retreating side. The parent material hardness is 145 HV<sub>700g</sub> with a drop in hardness starting at the HAZ to 130 HV<sub>700g</sub>. The

hardness further drops in the TMAZ to 118 HV<sub>700g</sub> with an increase representing a dispersed interface of AA 2014-T6 material to 135 HV<sub>700g</sub>. The hardness then drops significantly within the nugget region to 85 HV<sub>700g</sub> followed by an increase through the retreating side TMAZ into the HAZ to 135 HV<sub>700g</sub>. There was a sharp increase in the hardness value within the nugget region with the samples that were post weld heat treated (PWHT) showing an increase of 58%.

The welded joints were tested for ultimate strength. The testing variations included two specimen widths, two plug sizes (M3 and M5), room temperature and cryogenic testing, and post weld heat treated (PWHT) samples. Initial welds had an average ultimate strength of 370 MPa with a slight drop from initial weld strength to plug weld strength of ranging from 13.8 to 20.7 MPa. The M3 plug strength was approximately equal to M5 plug strength. The PWHT strengths at room temperature were slightly higher than non-PWHT strengths, ranging from 13.8-20.7 MPa and PWHT strengths were equal to non-PWHT at cryogenic temperature. Non-PWHT had a cryogenic strength enhancement approximately 59.2 MPa and PWHT had a cryogenic strength enhancement of approximately 57.2 MPa in the M3 and M5 plugs. Within the subsets of data collected no major statistical significance in strength behavior was observed between the samples tested at room temperature or between the subsets tested at cryogenic temperature.

In almost all cases, failure occurred on the retreating side of the weld which corresponds to the softer material (AA 2219-T87). Exceptions were characterized with flaws (weld defects) in the sample. In these cases, failure occurred on the advancing side, the side where flaws were detected. Ductile fracture was noted in most all samples.

Digital image correlation using the ARAMIS system was used to define strain patterns in the weld joint. Strain accumulation was observed in the weld along the retreating side and

around the plug. ARAMIS data in comparison to extensometer data shows a very reasonable comparison. The ARAMIS strain gage data showed the retreating side of the major diameter has a greater yield than the advancing side. This behavior is identical to the external electrical resistance strain gages.

## **DEDICATION**

This dissertation is dedicated to those who came before me, those who will come after me and those who helped me, guided me, and supported me through my trials and tribulations as I have pursued a life of endless possibilities. In particular, I would like to thank my children, parents and close friends who stood by me through this difficult time, by making my life stress-free, worry-free, and even on occasion, dog-free. I love each and every one of you for your support and for traveling this journey with me. Lastly, I dedicate this to my future. *Laissez les bons temps rouler!*

In Memory of Alexis Antonia Roberts  
June 24, 1980 – March 22, 2011

## LIST OF ABBREVIATIONS AND SYMBOLS

$A_0$	Initial cross-sectional area
AA	Aluminum alloy
C-FSW	Conventional friction stir weld
$\Delta L$	Change in gage length
DRV	Dynamic recovery
DRX	Dynamic recrystallization
$E$	Young's modulus
$\varepsilon$	Engineering strain
$F$	Tensile force
FSW	Friction Stir Weld
HAZ	Heat affected zone
$L_0$	Initial gage length
MSFC	Marshall Space Flight Center
NASA	National Aeronautics and Space Administration
NDE	Nondestructive evaluation
PDS	Process Development System
SEM	Scanning electron microscopy
$\sigma$	Engineering stress
SR-FSW	Self reacting friction stir weld
TMAZ	Thermo-mechanically affected zone

TWI The Welding Institute

VHN Vickers hardness



## **ACKNOWLEDGMENTS**

I am pleased to have this opportunity to thank the many colleagues, friends, and faculty members who have helped me with this research project. I am most indebted to Dr. Mark Barkey for assuming the responsibility of serving as chair, all my committee members, and especially, Dr. Preston McGill for overseeing this study at the NASA MSFC and for all of his invaluable knowledge and guidance throughout this process. I would like to thank Mr. James Hodo, William “Van” Bradford, Shane Brooke, Carolyn Russell, Tina Malone, EM10, EM20 and EM30 for providing me with invaluable guidance and assistance.

This opportunity to pursue my Ph.D. would not have been possible without the unwavering support of my parents, Owens C. Booker Sr. and Paul and Evelyn Edwards; my children, Eric, Malik and Denise; my very special godson Christian, who on countless occasions made his nana smile and laugh; my Tee Sand, Dean and very special members of Delta Sigma Theta Sorority, Inc. Each have supported me, encouraged me to persist, and provided a shoulder to cry on when needed and have given an extra push when I no longer had the steam to go forward. Each of you, in your own special way, has been an inspiration. To the rest of my family, especially and close friends, thank you for sticking around this long and obstacle filled journey. I truly am blessed to have such a strong support system. It may take a village to raise a child, but it took the universe and its maker to raise this doctor. Thank you.

## TABLE OF CONTENTS

ABSTRACT .....	ii
DEDICATION.....	v
LIST OF ABBREVIATIONS AND SYMBOLS .....	vi
ACKNOWLEDGMENTS .....	viii
LIST OF TABLES .....	xiii
LIST OF FIGURES .....	xv
1. INTRODUCTION AND BACKGROUND .....	1
1.1 Research Rationale and Objectives .....	1
1.2 Aluminum Alloys.....	2
1.2.1 AA 2014-T6.....	2
1.2.2 AA 2219-T87 .....	2
1.3 Friction Stir Welding (FSW) .....	3
1.3.1 Conventional Friction Stir Welding (C-FSW).....	4
1.3.2 C-FSW Weld Profile.....	6
1.3.3 Self Reacting Friction Stir Welding (SR-FSW).....	7
1.3.4 SR-FSW Weld Profile.....	8
1.4 Frictional and Adiabatic Heating .....	10
1.4.1 Frictional Heating .....	10
1.4.2 Adiabatic Heating .....	11
1.5 Dynamic Recovery (DRV) and Dynamic Recrystallization (DRX) .....	11

1.5.1 DRV .....	11
1.5.2 DRX .....	12
1.6 Friction Plug Welding (FPW) .....	12
1.7 Summary .....	14
2. EXPERIMENTATION .....	16
2.1 Test Panel Fabrication .....	16
2.1.1 SR-FSW of 101.6 mm (4 in) Wide Panels of AA 2014/2219 .....	17
2.1.2 SR-FSW of 215.9 mm Wide Panels of AA 2014/2219 .....	18
2.1.3 SR-FSW of 215.9 mm Wide Overlap Panels of AA 2014/2219 .....	19
2.2 Nondestructive Evaluation .....	21
2.2.1 Liquid Penetrant Inspection .....	21
2.2.2 Eddy Current Testing .....	22
2.2.3 Phased Array Ultrasound .....	22
2.3 Post-Weld Heat Treatment .....	22
2.4 Microscopy .....	23
2.5 Vickers Microhardness Testing .....	23
2.6 ARAMIS Three-Dimensional Image Photogrammetry Correlation System, Calibration Methods and Sample Preparation .....	24
2.6.1 ARAMIS 3D Image Photogrammetry System .....	24
2.6.2 ARAMIS Calibration .....	25
2.6.3 ARAMIS Sample Preparation .....	26
2.7 Tensile Testing .....	26

3. RESULTS AND DISCUSSION .....	33
3.1 Initial Weld.....	33
3.1.1 NDE .....	33
3.1.2 Macrographs and Hardness Profiles .....	34
3.1.3 Tensile Test.....	42
3.1.4 Metallography .....	43
3.1.5 Fractography .....	44
3.2 Plug Weld.....	45
3.2.1 NDE .....	45
3.2.2 Hardness Profile.....	46
3.2.3 Tensile Behavior .....	53
3.2.3.1 101.6 mm Samples .....	53
3.2.3.2 215.9 mm Samples .....	56
3.2.3.3 215.9 mm Overlap Samples .....	57
3.2.3.4 Comparative Tensile Data for all Samples.....	58
3.2.4 Strain Data .....	60
3.2.4.1 101.6 mm Samples .....	61
3.2.4.2 215.9 mm Samples .....	65
3.2.4.3 ARAMIS Strain Data .....	65
3.2.5 Fractography .....	69
4. SUMMARY .....	72
5. REFERENCES .....	75
Appendix A (BASE MATERIALS INFORMATION) .....	78

Appendix B (EXPERIMENTAL APPARATUS) .....	79
Appendix C (NON DESTRUCTIVE EVALUATION IMAGES) .....	82
CURRICULUM VITAE.....	89

## LIST OF TABLES

1.	2.1 Capability of the ARAMIS System .....	25
2.	2.2 Summary of test samples by sample identification, tensile test condition for the initial weld and 101.6 mm wide samples .....	31
3.	2.3 Summary of test samples by sample identification, tensile test condition for the 215.9 mm weld and 101.6 mm samples and 215.9 mm overlap samples.....	32
4.	3.1 Phased array ultrasonic Inspection results .....	34
5.	3.2 Initial weld tensile test data.....	43
6.	3.3 Initial weld statistical data .....	43
7.	3.4 Penetrant inspection results.....	46
8.	3.5 101.6 mm samples with M3 plugs test data subset 1 .....	54
9.	3.6 101.6 mm samples with M5 plugs test data subset 2.....	54
10.	3.7 101.6 mm samples with M3 plugs test data subset 3.....	55
11.	3.8 101.6 mm samples with M5 plugs test data subset 4.....	55
12.	3.9 215.9 mm samples with M3 plugs test data subset 1 .....	56
13.	3.10 215.9 mm samples with M3 plugs statistical data subset 1 .....	56
14.	3.11 215.9 mm samples with M5 plugs test data subset 2.....	57
15.	3.12 215.9 mm samples with M5 plugs test data subset 2.....	57
16.	3.13 215.9 mm samples with M5 plugs test data subset 2 without samples with flaw.....	57
17.	3.14 215.9 mm overlap samples with M3 plugs test data subset 1 .....	58

18.	3.15 215.9 mm overlap samples with M3 plugs statistical data subset 1 .....	58
19.	3.16 Comparative statistical data for all samples at room temperature .....	59
20.	3.17 <i>t</i> -test comparative data with respect to PWHT 101.6 mm M3 samples at room temperature .....	59
21.	3.18 <i>t</i> -test comparative data with respect to PWHT 215.9 mm M3 samples at room temperature .....	59
22.	3.19 Comparative statistical data for all samples in LN <sub>2</sub> .....	59
23.	3.20 <i>t</i> -test comparative data with respect to PWHT 101.6 mm M3 samples in LN <sub>2</sub> .....	60
24.	3.21 Weld strength efficiency .....	60
25.	Table A1 Base Material Properties .....	78

## LIST OF FIGURES

1.	1.1 Two metal pieces butted together (Somasekharan, 2005) .....	5
2.	1.2 Progress of tool during FSW process (Somasekharan, 2005).....	5
3.	1.3 Image showing the distinctive zones in a conventional FSW. Parent material is also referred to as base material (Mahoney, et al., 1998).....	6
4.	1.4 Pin tool used in self-reacting FSW (Schneider, et al., 2008).....	8
5.	1.5 Image showing the distinctive zones in a self-reacting friction stir weld (Schneider, et al., 2008) .....	8
6.	1.6 Metal entering severe shear zone surrounding tool (Schneider, et al., 2008).....	9
7.	1.7 Basic material flow model in SR-FSW(Schneider, et al., 2008) .....	10
8.	1.8 Frictional heat is created between the shoulder and the workpiece.....	10
9.	1.9 DRX and DRV in Aluminum (Cahn, 1996) .....	12
10.	1.10 Depiction of tapered plug used or plug welding (Metz, Weishaupt, Barkey, & Fairbee, 2011) .....	14
11.	2.1 Panel schematic for 101.6 mm panels.....	18
12.	2.2 Schematic for 215.9 mm panels.....	19
13.	2.3 Schematic of 215.9 mm wide-overlap panels .....	20
14.	2.4 Isometric rendering of 215.9 mm test panels.....	27
15.	2.5 Photograph of 101.6 mm wide test panels with the bolt hold grips on top and bottom .....	28
16.	3.1 Macrograph of initial weld.....	34
17.	3.2 Defined HAZ and TMAZ of the advancing side to the left of the dispersed interface within the nugget, retreating side TMAZ and HAZ to the right.....	35
18.	3.3 Representation of pin tool and ring vortices of a SR-FSW .....	35
19.	3.4 Schematic showing the travel direction, rotation and location of vortices.....	36



20.	3.5 Ring vortex circulations of the SR-FSW left hand/right hand pin tool. (A) vortex at the top of pin tool, (B) middle of pin tool and (C) bottom of the pin tool.....	37
21.	3.6 Macrographs of SR-FSW dissimilar alloys. AA 2014 is on the advancing side and AA 2219 is on the retreating side. All samples were processed with the same weld parameters. (A) CB-179, (B) CB-180, (C) CB-181, (D) CB-182, (E) CB-183, (F) CB-184, (G) CB-185 and (H) CB-186.....	38
22.	3.7 Macrograph and hardness profile of CB-180 initial weld .....	39
23.	3.8 CB-180 Vickers hardness profile initial weld.....	40
24.	3.9 CB-186 Vickers hardness profile initial weld.....	40
25.	3.10 CB-179-P1 PWHT weld Vickers hardness profile .....	41
26.	3.11 CB-183-P1 PWHT weld Vickers hardness profile .....	41
27.	3.12 Comparison of the PWHT vs. the initial weld hardness profiles.....	42
28.	3.13 Schematic cross-section of initial weld tensile macrograph .....	42
29.	3.14 Leica MZ 16A optical light microscopy with 4.5 magnification of retreating side fracture within the AA 2219-T87 HAZ .....	44
30.	3.15 Extended regions of micro dimples on the fracture surface .....	44
31.	3.16 Fracture surface resultant from tensile test showing a cup cone surface at 1000x. Images taken with a Hitachi S-3700N SEM (Dion D. Jones).....	45
32.	3.17 Schematic of cross-sections of FPW.....	46
33.	3.18 Cross-section macrographs of CB-179-P1 post weld heat treated plug welds of M3 plug major diameter side.....	47
34.	3.19 Cross-section macrographs of CB-183-P1 post weld heat treated plug welds of M5 plug major diameter side.....	48
35.	3.20 Variations in the hardness profile across the three sub sections of CB-179-P1 .....	49
36.	3.21 Hardness profile across the center of CB-179-P1 .....	49
37.	3.22 Hardness profile across the left of center of CB-179-P1 .....	50
38.	3.23 Hardness profile across the right of center of CB-179-P1 .....	50

39.	3.24 Comparative hardness profiles of CB-183-P1 .....	51
40.	3.25 Hardness profile across the center of CB-183-P1 .....	51
41.	3.26 Hardness profile across the left of center of CB-183-P1 .....	52
42.	3.27 Hardness profile across the right of center of CB-183-P1 .....	52
43.	3.28 Placement of strain gages across major diameter of plug of specimen CB-181-P3 ..	61
44.	3.29 Extensometer strain data of 101.6 mm samples.....	62
45.	3.30 (A) Top strain gage and (B) bottom strain gage data of 101.6 mm samples .....	63
46.	3.31 (A) Minor side and (B) major side strain gage data of 101.6 mm samples .....	64
47.	3.32 Extensometer strain data of 215.9 mm samples.....	65
48.	3.33 ARAMIS facet and strain overlay at failure showing extensometer placement.....	66
49.	3.34 Extensometer versus ARAMIS strain data for CB-179-P1 .....	67
50.	3.35 ARAMIS strain gage data for CB-181-P3 on the minor side .....	68
51.	3.36 ARAMIS strain representation before failure.....	68
52.	3.37 Microscopy of bonded surface of weld and FPW.....	69
53.	3.38 Rough ductile surface on the surface of the plug fracture area of the sample that failed through the plug .....	70
54.	3.39 Fracture surface around plug with little or no bond to weld.....	70
55.	3.40 Rough fracture surface (A) ragged fracture with partial plug and (B) ragged fracture through the plug .....	71
56.	3.41 Ductile fracture surface of SR-FSW .....	71
57.	Figure B1 5-axis I-STIR Process Development Systems (PDS) .....	79
58.	Figure B2 ARAMIS cameras used during testing .....	80
59.	Figure B3 200K tensile test frame used during testing.....	81
60.	Figure C1 Phased array ultrasonic inspection output showing flaw in the volume of the weld shown. No flaw in the root or crown was detected .....	83

61.	Figure C2 Phased array ultrasonic inspection output showing flaws in the root of the weld.....	84
62.	Figure C3 Phased array ultrasonic inspection output showing no flaws in crown or volume.....	84
63.	Figure C4 Round indications located lower left quadrant of the plug .....	85
64.	Figure C5 Round indications marked with red marks .....	86
65.	Figure C6 Image showing no indications on the crown side .....	86
66.	Figure C7 Image showing no indications on the root side.....	87
67.	Figure C8 Snap shot of screen displaying Eddy current response in the plug weld HAZ on the crown advancing side. Note slight impedance change .....	88
68.	Figure C9 Snap shot of screen displaying Eddy current response in the plug weld HAZ on the crown retreating side. Note no impedance change .....	88

## **Chapter 1 Introduction and Background**

### **1.1 Research Rationale and Objectives**

This study presents an evaluation of strength, hardness, and strain field of self-reacting friction stir welding (SR-FSW) of dissimilar aluminum alloys both with and without a friction plug weld (FPW). The aluminum alloys (AA) specifically studied are AA 2014-T6 and AA 2219-T87. There are no material data properties in the literature on this combination of SR-FSW of alloys. Much work has been reported on conventional FSW of similar and dissimilar aluminum alloys, but in comparison, very little literature is available describing SR-FSW.

Friction stir welding (FSW) is a joining process wherein metals are joined by the application of heat and pressure which facilitate the flow of the metals. Self-reacting friction stir welding is one variation of friction stir welding, which is a new process being developed at the National Aeronautics and Space Administration (NASA) over the last ten years.

The objective of the study is to understand the fundamental interaction of the materials under static loading conditions of joints of SR-FSW AA 2014/2219 with and without a friction plug weld made with a 2219-T87 plug in a SR-FSW of AA 2014/2219. The weld zones in a SR-FSW of AA 2014/2219 alloys exhibit a distorted weld seam trace within the nugget region whose microhardness is comparable to that of the parent material. The formation of this zone and the role that this zone plays in the mechanical behavior of the welds are examined in this study. The interaction between the FPW and the SR-FSW results in a greater strain area around the plug under static tensile test conditions in smaller samples than in wider samples. At

the same stress level, the strain behavior, strength, and interaction of the parent material, weld zone and plug are very important discriminators used during the development process to accept or reject materials for design. The FPW/SR-FSW interface is a critical region to understand.

## **1.2 Aluminum Alloys**

Aerospace industry designers and engineers strive to use the lightest weight material that will meet the operational requirements. These requirements include strength, stiffness, damage tolerance, environmental compatibility, manufacturability and cost. The aluminum alloys used in this study, 2014 and 2219, are aluminum-copper alloys and are widely used in the aerospace industry due to their high strength, low density and high ductility as compared to AA 2013 or AA 2024.

**1.2.1 AA 2014-T6.** AA 2014-T6 is an aluminum alloy with an alloying element nominal composition of 4% copper, 0.8% magnesium, and 0.8% silicon. The T6 temper designation indicates the material is solution heat treated and artificially aged. An increase in strength is observed at cryogenic temperatures. Specifically, there is an increase in ultimate tensile strength of 455 to 579 MPa and a 10% increase in yield strength from 455 to 496 MPa when cooled from room temperature to the boiling point of nitrogen (-196°C) (MATWEB, 2011a). The mechanical, thermal, thermomechanical material properties and the chemical compositional limits (%) are shown in Table A1.

**1.2.2 AA 2219-T87.** AA 2219-T87 is an aluminum alloy with an alloying element nominal composition 6% copper, 0.3% manganese and 0.2% zirconium. The T87 designation indicates the material is solution-heat treated, cold worked by stretching and then artificially aged. AA 2219-T87 exhibits an ultimate tensile strength of 440 MPa and a yield strength of 360 MPa (MATWEB, 2011b). AA 2219-T87 displays increasing fracture toughness from room

temperatures down to  $-196^{\circ}\text{C}$  (Aluminum Alloy Properties, 2009). The mechanical, thermal, thermomechanical material properties and the chemical compositional limits (%) are shown in Table A1.

### **1.3 Friction Stir Welding (FSW)**

FSW is a solid-state joining process. During a friction stir weld, the metal is not melted during the process; the mechanical stirring process heats the material to the point where it flows plastically. FSW was invented and patented by The Welding Institute (Thomas, et al., 1991), a British research and technology organization; the process is applicable to aerospace, shipbuilding, aircraft and automotive industries. Two key benefits of this new technology are that it allows aluminum alloys to be welded together that cannot be readily fusion arc welded and it creates stronger welds than those obtained from fusion arc welds (Raj, Sharm, & Singh, 2010). FSW utilizes frictional heating combined with forging pressure to produce high-strength bonds virtually free of defects (*Space Shuttle Technology Summary: Friction Stir Welding*, 2001).

There are several advantages to FSW that were recently reported (Threadgill, Leonard, Shercliff, & Withers, 2009):

- i. As a solid state process, it can be applied to all the major aluminum alloys and avoids problems of hot cracking, porosity, and compositional loss common to aluminum fusion welding processes.
- ii. As a mechanized process, FSW does not rely on specialized welding skills.
- iii. No shielding gas or filler wire is required for aluminum alloys.
- iv. The process is tolerant to poor quality edge preparation: gaps of up to 20% of plate thickness can be tolerated, although this leads inevitably to a reduction in local section thickness since no filler is added.
- v. The absence of fusion removes much of the thermal contraction associated with solidification and cooling, leading to significant reductions in distortion; however, it is not a zero distortion technique.
- vi. It is very flexible, being applied to joining in one, two and three dimensions, being applicable to butt, lap and spot weld geometries; welding can be conducted in any position.
- vii. FSW provides excellent mechanical properties, competing strongly with welds made by other processes.

- viii. The energy required at the weld for FSW lies between laser welding (which requires less energy) and metal inert gas (MIG) welding (which typically needs more energy).

There are two primary forms of friction stir welds: 1) conventional friction stir welds which have been detailed in the literature and 2) self-reacting friction stir welds.

**1.3.1 Conventional Friction Stir Welding (C-FSW).** In C-FSW, a pin tool is rotated between 180 to 300 revolutions per minute, depending on the thickness of the material. The force is reacted by an anvil which runs the entire length of the weld. The pin tip of the pin-tool is forced into the material under 34 to 69 MPa of pressure. The pin continues rotating and moves forward at a rate of 88.9 to 127 mm per minute. As the pin rotates, friction heats the surrounding material and rapidly produces a softened "plasticized" area around the pin. As the pin travels forward, the material behind the pin is forged under pressure from the tool and consolidates to form a bond. Unlike fusion welding, no melting occurs in this process. The advancing side of the weld is the side of the weld in which the rotational motion of the lateral surface of the welding tool is in the same direction as the travel direction. The opposite side of the weld is called the retreating side of the weld, where the rotational motion of the lateral surface opposes the travel direction. Figure 1.1 shows two discrete metal work pieces butted together, along with the tool (with a pin). Figure 1.2 shows the progress of the tool through the joint, also showing the weld zone and the region affected by the tool shoulder. During the process, frictional heat is generated between the wear-resistant welding tool shoulder and pin, and the material of the work pieces.

This heat, along with the heat generated by the mechanical mixing process and the adiabatic heat within the material, causes the stirred materials to soften without reaching the

melting point, allowing the traversing of the tool along the weld line in a plasticized cylindrical shaft of metal.

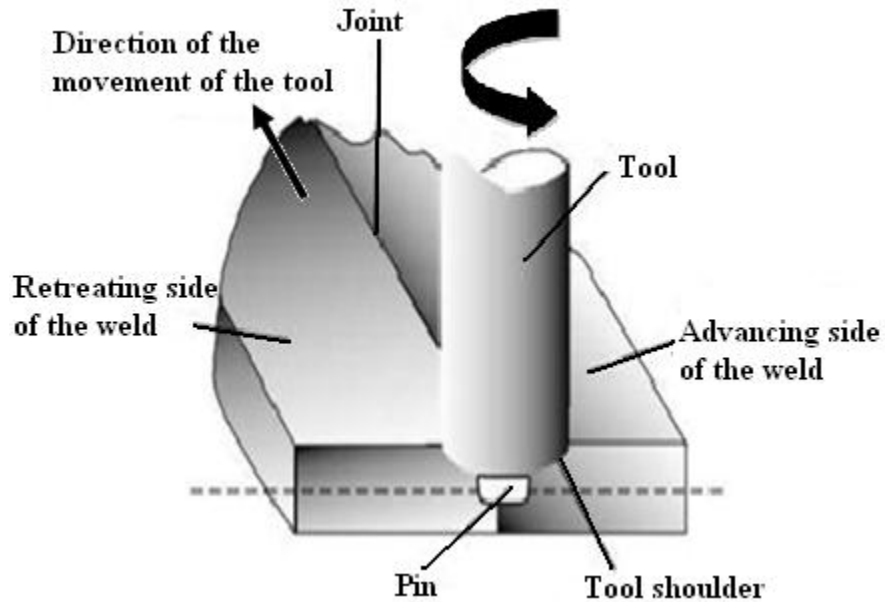


Figure 1.1 Two metal pieces butted together (Somasekharan, 2005).

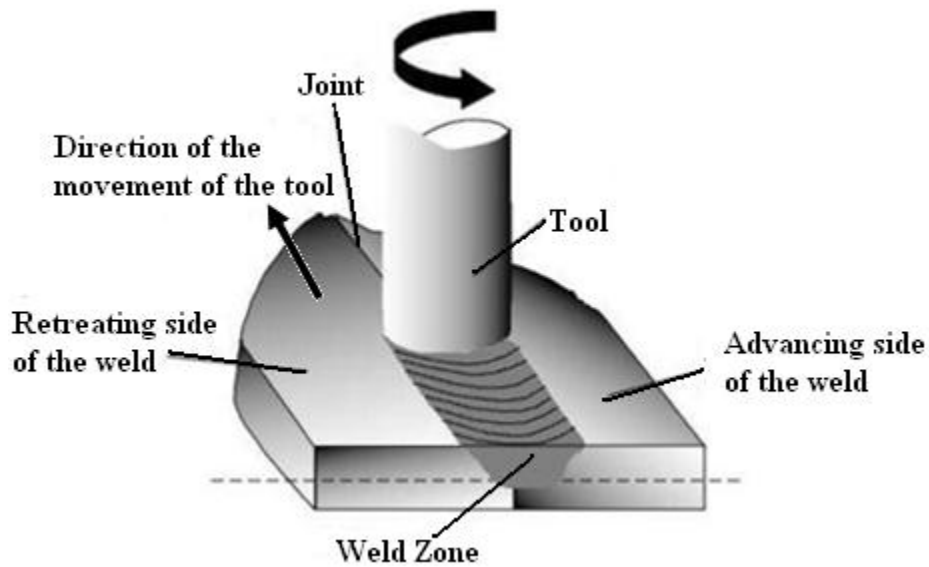


Figure 1.2 Progress of tool during FSW process (Somasekharan, 2005).

As the tool is moved in the direction of welding, the leading face of the pin forces plasticized material to the back of the pin while applying a substantial forging force to consolidate the weld metal.



**1.3.2 C-FSW Weld Profile.** The conventional friction stir weld has distinct regions known as the flow arm, nugget, thermo-mechanically affected zone (TMAZ), and heat-affected zone (HAZ) (Mahoney, Rhodes, Flintoff, Spurling, & Bingel, 1998) which can be seen in Figure 1.3.

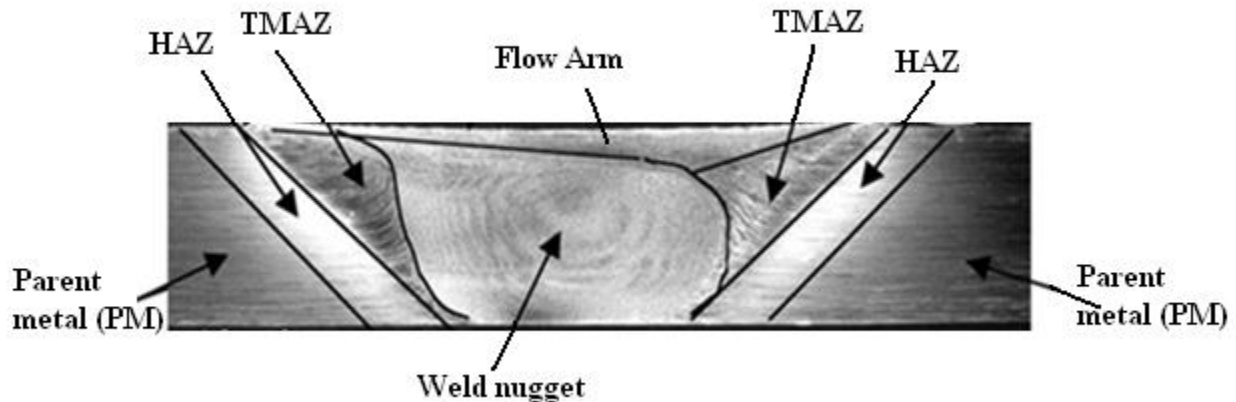


Figure 1.3 Image showing the distinctive zones in a conventional FSW. Parent material is also referred to as base material (Mahoney, et al., 1998).

Each zone experiences a variety of heat variations (and deformation in the nugget and TMAZ) which results in a complex mixture of microstructural processes such as dynamic recrystallization (DRX) and dynamic recovery (DRV). The flow arm is on the upper surface of the weld and consists of material that is dragged by the shoulder from the retreating side of the weld, around the rear of the tool, and deposited on the advancing side (Mishra & Mahoney, 2007). The HAZ is characterized by a coarsening of the precipitate particle distribution caused by the heat generated during the process (Genevois, Deschamps, Denquin, & Doisneau-Cottignies, 2005). In the region which is closest to the weld-center, the material experiences an extreme heat variance that has modified the microstructure and/or the mechanical properties. Post-weld cooling of friction stir aluminum alloy welds leads to complex microstructural evolution in the nugget region due to supersaturated alloying elements, the interaction of precipitation and the

recovery of deformed grains (Oertelt, Babu, David, & Kenik, 2001). This in turn leads to a difference in mechanical properties across the weld and such variation may be detrimental to the joint performance. The nugget and TMAZ are typically characterized by coarse heterogeneous precipitation that occurs during weld cooling and post-weld natural aging (Sullivan & Robson, 2008). The grain structure in the nugget is generally dynamically recrystallized (Hassan, Norman, Price, & Prangnell, 2003) whereas the TMAZ generally contains deformed parent grains. In the case of aluminum, it is possible to obtain significant plastic strain without recrystallization in the TMAZ region, and there is generally a distinct boundary between the recrystallized zone (weld nugget) and the deformed zones of the TMAZ.

**1.3.3 Self Reacting Friction Stir Welding (SR-FSW).** In SR-FSW there are two rotating shoulders: one on the top (or crown) and one on the bottom (or root) of the workpiece. In this case, a threaded shaft protrudes from the tip of the pin tool to beyond the back surface of the workpiece. The back shoulder is held axially in place by tension created by a nut on the threaded shaft. The main axial force exerted on the workpiece by the tool and front shoulder is reacted through the back shoulder and the threaded shaft, back into the FSW machine head, so that a backing anvil is no longer needed (Nabors, 2006). The opposing forces balance, simplifying the backup tooling used along the inside length of the weld. Sato et al. (2004) reports on a self-reacting tool and indicates that the concept was introduced in the original TWI patent and that it was demonstrated by Boeing (Khaled, 2005). A schematic of the tool developed at the Marshall Space Flight Center (Carter, 2004) is shown in Figure 1.4.

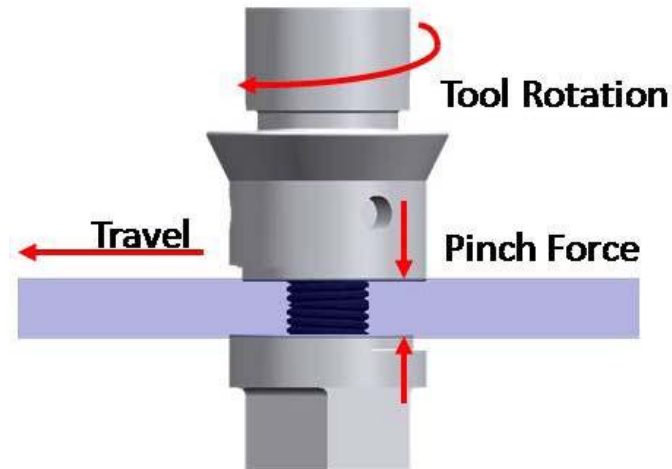


Figure 1.4 Pin tool used in self-reacting FSW (Schneider, et al., 2008).

**1.3.4 SR-FSW Weld Profile.** As shown in Figure 1.5, there are three distinctive weld zones in the cross-section of a SR-FSW of AA2195-T87 plates. The zones are the HAZ, TMAZ and the nugget region, which are different in geometric shape from those seen in the C-FSW. Note the TMAZ forms a bulge into the nugget region.

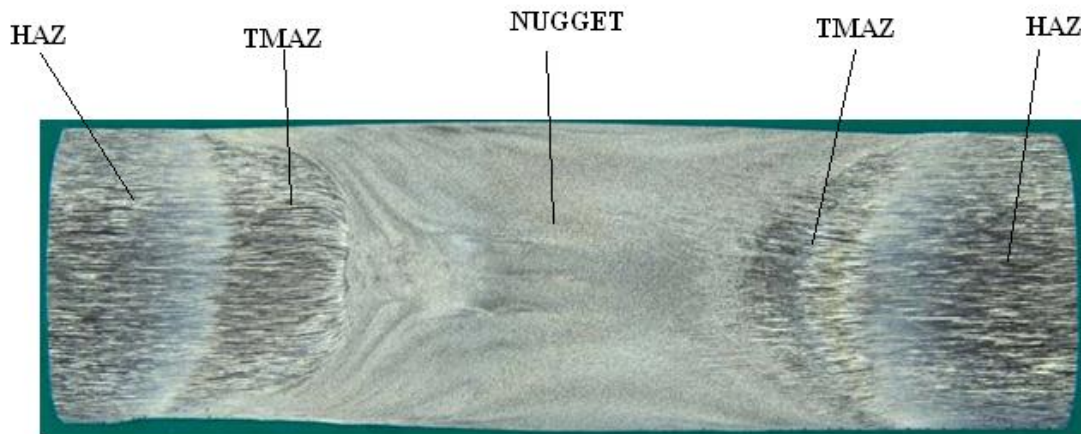


Figure 1.5 Image showing the distinctive zones in a self-reacting friction stir weld (Schneider, et al., 2008).

Schneider et al. (2008) explains the appearance of the SR-FSW weld zone with a kinematic material flow concept. This approach describes a rotating plug of metal attached to the weld tool and translated along the weld seam with the tool. The rotating plug of metal is bounded by the tool surface and a shearing surface, observed to be very thin, separating the

rotating plug from the fixed body of weld metal outside the plug. Figure 1.6 illustrates the metal flow crossing this boundary which is exposed to a very high shear strain rate. At the reported temperature range of 0.8-0.9 times the solidus melting temperature ( $T_{mp}$ ) of the alloy, the flow stress of the metal is almost uniform in the close vicinity of the tool and shear surface (Brick, Gordan, & Phillips, 1965). Because the metal flow stress depends mostly on temperature, only minor variations in the flow stress are also expected close to the tool.

The weld tool has a threaded pin which creates a ring vortex velocity field with pronounced axial as well as radial flow velocity.

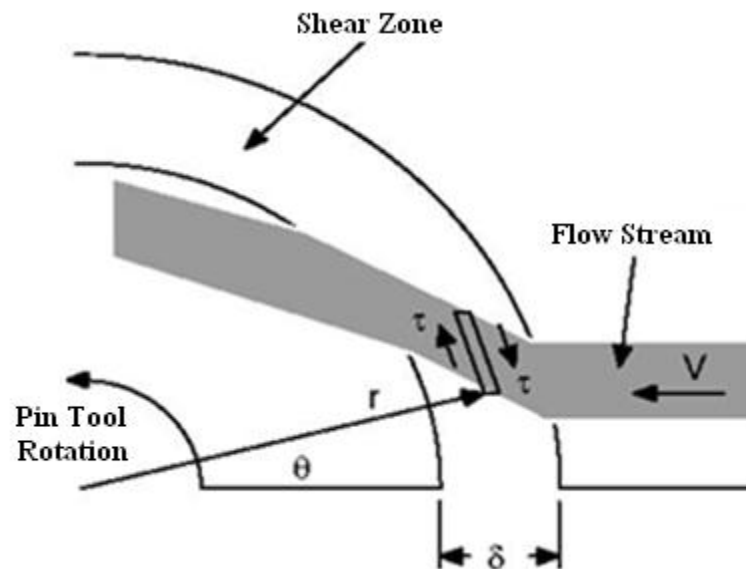


Figure 1.6 Metal entering severe shear zone surrounding tool (Schneider, et al., 2008).

This axial field component is responsible for retaining metal within the rotating plug during multiple revolutions as reported in other studies. Schneider et al. (2008) show a relationship between weld nugget bulges and weld parameters using a basic flow model shown in Figure 1.7 for SR-FSW.

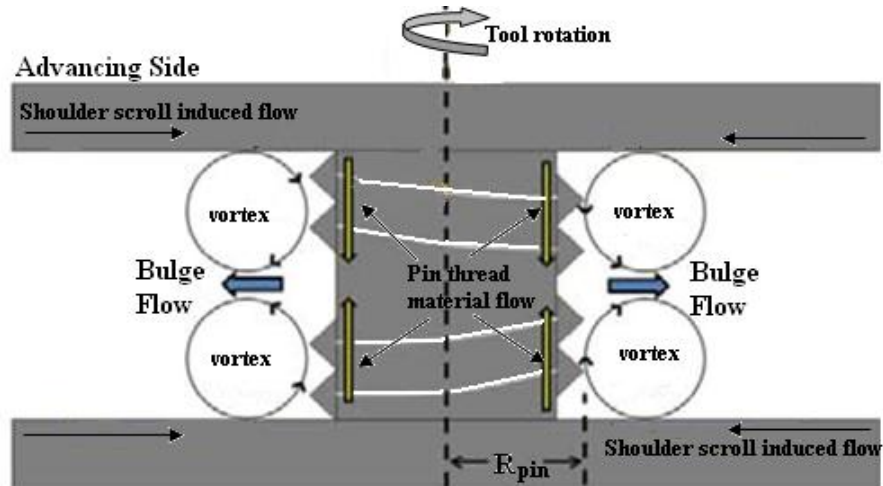


Figure 1.7 Basic material flow model in SR-FSW (Schneider, et al., 2008).

## 1.4 Frictional and Adiabatic Heating

The severe plastic deformation in C-FSW and SR-FSW is facilitated by the dynamic recrystallization (DRX) process which is created by the energy input into the welding process by frictional heating from the tool against the workpiece and by adiabatic heating. Both are produced as a result of the mechanical shearing and mixing of the base materials by the rotating FSW tool while traveling the length of the weld joint.

**1.4.1 Frictional Heating.** Frictional heat is created by the sliding of the rotating tool shoulders and the rotating tool probe against the workpiece surfaces as seen in Figure 1.8.

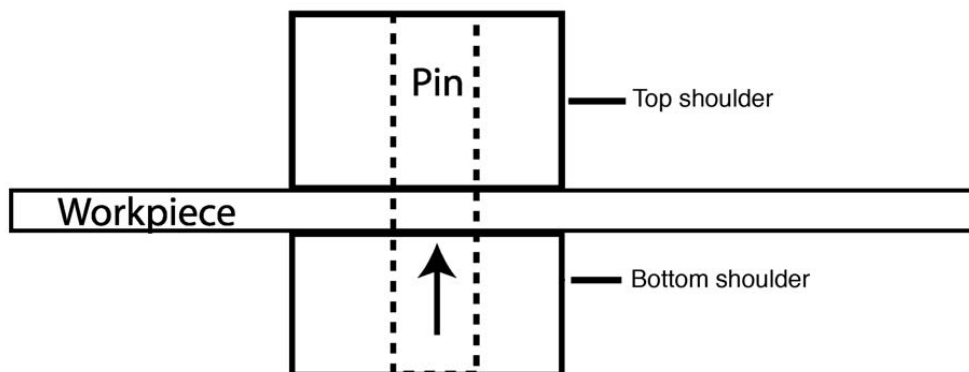


Figure 1.8 Frictional heat is created between the shoulder and the workpiece.

The surface temperature from frictional heating depends on the thermal conductivity of the metals in contact, the exposed surface that allows dissipation of heat to air and the number of point contacts between the materials.

**1.4.2 Adiabatic Heating.** Adiabatic heating is created by the release of energy stored within the grains of the rolled base material, and because of the extremely short amount of time for deformation, no heat is exchanged, but part of the stored energy is dissipated from the welded region during the recovery and the DRX of the grains. The effect of adiabatic heating and adiabatic shear bands on plastic deformation has been researched by Murr et al. (2002), Perez-Pado et al. (2001) and Pantleon et al. (1996). Also, Perez-Pado et al. (2001) and Pantleon et al. (1996) developed an expression for adiabatic heating as a result of plastic deformation in FSW. A part of the mechanical energy expended in the plastic deformation gets stored in the material and the rest is dissipated as heat.

## **1.5 Dynamic Recovery (DRV) and Dynamic Recrystallization (DRX)**

The weld nugget is a clearly defined zone in most welds. The TMAZ is affected by severe plastic deformation that occurs during welding. The elevated temperatures in the weld zone facilitate the dynamic recrystallization that follows dynamic recovery from stored energy in the TMAZ. Dynamic recovery has a strong effect on the shape of the stress-strain curves (Reed-Hill & Abbaschian, 1994).

**1.5.1 DRV.** Recovery in plastically deformed metals involves recovery of stored energy, mechanical properties, and microstructure. When recovery occurs during hot-working, it is called Dynamic Recovery (DRV). DRV precedes dynamic recrystallization (DRX) in high strain rate processes, with DRV being quite pronounced in metals of high stacking fault energy

(rapid dislocation climb) such as aluminum. During hot-working, continuous subgrain growth leads to annihilation and creation of sub-grain boundaries (Cahn, 1996).

**1.5.2 DRX.** DRX is the recrystallization occurring during deformation; this process occurs in a few milliseconds. Sufficiently high strains and strain rates tend to cause DRX (Cahn, 1996). DRX facilitates plastic deformation which allows the mechanical mixing of the base or parent material by the FSW tool. As seen in Figure 1.9, when the tool stirs the material in the weld joint, there is a mixing of the neighboring base material into the weld zone.

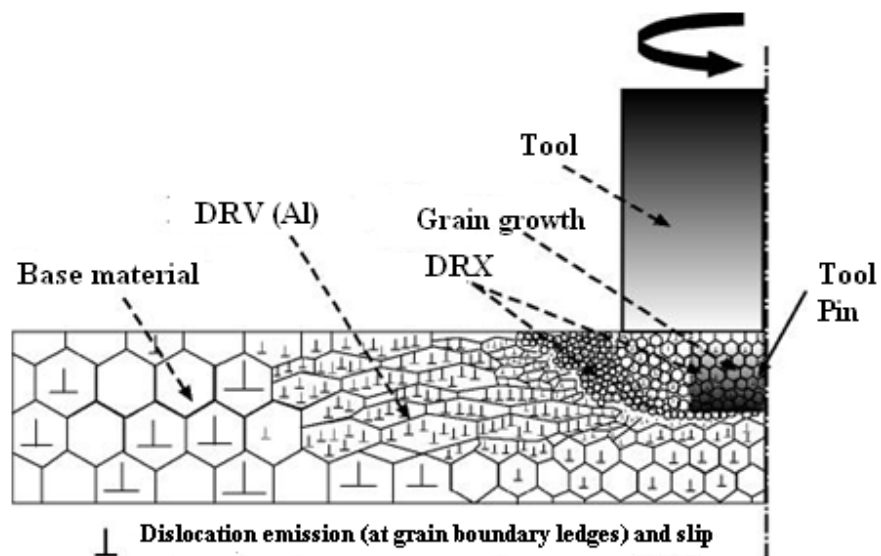


Figure 1.9 DRX and DRV in Aluminum (Cahn, 1996).

The material closest to the base material undergoes dynamic recovery, and inside the weld zone, the grains undergo dynamic recrystallization. The grains that experience DRV are elongated in nature while the grains that undergo DRX are fine in nature (Murr, Trillo, Pappu, & Kennedy, 2002).

## 1.6 Friction Plug Welding (FPW)

When longitudinal FSW are made, the tool travels off the workpiece on excess material at the beginning and end of the panel. The excess material is later trimmed off and removes any

start up or termination hole left by the friction stir weld tool. However, when circumferential frictional stir welds are made, a hole is left in the weld when the tool is removed. A process called friction plug weld (FPW) is used to repair the hole. FPW is a derivative of Friction Taper Plug Welding which was originally developed as a solid state repair method for steels (*Space Shuttle Technology Summary: Friction Stir Welding*, 2001).

The friction plug weld tool is a computer controlled, hydraulically driven system used to close-out the exit hole left at the end of a SR-FSW. The tool can also be used to repair weld defects in FSW or defects in parent material. The system consists of a hydraulically-driven spindle coupled to a linear hydraulic ram. During operation, the spindle rotates the ram assembly which in turn rotates the plug. The rotating ram pulls the plug into the weld joint with a predetermined axial load. This causes significant plastic flow and redistribution of material surrounding the plug. When the ram reaches a predetermined position, spindle rotation is halted and the forging load is terminated thus completing the friction plug weld. The complete conical section of the tapered plug is welded to the matching surface of the hole almost simultaneously. Considerable heat is generated, but the plug and workpiece are welded together, in a solid state process in which no melting occurs. Excess plug protruding from the repaired hole is removed. The plug welding system is capable of operating with speeds in excess of 7000 rpm, and ram forces greater than 62 kN.

In FPW, the primary weld parameters are plug rotation speed, forging load and plug displacement (the total distance the plug travels during the process). Also of primary importance are the plug geometry and hole geometry (Hartley, 2008). FPW has received little attention in the literature and each laboratory has had to develop its own data base of plug weld parameters versus plug weld strength (McClure, 2005). A sketch of the tapered plug is shown in



Figure 1.10. The plug is comprised of three main parts. The top of the plug consists of a heat sink and annular shoulder, and the middle of the plug section consists of the main portion of the plug that fills the hole in the plate. This section has a major diameter at the heat sink end, and transitions to a minor diameter through a double taper. The lower portion consists of the shank, threaded end, and conical tip. The threaded section is used as a means to attach the plug to the friction plug welding machine.

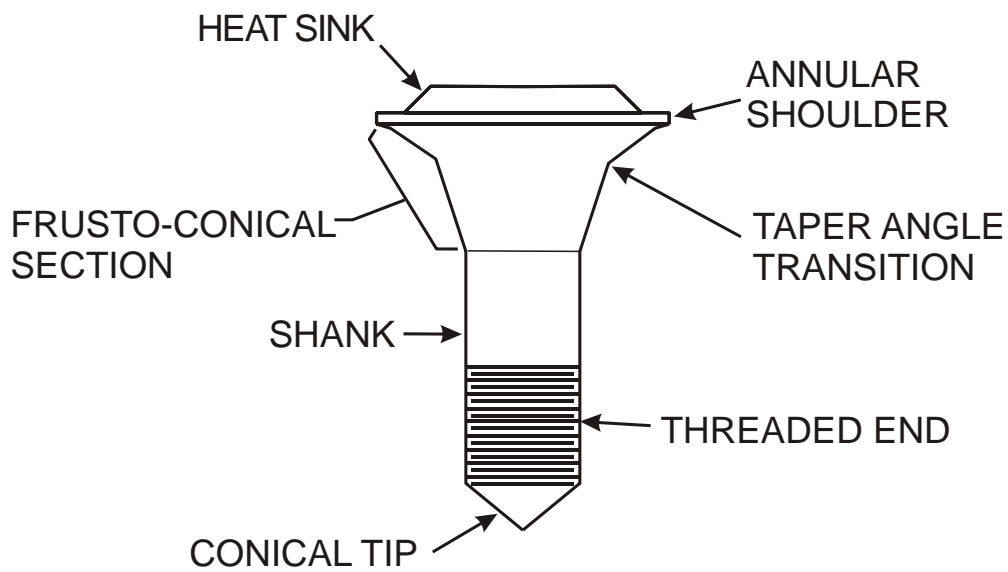


Figure 1.10 Depiction of tapered plug used or plug welding (Metz, Weishaupt, Barkey, & Fairbee, 2011).

### 1.7 Summary

Even though extensive work has been reviewed in literature on similar and dissimilar aluminum alloys for C-FSW covering microstructure, microhardness profiles and material strength testing, no literature has been reported for SR-FSW. This study will focus on testing and evaluation methods of SR-FSW of AA2014/AA2219 with and without an AA2195-T 87 FPW. Nondestructive evaluation is used to examine the material to detect surface and internal flaws that could affect strength and failure modes. Evaluation of the microstructure and microhardness was used to make a qualitative assessment of the variation of strength across the

welds, and tensile tests were used to determine the ultimate tensile strength, yield strength and modulus of elasticity which are basic material properties that are critical for component design and service performance assessment. The sample set consisted of 101.6 mm and 215.9 mm samples to study how the plug is affected by the width of the sample. Additionally, a subset was set; some were post weld heat treated (PWHT) to simulate the heating that occurs during an adhesive cure cycle applied to the flight structure. Within the 215.9 mm panels, a subset of panels referred to as overlap panels was studied to characterize properties of a closeout weld. The 101.6 mm samples were tested at room temperature and liquid (LN<sub>2</sub>) (-196°C) temperature to simulate flight conditions.

## **Chapter 2 Experimentation**

This chapter details the fabrication of the SR-FSW AA2014-T6 and AA2219-T87 with the addition of an AA2219 FPW. The first section details the initial weld formed between an AA2014-T6 plate on the advancing side and an AA2219-T87 plate on the retreating side. The second section details a SR-FSW of AA2014-T6 and AA2219-T87 with the addition of an AA2219 FPW. Specimens of different widths, 101.6 mm and the 215.9 mm, were manufactured with identical weld conditions with a decrease in spindle speed for the 215.9 mm overlap panels. The 101.6 mm samples were tested at room temperature and LN<sub>2</sub> (-196°C).

### **2.1 Test Panel Fabrication**

Test samples used in this investigation were taken from welded test panels. All test panels were 5.28 mm thick and butt welded using a 5-axis I-STIR Process Development System (PDS) shown in Figure B1 Friction Stir Welder located at the NASA Marshall Space Flight Center. The test panels were fabricated with AA 2014 on the advancing side and AA 2219 on the retreating side. The PDS is a commercially available system manufactured by MTS Systems Corporation in Eden Prairie, Minnesota. The system has the capability to perform both self-reacting and conventional friction stir welding. It has a travel range of 1000 mm in the x-direction, 2000 mm in the y-direction and 680 mm in the z-direction. It has a pitch of  $\pm 15^\circ$  and a roll of  $\pm 15^\circ$ .

The friction plug welding tool used in this work was designed and developed at the NASA Marshall Space Flight Center. The plugs are manufactured from AA 2219-T87 and are tapered. Since the plugs are pulled through a uniform hole in the weld, the tapered plug

geometry results in a root (bottom) side diameter which is larger than the crown (top) side diameter. Two plug geometries designated M3 and M5 were used in this investigation. The M3 plugs are small diameter plugs used for close-out of a circumferential SR-FSW. The M5 plugs are large diameter plugs used as a contingency for repair for the M3 plug.

**2.1.1 SR-FSW of 101.6 mm (4 in) Wide Panels of AA 2014/2219.** Panels were welded to create three samples at a time. Abutting weld edges were prepped immediately prior to welding by wirebrushing the edge of the panel and 38 mm of top and bottom surface of the panel. The panels were then cleaned with acetone and isopropyl alcohol. The abutting edges were then draw filed to provide a clean surface free of oxides. This is a critical step since residual surface oxides can result in a poor bond. The start hole, shown in Figure 2.1, is drilled with the centerline offset towards the retreating side. The panel is then welded with a left hand/right hand threaded pin in a single pass. The weld is the full length of the panel and is a full penetration weld. After the panel has been welded, the root and crown sides of the panel were sanded to remove slivers and burrs. All panels were handled with clean gloves.

Welded panels receive liquid penetrant, phased array ultrasonic and eddy current non-destructive evaluations. Following inspection, a hole, sized to accommodate the plug, is drilled in each section as shown in Figure 2.1.

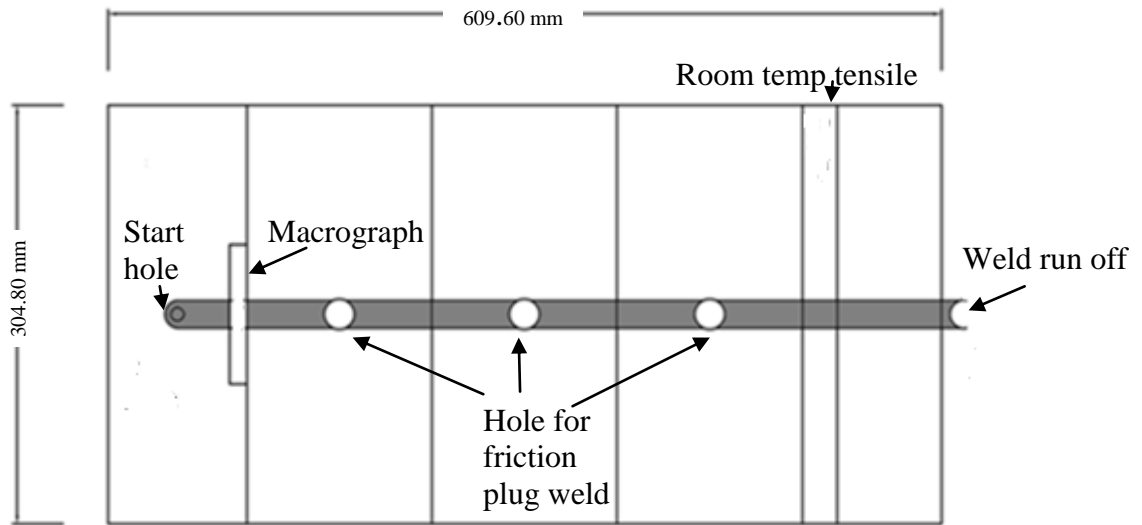


Figure 2.1 Panel schematic for 101.6 mm panels.

Each initial weld root side surface is sanded before drilling. After drilling, a plug is cleaned with a wire brush followed with an isopropyl alcohol wipe immediately prior to welding. The plug is placed through the hole and threaded into the plug weld tool.

**2.1.2 SR-FSW of 215.9 mm Wide Panels of AA 2014/2219.** Panels were welded such that two samples can be machined from a panel. As with the 101.6 mm samples, abutting weld edges were prepped immediately prior to welding by wirebrushing the edge of the panel and 38 mm of the top and bottom surface of the panel. The panels were then cleaned with acetone and isopropyl alcohol. The abutting edges were then draw filed to provide a clean surface free of oxides. The start hole, shown in Figure 2.2, is drilled with the centerline offset towards the retreating side. The panel is then welded with a left hand/right hand threaded pin in a single pass. The weld is the full length of the panel and is a full penetration weld. After the panel has been welded, the root and crown sides of the panel were sanded to remove slivers and burrs. All panels were handled with clean gloves.

Following NDE inspection, a hole, sized to accommodate the plug, is drilled in each section one at a time. Each initial weld root side surface is sanded before drilling. The plug is cleaned with a wire brush followed with an isopropyl alcohol wipe immediately prior to welding. The plug is placed through the crown side hole and threaded into the plug weld tool.

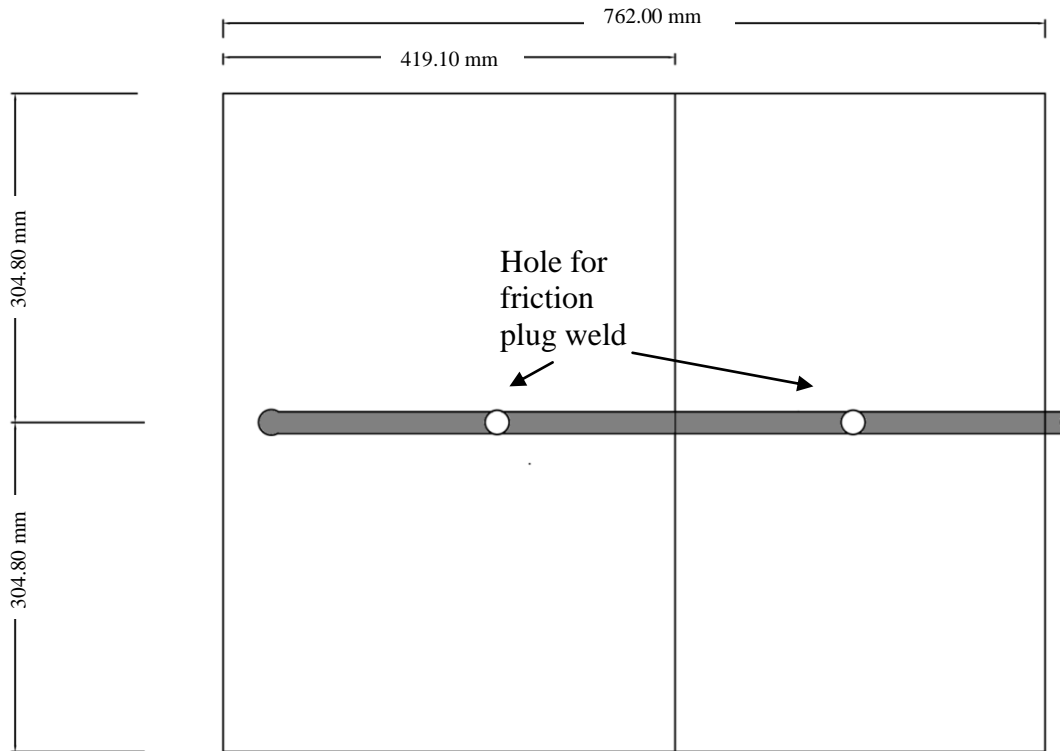


Figure 2.2 Schematic for 215.9 mm panels.

**2.1.3 SR-FSW of 215.9 mm Wide Overlap Panels of AA 2014/2219.** Overlap panels simulate manufacturing process for circumferential welds in which the SR-FSW overlaps itself or is re-welded. Panels were welded such that two test samples can be machined from a panel. Each panel was prepped before welding by removing by wirebrushing 38.1 mm of the top and bottom surface of the panel followed by cleaning with acetone followed by isopropyl alcohol. The edges were then draw filed along abutting edges. A 76.2 mm x 76.2 mm AA 2219 start tab is welded to the left side of the panels. The extra material added as a start tab is used to start the weld so that there is a continuous weld on the test samples. The start tab is placed far enough

away from the sample such that FSW heat affected zone does not interfere with the side of the sample.

The panel is re-welded with a left hand/right hand threaded pin with the initial weld starting at point A and running off the end of the panel as seen in Figure 2.3. The second re-weld is started at point B and continues down the length of the panel passing over point A, creating a re-weld and ending 190.5 mm to the right of point A leaving a exit hole. The third re-weld is started point C, 38.1 mm from the left end of the start tab, passing over point B creating another re-weld and ending 190.5 mm to the left of point A leaving another exit hole. The flash is sanded on both sides of the panel to remove slivers or burrs after welding. All panels were handled with clean gloves. After non-destructive evaluations were conducted, the panels were cut in half in order to make two test samples. The initial weld root side is sanded, and another hole is cut with the termination hole at the center. One small diameter AA 2219 plug is cleaned with a wire brush immediately followed with alcohol wipe prior to welding.

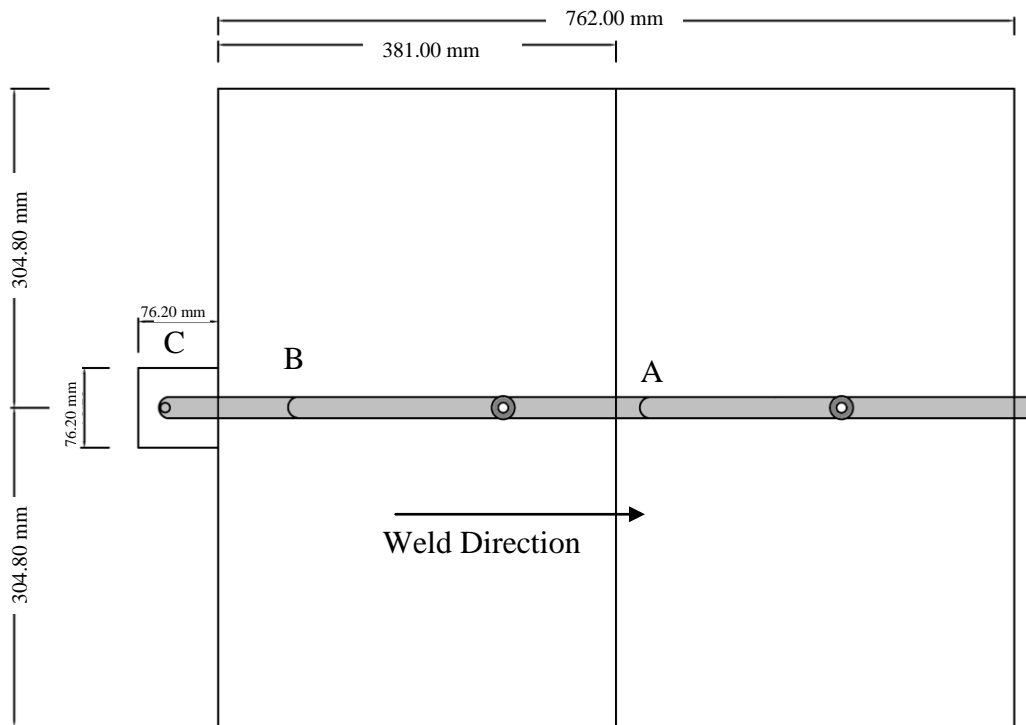


Figure 2.3 Schematic of 215.9 mm wide-overlap panels.

## **2.2 Nondestructive Evaluation**

Welded panels were subjected to nondestructive evaluation (NDE), which is an integral operation in the production of welded joints for space flight hardware. The objective of NDE is to benignly examine the material in a way that will detect defects in the weld that compromise the structural and/or operational integrity of the weld. In the broadest sense, NDE can be divided into two primary categories: surface inspections and volumetric inspections. In the fabrication of friction stir welds and friction stir plugs, two surface inspection techniques and one volumetric inspection technique were implemented. The two surface techniques were liquid penetrant and eddy current; the volumetric technique was phased array ultrasound.

**2.2.1 Liquid Penetrant Inspection.** Liquid penetrant inspection is a nondestructive evaluation method used to examine the surface of a material or weld joint. The penetrant is allowed to sit on the surface of the part and is then removed by wiping with a clean cloth. The liquid penetrant wicks down into any cracks or crack-like defects in the weld. After wiping, the penetrant will then “bleed” out of the cracks and become visible under ultraviolet light.

In this study, the plug welds in the test panels were inspected with liquid penetrant per ASTM E1417 2005–Standard Practice for Liquid Penetrant Testing, ASTM E165–Standard Test Method for Liquid Penetrant Examination and ASTM E1209-05–Standard Test Method for Fluorescent Liquid Penetrant Examination using the Water Washable Process. An overview of the process is provided below.

1. Samples were cleaned with isopropyl alcohol to remove any debris.
2. Penetrant was applied and allowed to sit for 30 minutes.
3. Excess penetrant was washed off.
4. Panels were cleaned again with alcohol.



5. Samples were examined under an ultraviolet light with a wavelength of 368 nm.

**2.2.2 Eddy Current Testing.** Eddy current inspection is a nondestructive evaluation method used to examine the surface of a material. Fundamentally, the process involves inducing a magnetic field into a conductive material (part being inspected) and monitoring the resulting electromotive force (EMF) in the part. The magnetic field induces currents in the conductor (part being inspected) that travel in closed loops called eddy currents. A defect or flaw in the part modifies the eddy current resulting in a detectable change in the EMF (Shull, 2002). In this study, the plug welds in the test panels were inspected across the weld, plug and parent metal interfaces on the crown and root side of each plug. The test was conducted using an ELOTEST eddy current tester with a 500 kHz frequency with a 3.175 mm mini rotor probe.

**2.2.3 Phased Array Ultrasound.** Phased array ultrasound inspection is a nondestructive evaluation method used to examine the internal volume of a material. Fundamentally, the process involves subjecting the specimen to a high frequency sound wave. The sound wave travels through the test specimen and is received by a transducer. Differences between the transmitted wave and the returned wave can be analyzed to determine the size and location of flaws or defects internal to the material (Shull, 2002). Phased array ultrasound was used to inspect the initial weld and the plug weld for defects. The test was conducted using an OmniScan MX system with a transducer frequency of 10.0 MHz.

### **2.3 Post-Weld Heat Treatment**

Ten of the 101.6 mm wide panels and all of the 215.9 mm wide panels were thermally cycled. The samples were first heated to 126.7°C for 30 minutes and then to 165.6°C for 90 minutes. In this study, the thermal cycle simulates the heating that occurs during an adhesive cure cycle applied to the flight structure.

## **2.4 Microscopy**

Microscopy was performed to characterize the fracture surface of the samples. Optical microscopy images of the samples were acquired with a Leica MZ16 FA microscope with no etchants used on the samples. Scanning electron microscopy (SEM) was completed with a Hitachi S-3700N SEM.

## **2.5 Vickers Microhardness Testing**

Vickers Hardness Testing or microindentation hardness testing was a method for measuring the hardness of a material on a microscopic scale. It is used to measure the material's ability to resist plastic deformation and for making a qualitative assessment of the variation of strength across the weld. Strength has been shown to be proportional to hardness (Srinivasan, Arora, Dietzel, Pandey, & Schaper, 2010).

For the hardness test conducted in this study, a precision diamond indenter is impressed into the material. The impression length, measured microscopically, and the test load were used to calculate a hardness value. The hardness values obtained were useful indicators of a material's properties and expected service behavior. These indentations were made using an automatic Vickers hardness tester with a 700 gram test load. The tester applies the selected test load using dead weights. The length of the hardness impressions were measured with a light microscope using video imaging and computer software. A hardness number was calculated using the test load, the impression length, and a shape factor for the indenter type used for the test. (*Handbook for Analytical Methods for Materials*, 2010). Microhardness profiles were taken on 16 initial welds and 6 plug weld cross-sections that were ground, polished and mounted to develop relative strength profiles across the welds.

## **2.6 ARAMIS Three-Dimensional Image Photogrammetry Correlation System, Calibration Methods and Sample Preparation**

Each specimen tested at room temperature was prepared with a speckle pattern to obtain the deformation response of the sample as a function of applied load. This data was used to determine the strain distribution pattern in the weld. The analysis of displacement fields from mechanical tests is often used to correlate between experiments and simulations (Besnard, Hild, & Roux, 2006).

**2.6.1 ARAMIS 3D Image Photogrammetry System.** Three-dimensional image correlation photogrammetry is a full-field displacement and strain measurement tool typically used for static and slow strain rate testing. The tool has been used in conjunction with pulsed illumination for high speed rotating component evaluation (Schmidt, et al., 2005). Sample preparation consists of applying a regular or random high contrast speckle pattern to the surface, commonly with spray paint. Thousands of overlapping unique correlation areas known as facets (typically 15 pixels square) are defined across the entire imaging area. The center of each facet is a measurement point that can be thought of as a 3D extensometer. Closely spaced arrays of them form in-plane strain rosettes. The facet centers are tracked, in each successive pair of images, with accuracy up to one hundredth of a pixel. Then, using the principles of photogrammetry, the 3D coordinates of each facet are determined for each picture set. The results are the 3D shape of the component; the 3D displacements are then used to calculate surface strains (Schmidt, et al., 2005). Data can be presented as color plots, movies, section line diagrams, etc., and ASCII exports support further analysis and comparison. Because of similar output, this is an excellent tool for verifying and iterating finite element models; it provides distribution as well as maximum values of displacements and strains. The method is extremely robust (Schmidt, Tyson,

& Galanulis, 2003). It has wide dynamic range and is not affected by rigid body motions, ambient vibrations, etc. Figure B2 shows a common setup of the ARAMIS 3D correlation system. Each image can be analyzed to locate fracture points, stress zones and failure points.

Table 2.1 shows the capability of the ARAMIS System.

Frame Rate	60Hz to 480Hz
Camera Resolution	2358 x 1728 px
Measuring Area	mm <sup>2</sup> to > m <sup>2</sup>
Strain Measuring Range	0.01 % up to >100%
Strain Measuring Accuracy	up to 0.01 %
ARAMIS Software Version	6.0.2

Table 2.1 Capability of the ARAMIS System.

**2.6.2 ARAMIS Calibration.** Calibration is a process during which the measuring system, with the help of calibration objects, is adjusted such that the dimensional consistency of the measuring system is ensured. During calibration, the image characteristics of the lenses (e.g., focus, lens distortions) and the sensor configuration are determined; the distance of the cameras and the orientation of the cameras to each other are determined. Based on these settings, the software calculates from the reference points of the calibration object in the 2D camera image their 3D coordinates. The calculated 3D coordinates are then “calculated back” again into the 2D camera images. Based on position of the reference points, this data can be used to determine the so-called reference point deviation (intersection error). The calibration deviation is calculated from the average reference point deviation of all points recorded during the calibration process. A predetermined measuring volume is used to calculate all calibrations based off the size of the sample being tested (*Aramis User Manual-Software*, 2007).

Two camera images are taken simultaneously during the testing. To ensure accuracy of the images captured, calibration of the system must be completed before each test. The cameras were calibrated for this study at a distance of 140.868 mm and 140.843 mm with a certification

temperature and a measurement temperature of 68°F. Calibration deviation was 0.017 pixels, a camera angle of 14.4° and a measuring volume of 214.88 x 160.02 x 150.114 mm with a height variance of 25.4 mm; all within accuracy acceptable for the system.

**2.6.3 ARAMIS Sample Preparation.** Each sample was cleaned with isopropyl alcohol and acetone to remove contaminants such as oil and dust. Each panel was painted with Krylon™ flat white paint until samples were completely covered with no aluminum showing. A black speckled pattern was applied to the top of the white paint with Krylon™ flat black paint. Each sample was dried on a flat surface. The bolt holes, used to grip each sample, were masked off during painting and cleaned with isopropyl alcohol before testing.

## **2.7 Tensile Testing**

The evaluation of the mechanical behavior of a sample under conditions of tension and compression can be performed to provide basic material property data that is critical for component design and service performance assessment. A tensile test is a method for determining behavior of materials under axial tensile loading. For this study, the tests were conducted by fixturing the specimen into the test apparatus and then applying a force to the specimen by separating the testing machine crossheads. The crosshead speed can be varied to control the rate of strain in the test specimen. Data from the test are used to determine ultimate tensile strength, yield strength, and modulus of elasticity. Measurement of the specimen dimensions after testing also provides reduction of area and elongation values to characterize the ductility of the material (*Handbook for Analytical Methods for Materials*, 2010). A typical specimen has enlarged ends or shoulders for gripping. The important part of the specimen is the gage section. The cross-sectional area of the gage section is reduced relative to that of the remainder of the specimen so that deformation and failure will be localized in this region. The

gauge length is the region over which deformation measurements are made and is centered within the reduced section. The distances between the ends of the gauge section and the shoulders should be great enough so that the larger ends do not constrain deformation within the gauge section, and the gauge length should be great relative to its diameter or thickness (Davis, 2004). Figure B3 shows the tensile test machine used in this study. Figure 2.4 shows an isometric image of tensile test specimens used in this study. Figure 2.5 shows actual tensile specimens used for tensile testing of a SR-FSW with a FPW.

The tensile test results provide information on the deformation characteristics on the SR-FSW FPW specimens under load, which was used to evaluate stress-strain relations in the material and strain to failure. Additionally the tensile tests were used to evaluate the ultimate strength of the joint and the stress level at the onset of yielding.

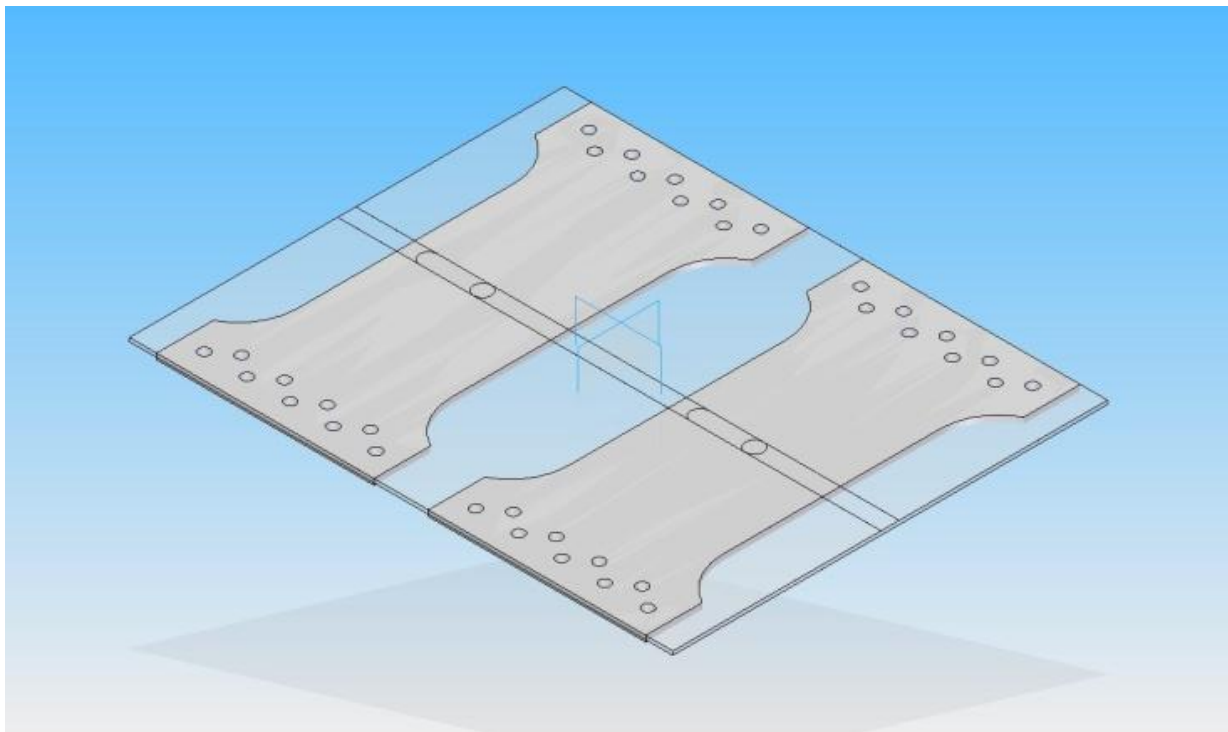


Figure 2.4 Isometric rendering of 215.9 mm test panels.

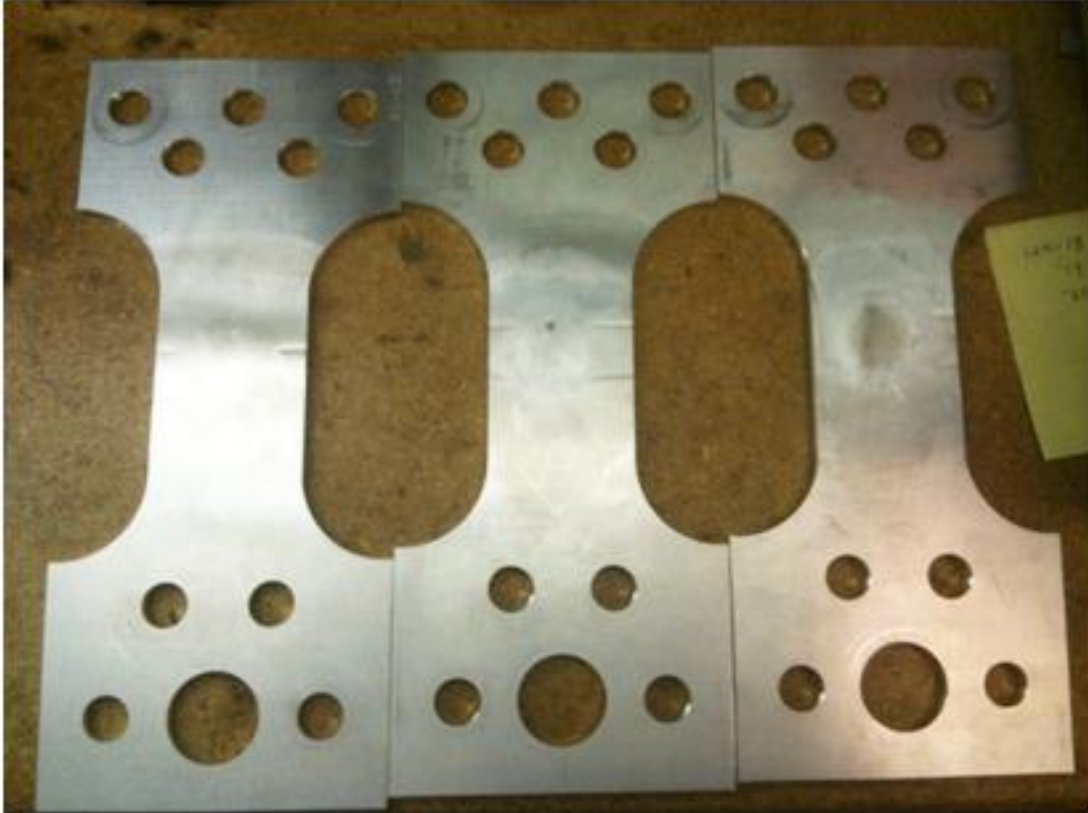


Figure 2.5 Photograph of 101.6 mm wide test panels with the bolt hold grips on top and bottom.

The tensile force is recorded as a function of the increase in gage length. Engineering stress, or nominal stress,  $\sigma$ , is defined as

$$\sigma = F/A_0 \quad (2.1)$$

where  $F$  is the tensile force and  $A_0$  is the initial cross-sectional area of the gage section.

Engineering strain, or nominal strain,  $\epsilon$ , is defined as

$$\epsilon = \Delta L/L_0 \quad (2.2)$$

where  $L_0$  is the initial gage length and  $\Delta L$  is the change in gage length, defined as

$$\Delta L = (L - L_0) \quad (2.3)$$

When a solid material is subjected to small stresses, the bonds between the atoms are stretched. When the stress is removed, the bonds relax and the material returns to its original

shape. This reversible deformation is called *elastic deformation*. At higher stresses, planes of atoms slide over one another. This deformation, which is not recovered when the stress is removed, is termed *plastic deformation*. For most metals, the initial portion of the curve is linear. The slope of this linear region is called the *elastic modulus* or *Young's modulus*,  $E$ , defined as

$$E = \sigma/\varepsilon \quad (2.4)$$

When the loads are low, the specimens are expected to respond in a linear elastic manner and when the stress rises high enough, the stress/strain behavior will cease to be linear and the strain will not disappear completely on unloading. The strain that remains is called plastic strain. The first plastic strain usually corresponds to the first deviation from linearity. Once plastic deformation has begun, there will be both elastic and plastic contributions to the total strain,  $\varepsilon_T$ .

This can be expressed as

$$\varepsilon_T = \varepsilon_e + \varepsilon_p \quad (2.5)$$

where  $\varepsilon_p$  is the plastic contribution and  $\varepsilon_e$  is the elastic contribution (Davis, 2004).

Both the 101.6 mm and 215.9 mm samples tested for this study were tested on a 900 kN MTS 880 servo hydraulic uniaxial load frame. The 101.6 mm wide samples were tested at room temperature and in liquid nitrogen (-196°C). The 215.9 mm wide samples were tested at room temperature. All samples tested at room temperature were also tested using the ARAMIS system. A 50.8 mm extensometer was attached to the side of the 101.6 mm wide samples, centered across the weld. Strain gages were fixed to the top and bottom of the plug on the back side of some of the samples across the interface. The gages were 6.35 mm length with a  $\pm 3\%$  strain range. The gages were attached with M Bond 200 catalyst and M Bond 200 adhesive. The



strain gage adhesive was allowed to cure for 12-18 hours. The application of paint to the surface of the specimens for ARAMIS was completed 24 hours after gages were applied. Strain gage, force and extensometer data were collected in ARAMIS and externally on a separate acquisition system.

A summary of test samples by sample identification, configuration and test environment for the weld 101.6 mm wide samples is provided in Table 2.2. A summary for the 215.9 mm and 215.9 mm wide overlap samples is provided in Table 2.3. Test results for all samples are provided in Chapter 3.

Sample ID	Sample Width (mm)	Plug Size	Configuration	ARAMIS Included	Temperature	PWHT
CB-179	25.4	N/A	Initial	N	Room	N
CB-180	25.4	N/A	Initial	N	Room	N
CB-181	25.4	N/A	Initial	N	Room	N
CB-182	25.4	N/A	Initial	N	Room	N
CB-183	25.4	N/A	Initial	N	Room	N
CB-184	25.4	N/A	Initial	N	Room	N
CB-185	25.4	N/A	Initial	N	Room	N
CB-179-P1	101.6	M3	Plug Weld	Y	Room	Y
CB-179-P2	101.6	M3	Plug Weld	Y	Room	N
CB-179-P3	101.6	M3	Plug Weld	Y	Room	Y
CB-180-P1	101.6	M3	Plug Weld	Y	Room	N
CB-180-P2	101.6	M3	Plug Weld	Y	Room	Y
CB-181-P3	101.6	M3	Plug Weld	Y	Room	Y
CB-183-P1	101.6	M5	Plug Weld	Y	Room	Y
CB-183-P2	101.6	M5	Plug Weld	Y	Room	N
CB-183-P3	101.6	M5	Plug Weld	Y	Room	Y
CB-184-P1	101.6	M5	Plug Weld	Y	Room	N
CB-184-P2	101.6	M5	Plug Weld	Y	Room	Y
CB-184-P3	101.6	M5	Plug Weld	Y	Room	N
CB-181-P1	101.6	M3	Plug Weld	N	LN <sub>2</sub>	Y
CB-181-P2	101.6	M3	Plug Weld	N	LN <sub>2</sub>	N
CB-182-P1	101.6	M3	Plug Weld	N	LN <sub>2</sub>	N
CB-182-P2	101.6	M3	Plug Weld	N	LN <sub>2</sub>	Y
CB-182-P3	101.6	M3	Plug Weld	N	LN <sub>2</sub>	N
					LN <sub>2</sub>	
CB-185-P1	101.6	M5	Plug Weld	N	LN <sub>2</sub>	Y
CB-185-P3	101.6	M5	Plug Weld	N	LN <sub>2</sub>	Y
CB-186-P1	101.6	M5	Plug Weld	N	LN <sub>2</sub>	N
CB-186-P2	101.6	M5	Plug Weld	N	LN <sub>2</sub>	Y
CB-186-P3	101.6	M5	Plug Weld	N	LN <sub>2</sub>	N

Table 2.2 Summary of test samples by sample identification, tensile test condition for the initial weld and 101.6 mm wide samples.

Sample ID	Sample Width (mm)	Plug Size	Configuration	ARAMIS Included	Temperature	PWHT
CX01-P2	215.9	M3	Plug Weld	Y	Room	Y
CX02-P2	215.9	M3	Plug Weld	Y	Room	Y
CX03-P2	215.9	M3	Plug Weld	Y	Room	Y
CX04-P2	215.9	M3	Plug Weld	Y	Room	Y
CX07-P1	215.9	M5	Plug Weld	Y	Room	Y
CX08-P1	215.9	M5	Plug Weld	Y	Room	Y
CX09-P1	215.9	M5	Plug Weld	Y	Room	Y
CX10-P1	215.9	M5	Plug Weld	Y	Room	Y
CIF37-P1	215.9	M3	Plug Weld Overlap	Y	Room	N
CIF37-P2	215.9	M3	Plug Weld Overlap	Y	Room	N
CIF38-P1	215.9	M3	Plug Weld Overlap	Y	Room	N
CIF38-P2	215.9	M3	Plug Weld Overlap	Y	Room	N

Table 2.3 Summary of test samples by sample identification, tensile test condition for the 215.9 mm weld and 101.6 mm samples 215.9 mm wide overlap samples.

## Chapter 3 Results and Discussion

This chapter details the results and discussion of SR-FSW between two dissimilar aluminum alloys. The first section details the results of NDE, microstructure, hardness profiles and strength testing of an initial SR-FSW formed between an AA2014-T6 plate on the advancing side and an AA2219-T87 plate on the retreating side. The second section details the results of NDE, microstructure, hardness profiles strength testing, ARAMIS and FEA of a SR-FSW of AA2014-T6 and AA2219-T87 with the addition of an AA2219 FPW. SR-FSW process parameters are identical for the 101.6 mm and the 215.9 mm wide samples with a decrease in spindle speed for the 215.9 mm wide overlap panels.

### 3.1 Initial Weld

**3.1.1 NDE.** Phased array ultrasonic inspection was completed on the SR-FSW panels, before they are machined into individual specimens, scanning the crown, root and volume of the panel, using the techniques described in Section 2.2. Inspection revealed four panels that exhibited a volumetric indication located on the advancing pin-tool area suggesting a defect in the advancing nugget bulge or a minor wormhole within the volume of the panel. One panel exhibited root flaws and one exhibited crown flaws. The flaws detected in the crown and root areas were undefined in type. The largest flaw reported was located within the weld approximately 5.59 mm from the advancing side of the weld. Flaw severities are reported as a percentage of reflected ultrasonic input energy returned to the transducer. A larger percentage indicates a more severe defect. One flaw had amplitude of 18.04% and was the longest detected in the panels of 510.79 mm. This flaw is in 2/3 of the length of the weld. Other samples produced volumetric flaws of 10.98% and 15.59% shown in Table 3.1 along with root and crown

flaws indicated. All flaws were found in the 215.9 mm samples. No flaws were detected by phased array ultrasonic inspections of the initial welds of the 215.9 mm overlap samples or the 101.6 mm wide samples. Output from the ultrasonic inspection is shown in Figures C1-C3 in Appendix C. Flaws were within acceptable limits to be used within this study.

Panel	# of Indications	Location	Defect Length(mm)	Weld Width*(mm)	From Adv Side (mm)	Amplitude (%)
CX01	1	Root	6.02	19.05	7.47	9.41
	2	Root	5.99		7.72	5.10
	3	Root	5.99		7.19	5.10
CX02	1	Crown	29.0	19.05	9.07	16.47
CX07	1	Volume	191	19.43	6.4	12.16
CX08	1	Volume	337	19.35	4.29	10.98
CX09	1	Volume	447	19.25	6.93	15.59
CX10	1	Volume	511	19.15	5.59	18.04

Table 3.1 Phased array ultrasonic inspection results. \*Weld widths are given for the crown side of the panel. Width is reported from shoulder to shoulder.

**3.1.2 Macrographs and Hardness Profiles.** Macroscopic images of the cross-section of the initial weld are shown in Figure 3.1. In this figure, AA 2014 is on the advancing side and AA 2219 on the retreating side. Figure 3.2 shows the HAZ, TMAZ and nugget region of the welds. Additionally the dispersed interface is readily visible in the macrograph.



Figure 3.1 Macrograph of initial weld.

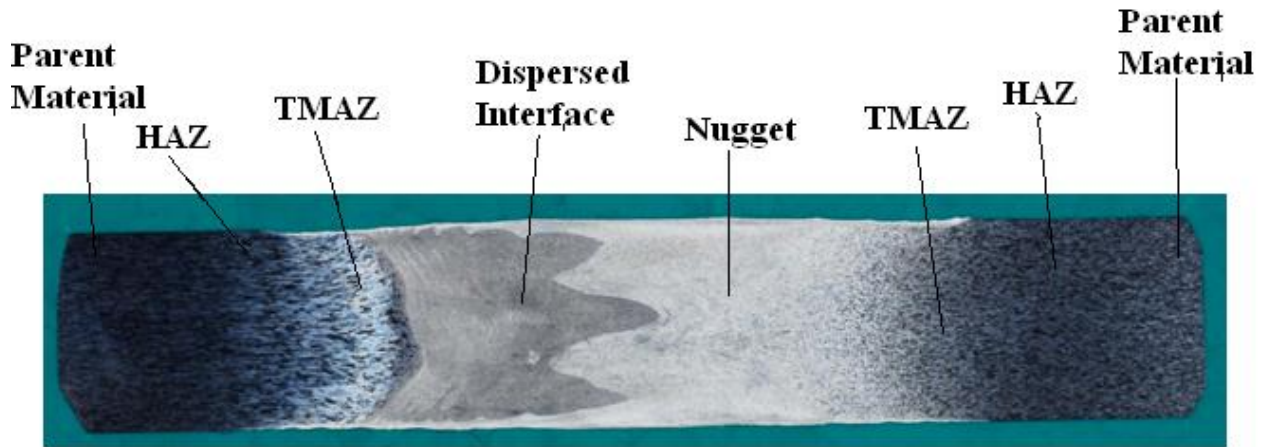


Figure 3.2 Defined HAZ and TMAZ of the advancing side to the left of the dispersed interface within the nugget, retreating side TMAZ and HAZ to the right.

The shape of the dispersed interface is determined by the mechanical action of the pin-tool. The threading in the pins pushes the material up and down creating a ring vortex circulation (RVC) which has local creeping motion. As shown in Figure 3.3, there are three ring vortices created around the diameter of the pin-tool, at the top, middle and bottom of the weld joint. Each vortex plays a role in the development of the weld zone. The pressure due to the constraint imposed by the top and bottom shoulder during the SR-FSW process causes the material to stick along the shaft.

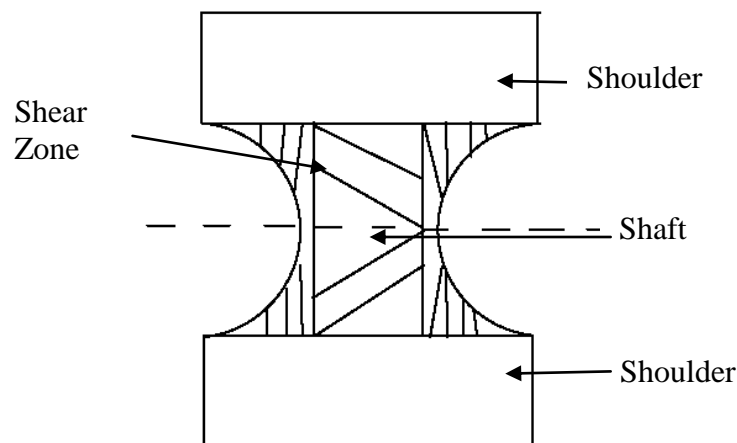


Figure 3.3 Representation of pin tool and ring vortices of a SR-FSW.

Figure 3.4 shows the pin-tool traveling down the weld; material from the advancing side is captured and is buried under additional material from the advancing side, then further buried by material on the retreating side.

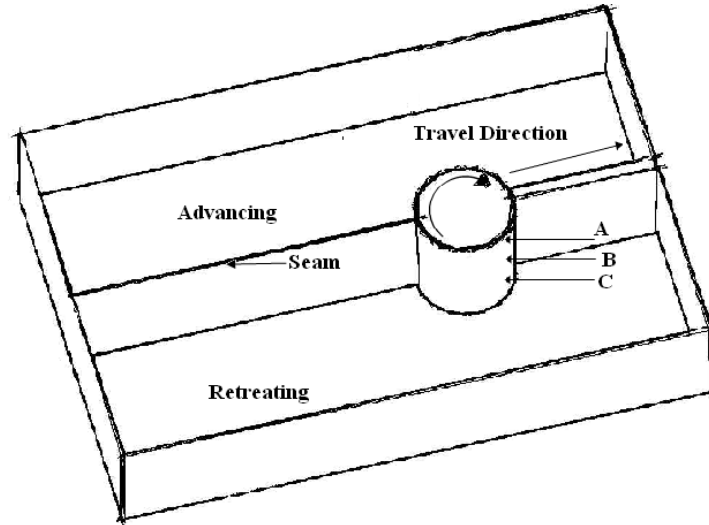


Figure 3.4 Schematic showing the travel direction, rotation and location of vortices.

As the pin-tool rotates, the retreating material is re-deposited followed by the advancing material. The material that passes through the ring vortex circulation (RVC) is subjected to the shear zone. The material closest to the pin-tool produces fine grains in the nugget. As material moves toward the outside of the ring vortex, it is subjected to the heat produced by the annihilation of the dislocations and the movement of the pin-tool in the TMAZ area. Beyond the RVC, the material is subjected to heat, thereby creating the HAZ. The three ring vortices are shown in Figure 3.5. The RVC-A creates an inward motion allowing the material from the retreating side to stay on the pin-tool longer allowing for a greater mixture of the two materials. The stream line is moved further into the retreating side. RVC-B creates an outward motion which deposits the retreating material sooner than material from RVC-A. RVC-C produces an inward circulation similar to that of RVC-A. The dispersed interface advancing material is extremely fine material that has passed through the shear surface. This material is buried deep

under the retreating material and is deposited further into the nugget region. The grains in the TMAZ are small and elongated grains. The grains in the HAZ are coarse grains that haven't been affected by the shear zone of the pin-tool.

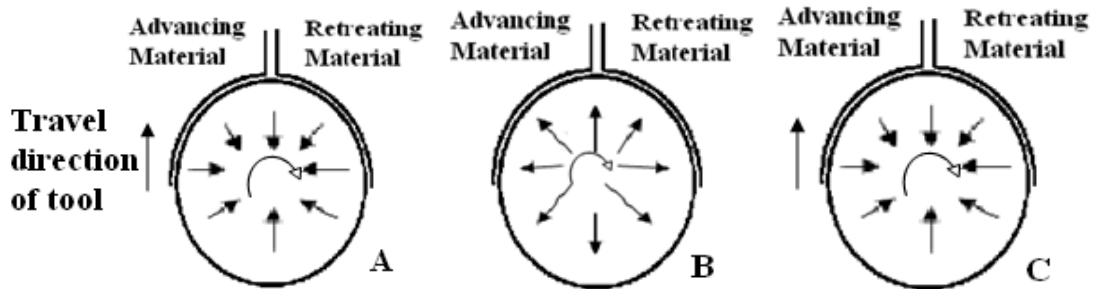


Figure 3.5 Ring vortex circulations of the SR-FSW left hand/right hand pin tool. (A) Vortex at the top of pin tool, (B) middle of pin tool and (C) bottom of the pin tool.

The macrostructure shown in Figure 3.6 shows a sharp demarcation between the HAZ and TMAZ on the advancing side of the samples. The material on the retreating side is more diffuse and the two zones are not easily distinguishable. The diffused boundary on the retreating side occurs because the retreating material is subjected to the shear zone for a shorter amount of time than the advancing side of the weld. Each sample shows a distorted seam trace with the striations from the threaded pin-tool. Vickers hardness profiles were taken across four representative samples, with two samples in the post weld heat treated (PWHT) condition. Figure 3.7 is a plot of the Vickers hardness profile across the CB-180 initial weld which fluctuates across the weld. The hardness profiles from a 700 gram Knoop and Vickers Diamond Indenters were used to resolve the HAZ and TMAZ of the retreating side which is diffused. The parent material hardness is 145 HV<sub>700g</sub> with a drop in hardness starting at the HAZ to 130 HV<sub>700g</sub>. The hardness further drops in the TMAZ to 118 HV<sub>700g</sub> with an increase representing a dispersed interface of AA2014-T6 material to 135 HV<sub>700g</sub>. The hardness then drops significantly within the nugget region to 85 HV<sub>700g</sub> followed by an increase through the retreating side TMAZ into the HAZ to 135 HV<sub>700g</sub>.



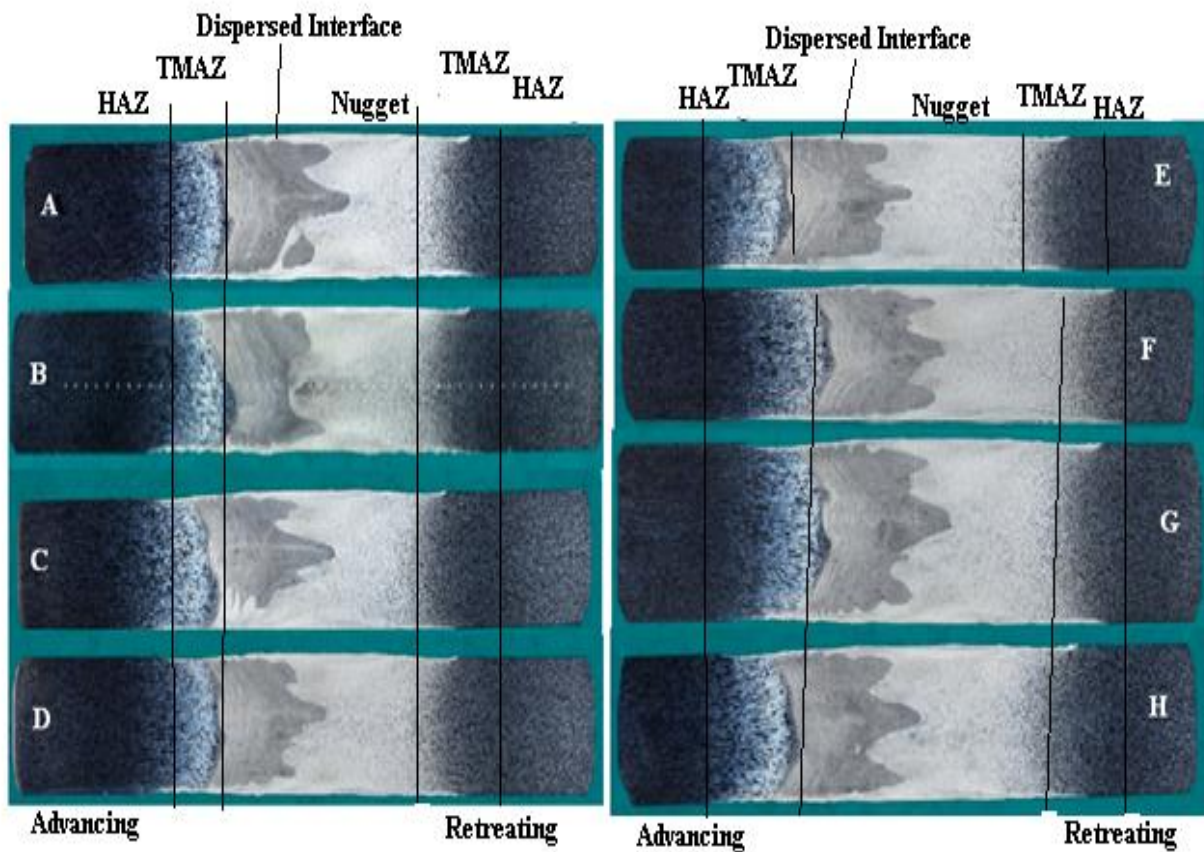


Figure 3.6 Macrographs of SR-FSW dissimilar alloys. AA 2014 is on the advancing side and AA 2219 is on the retreating side. All samples were processed with the same weld parameters. (A) CB-179, (B) CB-180, (C) CB-181, (D) CB-182, (E) CB-183, (F) CB-184, (G) CB-185 and (H) CB-186.

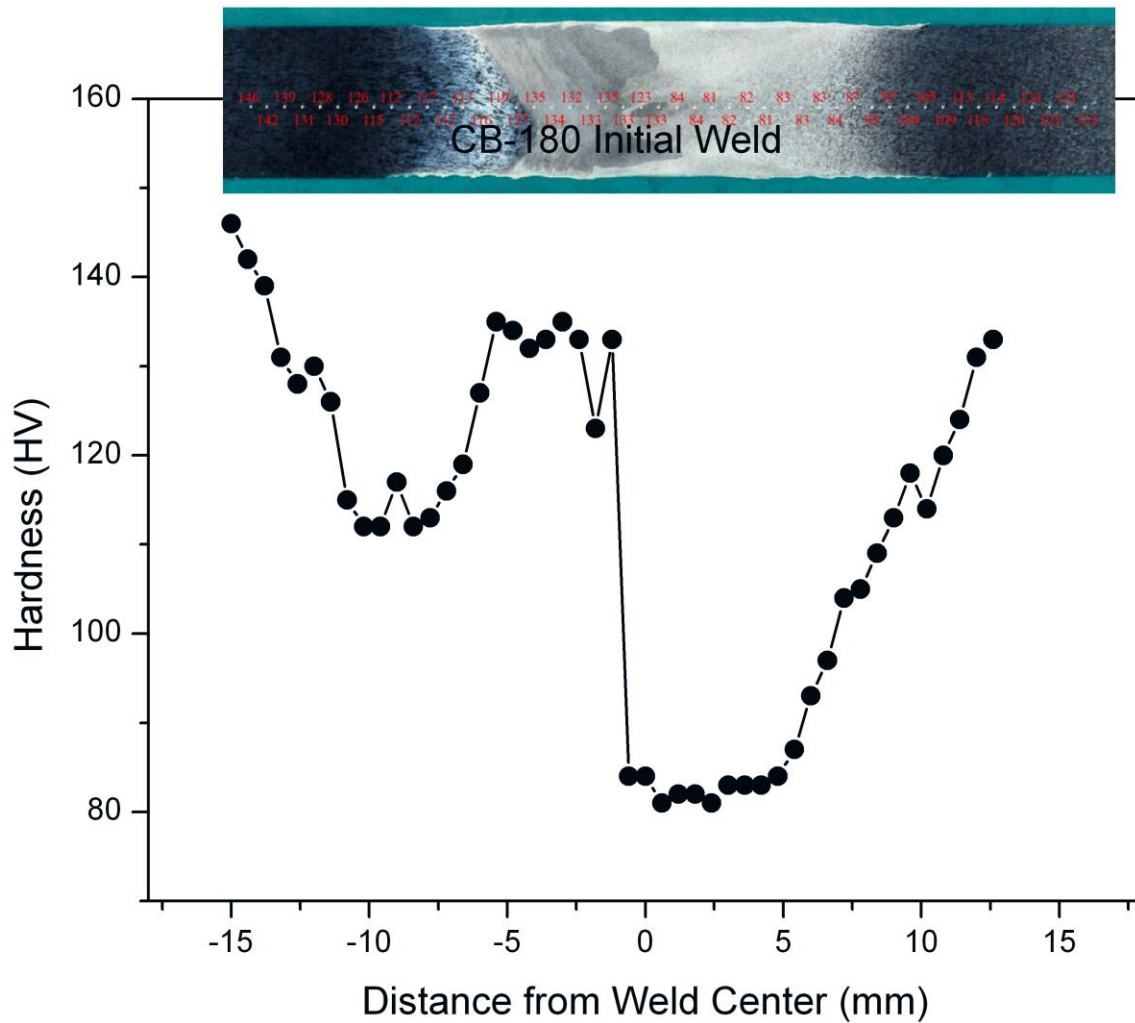


Figure 3.7 Macrograph and hardness profile of CB-180 initial weld.

Figures 3.8-3.11 show the Vickers hardness profiles of the CB-180 initial weld, CB-186 initial weld, CB-179-P1 PWHT weld and CB-183-P3 PWHT weld. The PWHT profiles show an increase in hardness in both profiles which results from aging or hardening during the PWHT cycles. Figure 3.12 shows the comparison of the PWHT versus the initial weld hardness profiles. The parent material and the HAZ are unaffected by the PWHT; the most significant changes are in the nugget region and the dispersed interface. Both of these regions exhibit a greater hardness due to refined grains or possible precipitate dissolution.

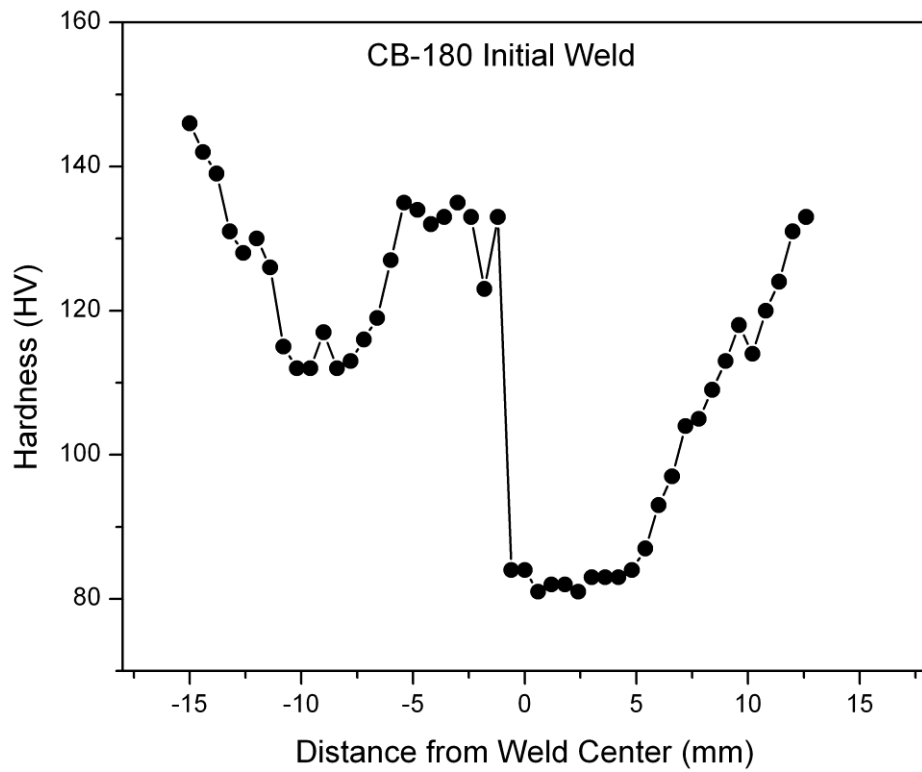


Figure 3.8 CB-180 Vickers hardness profile initial weld.

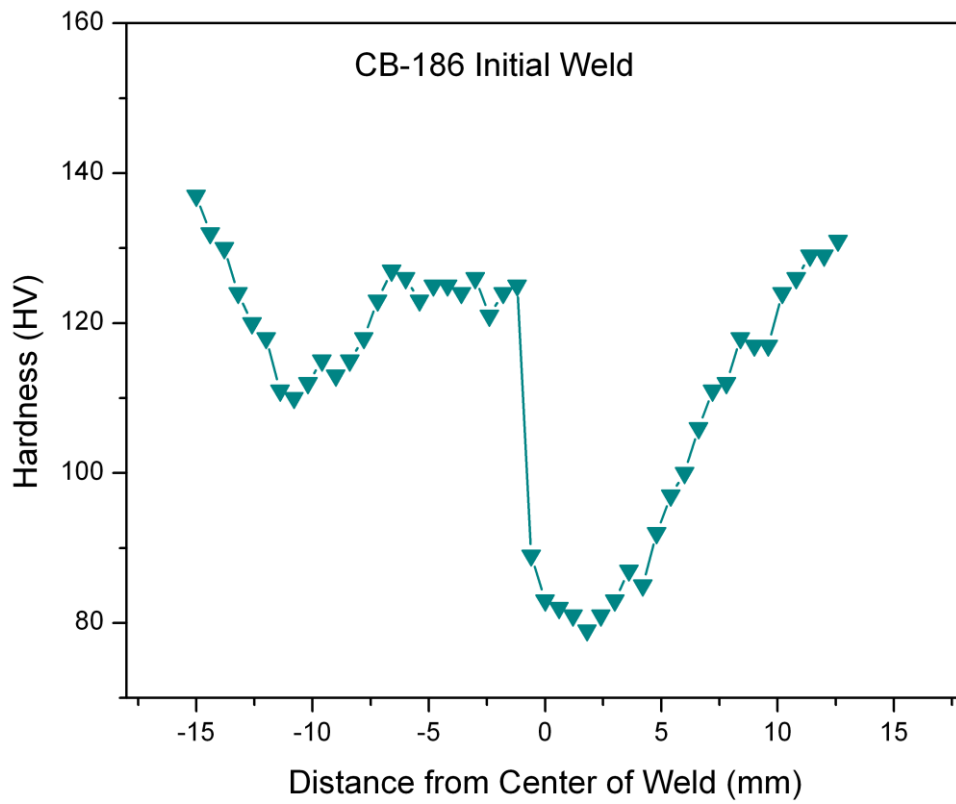


Figure 3.9 CB-186 Vickers hardness profile initial weld.

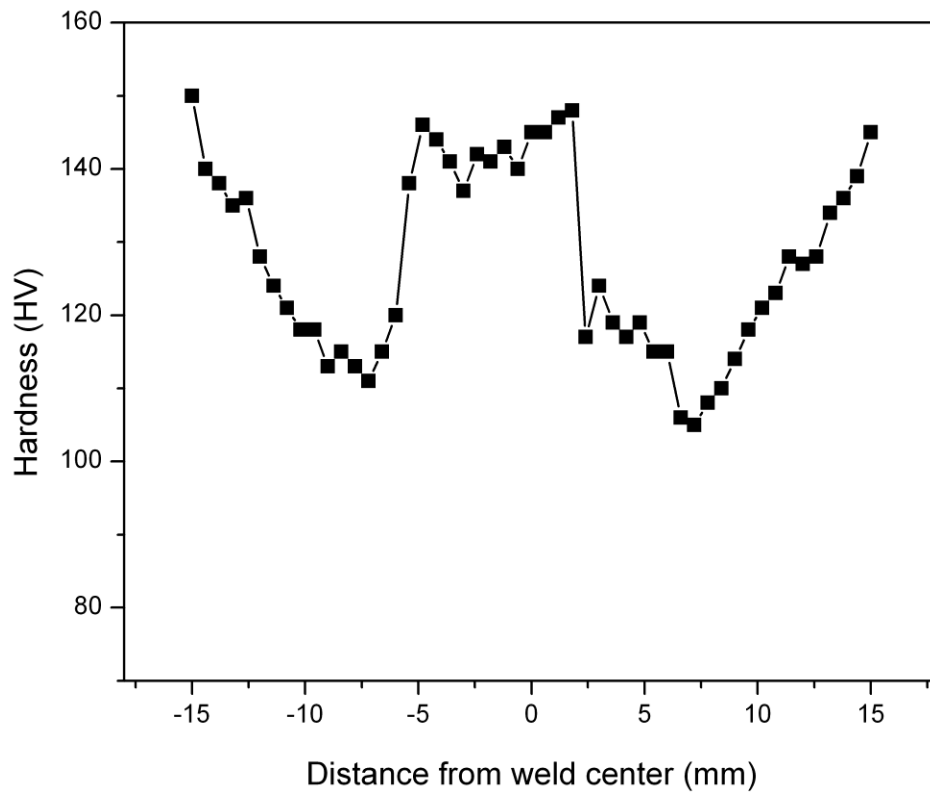


Figure 3.10 CB-179-P1 PWHT weld Vickers hardness profile.

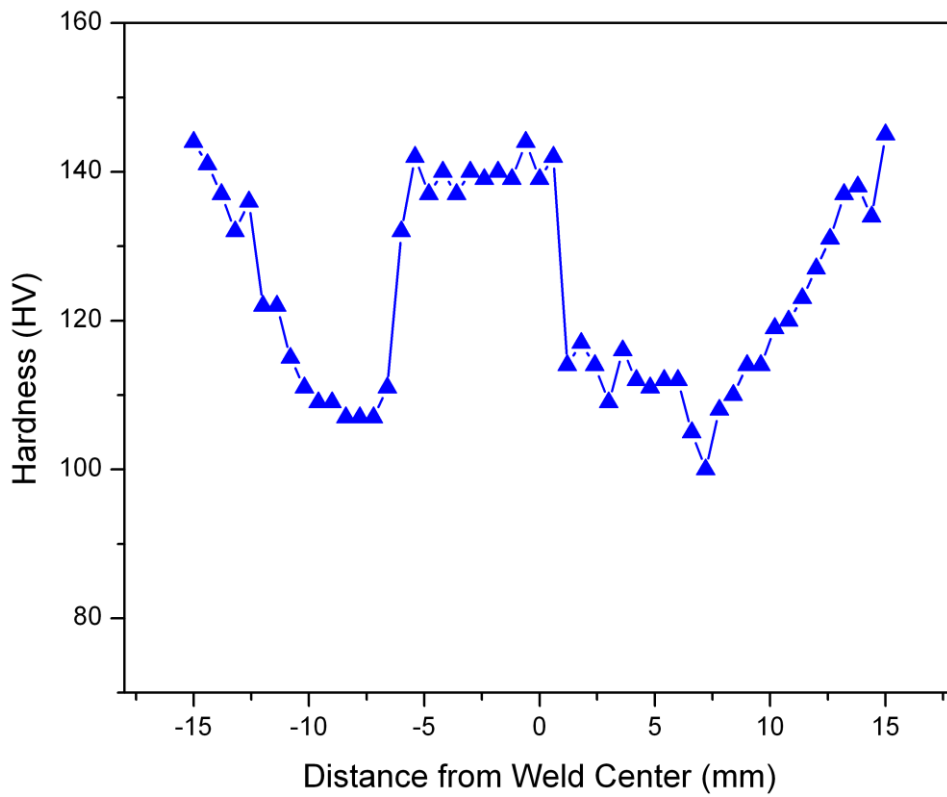


Figure 3.11 CB-183-P1 PWHT weld Vickers hardness profile.

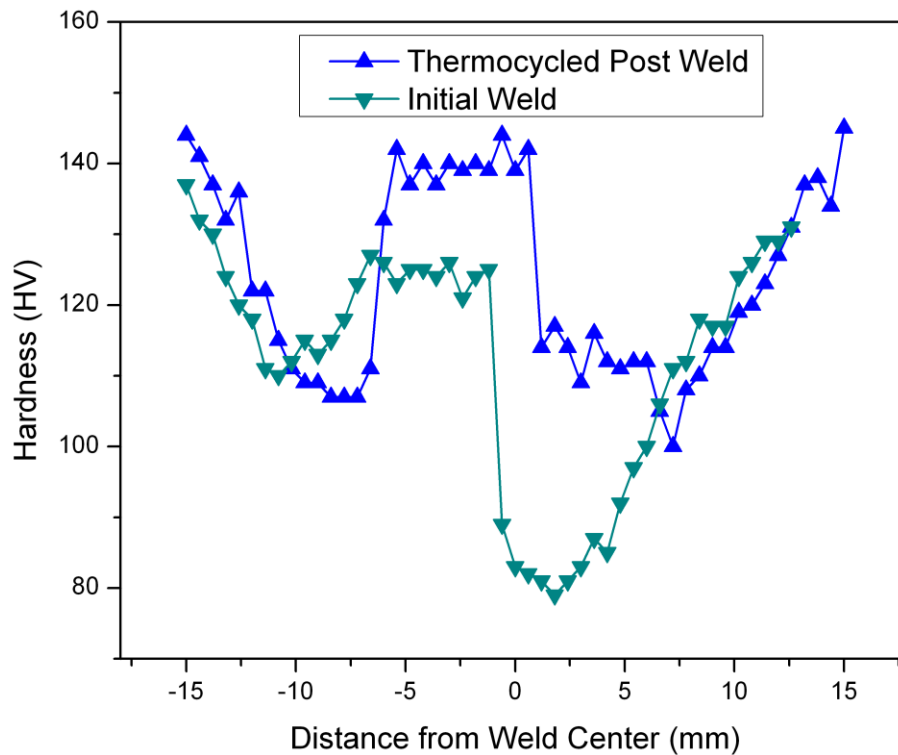


Figure 3.12 Comparison of the PWHT vs. the initial weld hardness profiles.

**3.1.3 Tensile Test.** In order to confirm the quality of the initial weld and to provide baseline weld strength for evaluating plug weld strength efficiency, tensile tests were performed on each of the weld panels. The tensile test coupons were one inch wide and were tested at room temperature under static conditions with a crosshead displacement of 1.27 mm/min. A schematic showing the location and geometry of the tensile coupon is shown in Figure 2.1. Figure 3.13 shows the schematic cross-section of the specimen.

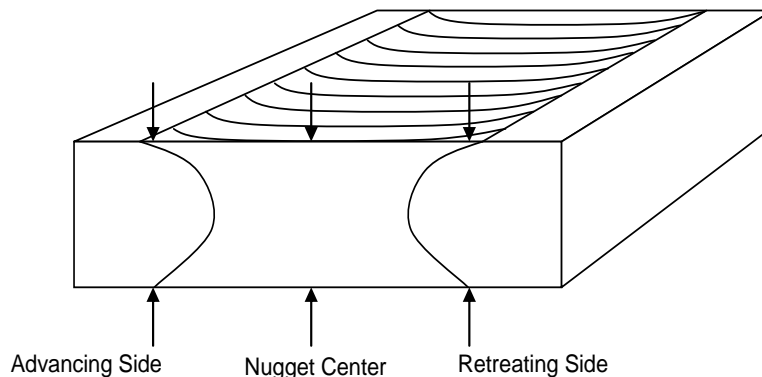


Figure 3.13 Schematic cross-section of initial weld tensile macrograph.

Table 3.2 details the specimen cross-section data, failure location and ultimate stress of the initial welds. Table 3.3 shows the statistical data.

Sample ID	Advancing Side Plate Thickness (mm)	Advancing Side Weld Thickness (mm)	Thickness at Nugget Center (mm)	Retreating Side Weld Thickness (mm)	Retreating Side Plate Thickness (mm)	Gauge Length (mm)	Location of Failure	Ultimate Stress (MPa)
CB-179	5.18	5.16	5.56	0.210	5.18	25.45	Ret	372
CB-180	5.21	5.21	5.44	5.31	5.18	25.27	Ret	368
CB-181	5.18	5.11	5.41	5.26	5.18	25.20	Ret	369
CB-182	5.21	5.08	5.46	5.28	5.18	25.30	Ret	367
CB-183	5.21	5.05	5.44	5.31	5.16	25.40	Ret	367
CB-184	5.18	5.16	5.46	5.36	5.16	25.37	Ret	371
CB-185	5.18	5.13	5.41	5.31	5.16	25.40	Ret	373
CB-186	5.11	5.16	5.38	5.26	5.13	25.35	Ret	375

Table 3.2 Initial weld tensile test data.

Test Results	Maximum	Minimum	Median	Mean	Std. Deviation (sample)	Coefficient of Variation (%)
Ultimate Strength (MPa)	375	367	370	370	3.10	0.83

Table 3.3 Initial weld statistical data.

Based on the results, the eight tensile specimens had an average ultimate strength of 370 MPa. All samples broke on the retreating side of the weld. All samples failed in the HAZ of the 2219 material. As a result of the hardness, the weaker component dictated the performance of the joint, where failure occurred in the region of the greatest hardness reduction and the smallest area, along the retreating HAZ and the nugget. The weld strength, however, exceeds the weld specification requirement minimum for ultimate tensile strength of 331 MPa.

**3.1.4 Metallography.** Light microscopy of the weld after tensile testing was used to examine the fracture surface of the initial welds. Macroscopic images reveal a ductile fracture surface on the retreating side of the weld shown in Figure 3.14.

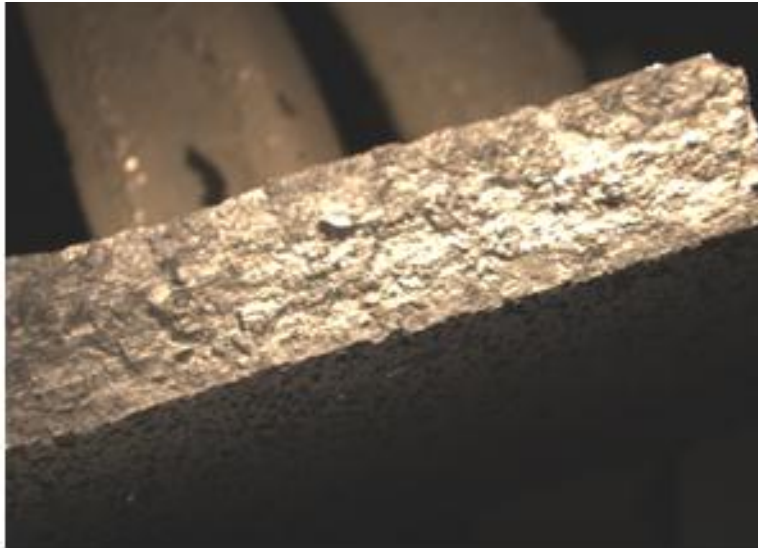


Figure 3.14 Leica MZ 16A optical light microscopy with 4.5 magnification of retreating side fracture within the AA 2219-T87 HAZ.

**3.1.5 Fractography.** Scanning electron microscopy (SEM) shows a cup cone appearance which is representative of a ductile fracture of metal material. Microscopic images shown in Figure 3.15 show the retreating side fracture in the HAZ displaying an extended region of micro dimples which can be correlated to the presence of coarse grain boundaries.

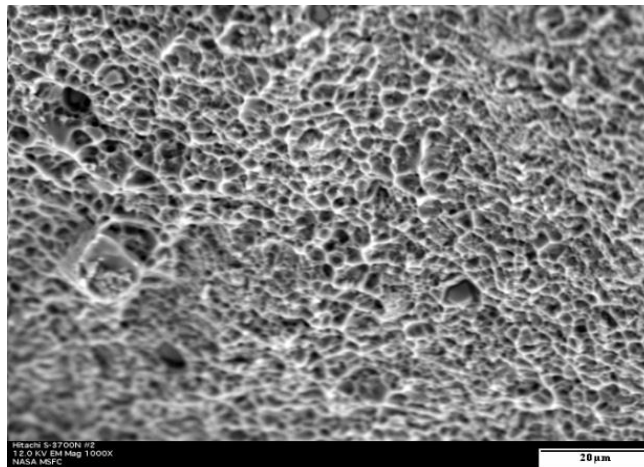


Figure 3.15 Extended regions of micro dimples on the fracture surface.

In Figure 3.16 the presence of fine particles observed inside the dimples suggests ductile transgranular fracture.

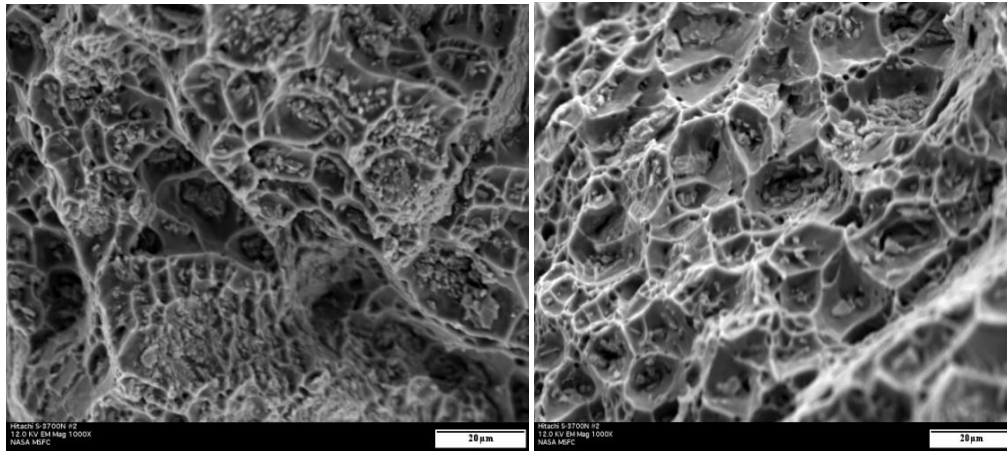


Figure 3.16 Fracture surface resultant from tensile test showing a cup cone surface at 1000x. Images taken with a Hitachi S-3700N SEM (Dion D. Jones).

The presence of a ductile fracture in the weld occurs as a result of applied stress exceeding the material yield or flow stress. Ductile fractures are usually observed away from the origin of fracture (Parrington, 2002).

### 3.2 Plug Weld

As described in Chapter 2, FPWs were placed into the initial weld panels. The plug welds were then subjected to NDE inspection. Following inspection, samples containing plugs were machined from the panels and tensile tested. Two plugs were cross-sectioned for microhardness and microstructural evaluation.

**3.2.1 NDE.** Liquid penetrant inspection was completed on the FPW panels to examine the crown and root side of the plug. Inspection revealed six panels that exhibit surface indications. Round indications were noted on the crown side of four panels with round and linear indications observed on the root side of two panels. The largest round indication was 1.27 mm in diameter and the largest linear indication was 1.27 mm long. A summary of the indications is provided in Table 3.4.



Panel ID	Plug #	Location	Size (mm)	Type
CB-183	3	Crown	1.27	Linear
CB-184	3	Root	0.508 dia.	Round
CB-186	2	Crown	1.27 dia.	Round
CIF37	2	Crown	< 0.254 dia.	Round
CIF38	1	Crown	< 0.254 dia.	Round
	2	Crown	< 0.254 dia.	Round

Table 3.4 Penetrant inspection results.

Eddy current testing indicated a sharp conductivity difference or change observed on the minor side of the plug welds at the friction stir weld to plug weld interface on the 215.9 mm overlap panels. The indication produced a response similar in appearance to crack-like indications but not as sharply defined. Base material to plug weld interface did not exhibit the same characteristic. No indications were observed on any of the 101.6 mm samples. Phased array ultrasound was repeated on the samples with no observable indications noted in the plug weld HAZ of any samples.

**3.2.2 Hardness Profile.** For two PWHT samples, cross-sections were taken across the center of the plug, 6.35 mm to the left of the center of the plug and 6.35 mm to the right of the center of the plug shown in Figure 3.17. All sections were perpendicular to the weld line.

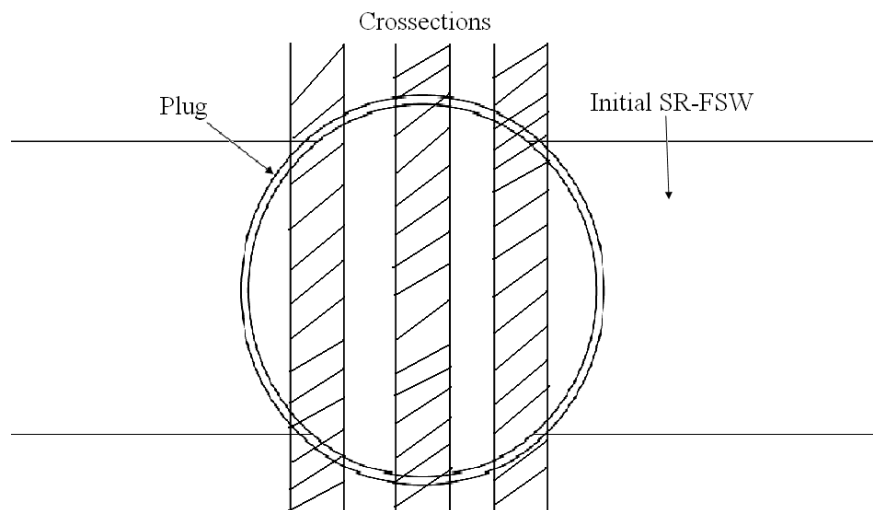


Figure 3.17 Schematic of cross-sections of FPW.

Both samples were post weld heat treated. Figure 3.18 shows macroscopic images of CB-179-P1 with a M3 (smaller diameter) plug.

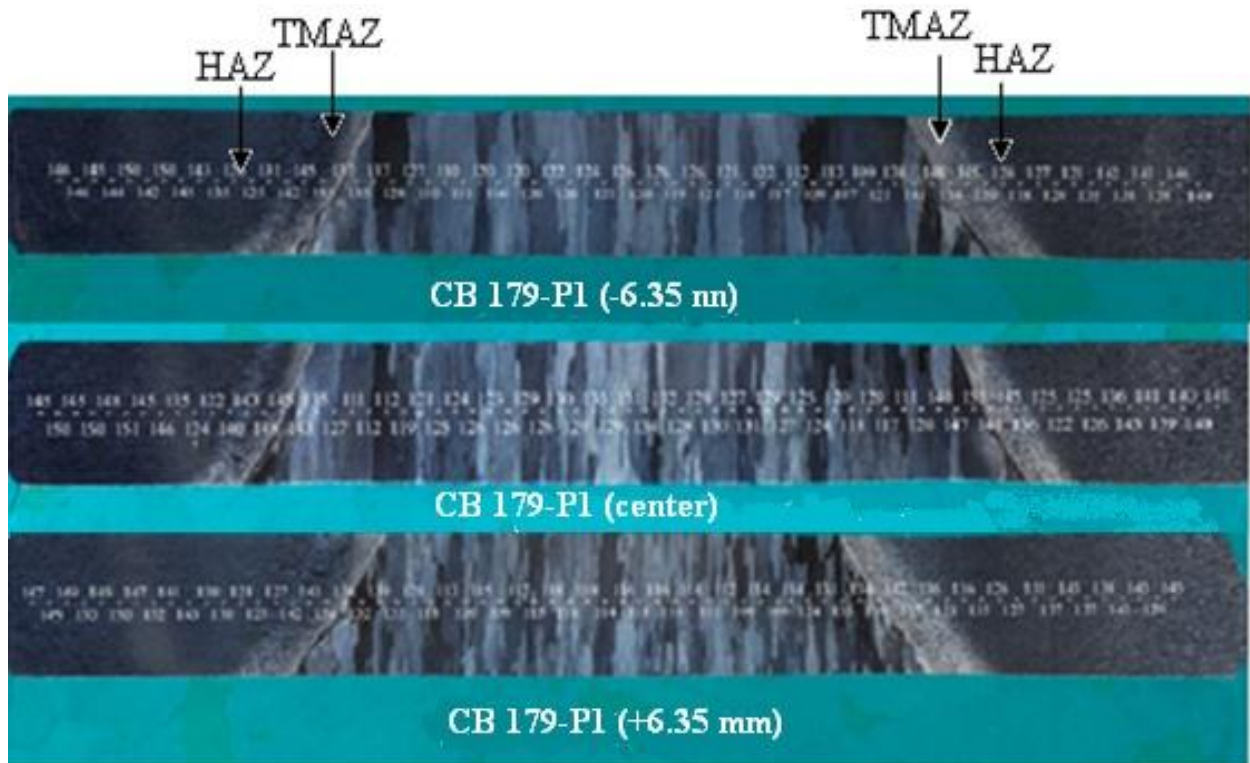


Figure 3.18 Cross-section macrographs of CB-179-P1 post weld heat treated plug welds of M3 plug major diameter side.

Figure 3.19 shows macroscopic images of CB-183-P1 with a M5 (larger diameter) plug. Macrographs show tapered plugs with a TMAZ and HAZ to the left and right of the plug with parent material to the left and right of the HAZ. The TMAZ shows distorted grains bending up and outward. Plug material grains are large pancake grains with no distortion in the plug at the boundaries. Hardness across the sample starts with the hardness values of the parent material to the outermost diameter of the plug with a decrease in hardness in the weld HAZ to 120 HV<sub>700g</sub> and an increase in hardness in the plug HAZ to 145 HV<sub>700g</sub> with a decrease in the plug TMAZ to 110 HV<sub>700g</sub>. A TMAZ is present in the parent material plug interface and with the hardness across the center of the plug increasing to an average of 125 HV<sub>700g</sub>. There is a similar behavior on the retreating side.

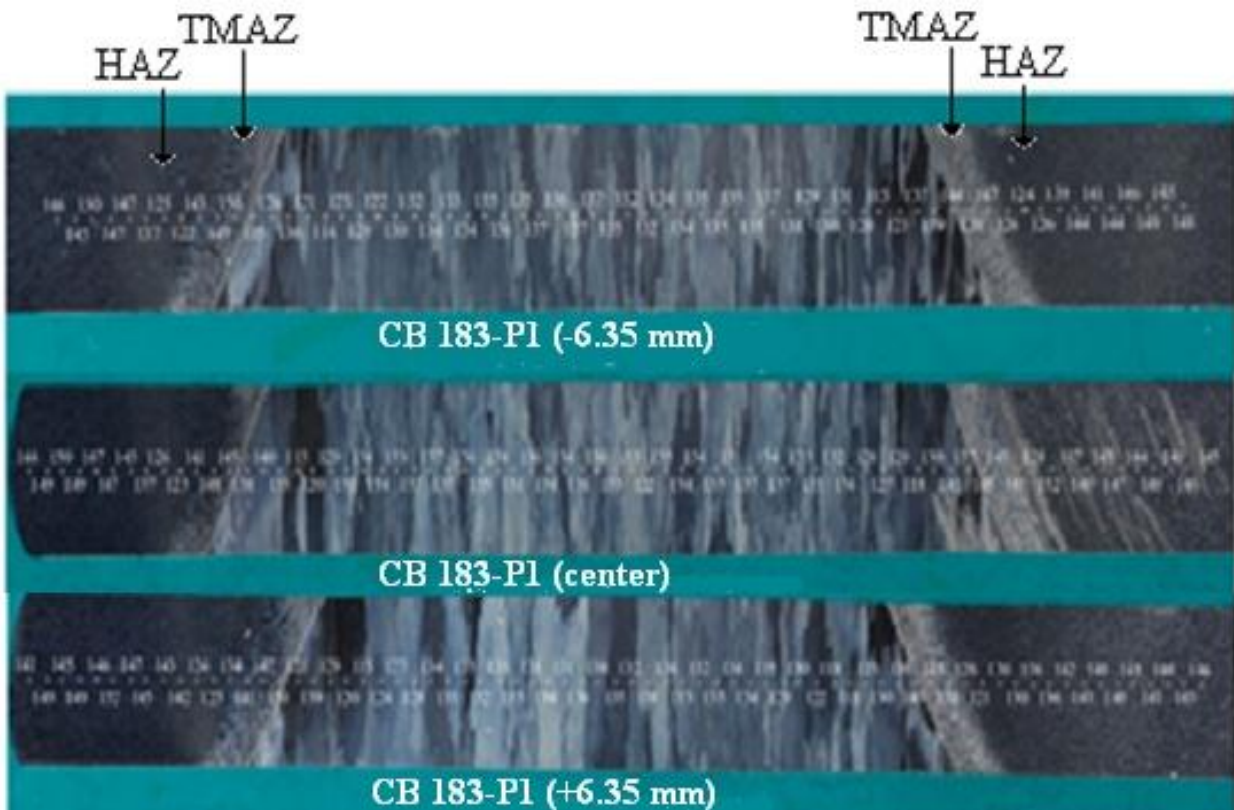


Figure 3.19 Cross-section macrographs of CB-183-P1 post weld heat treated plug welds of M5 plug major diameter side.

Figures 3.20-3.23 show a variation in the hardness profile across the three sub sections of CB-179-P1 whereas there is little noticeable variation in the subsets of CB-183-P1 in Figures 3.24-3.27 due to the larger diameter. The left and right cross-sections are similar to the center weld for CB-183-P1, which includes more of the plug as a result of the larger diameter plug.

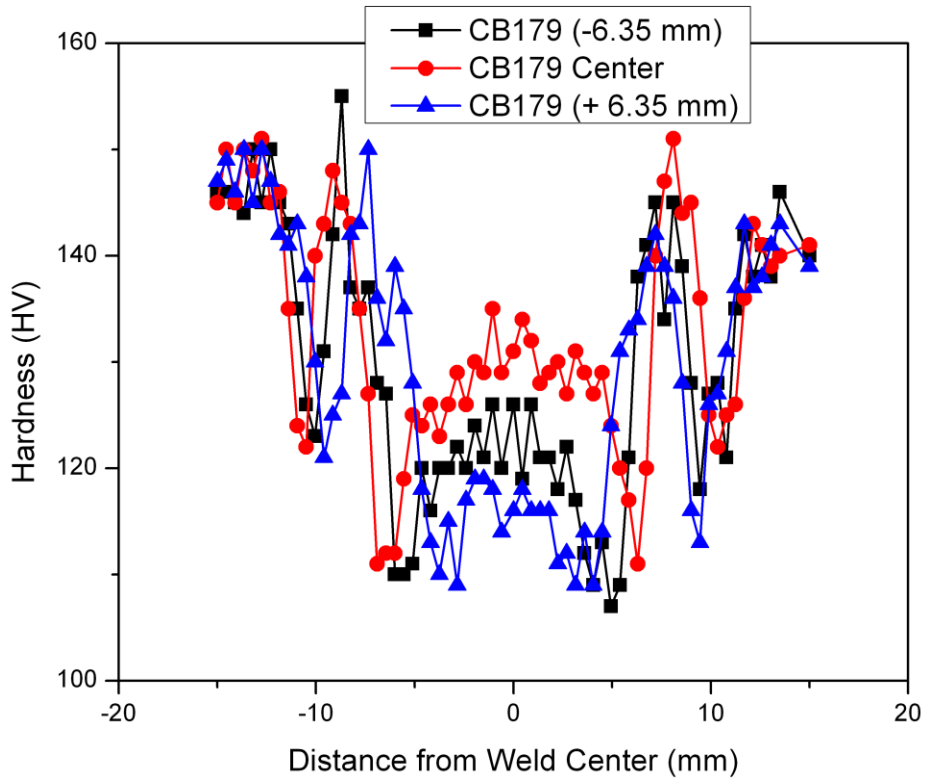


Figure 3.20 Variations in the hardness profile across the three sub sections of CB-179-P1.

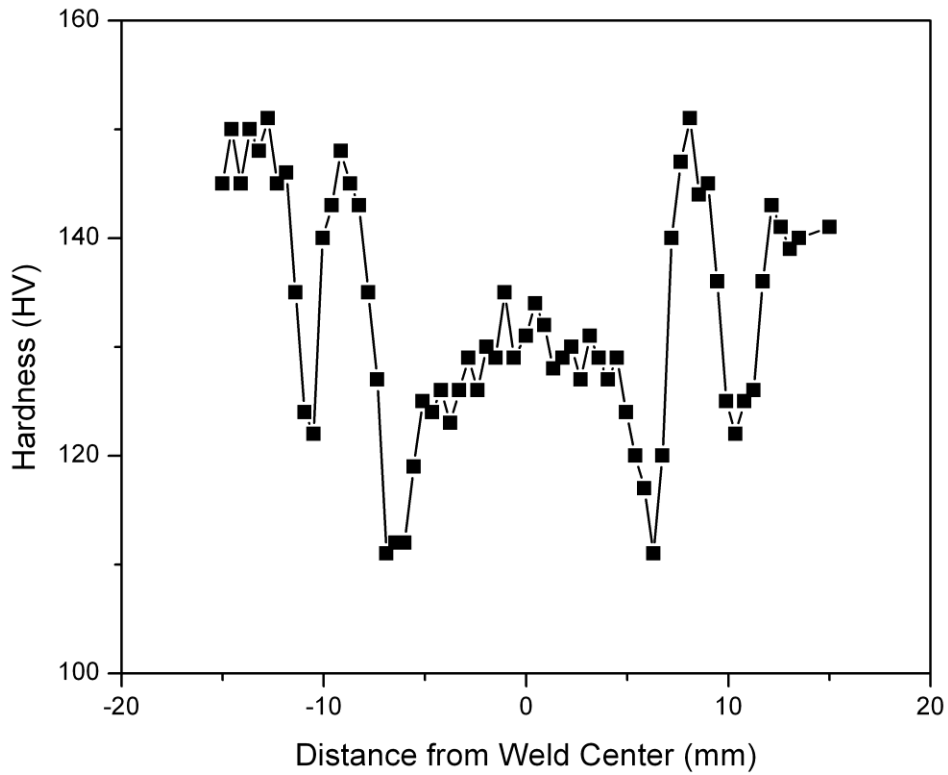


Figure 3.21 Hardness profile across the center of CB-179-P1.

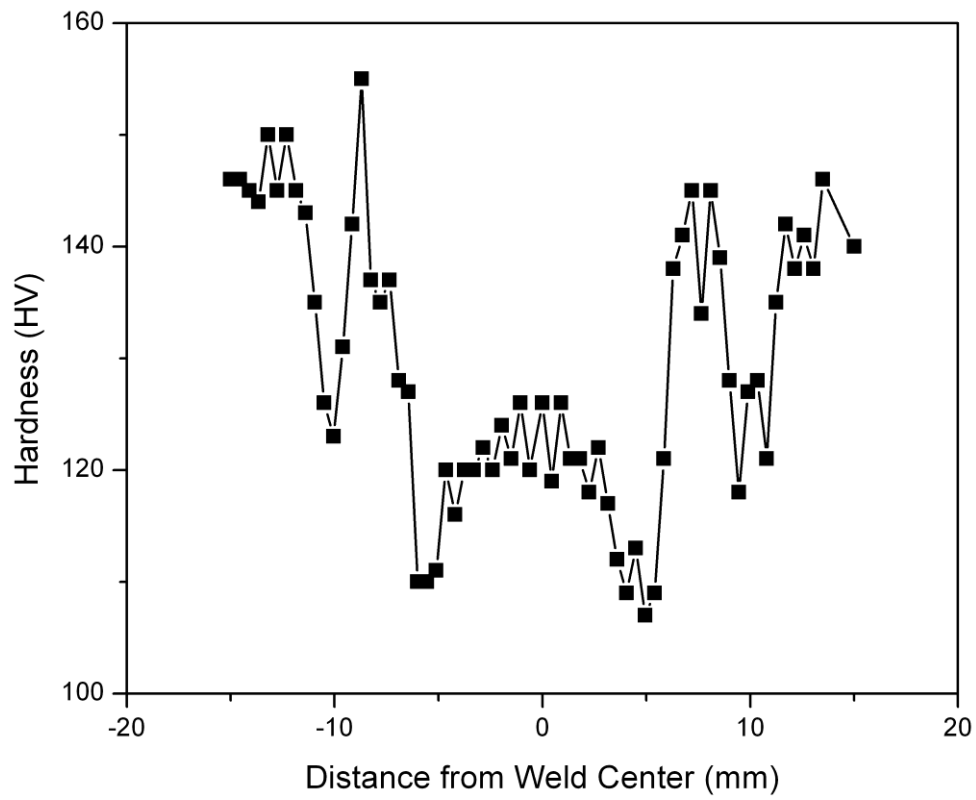


Figure 3.22 Hardness profile across the left of center of CB-179.

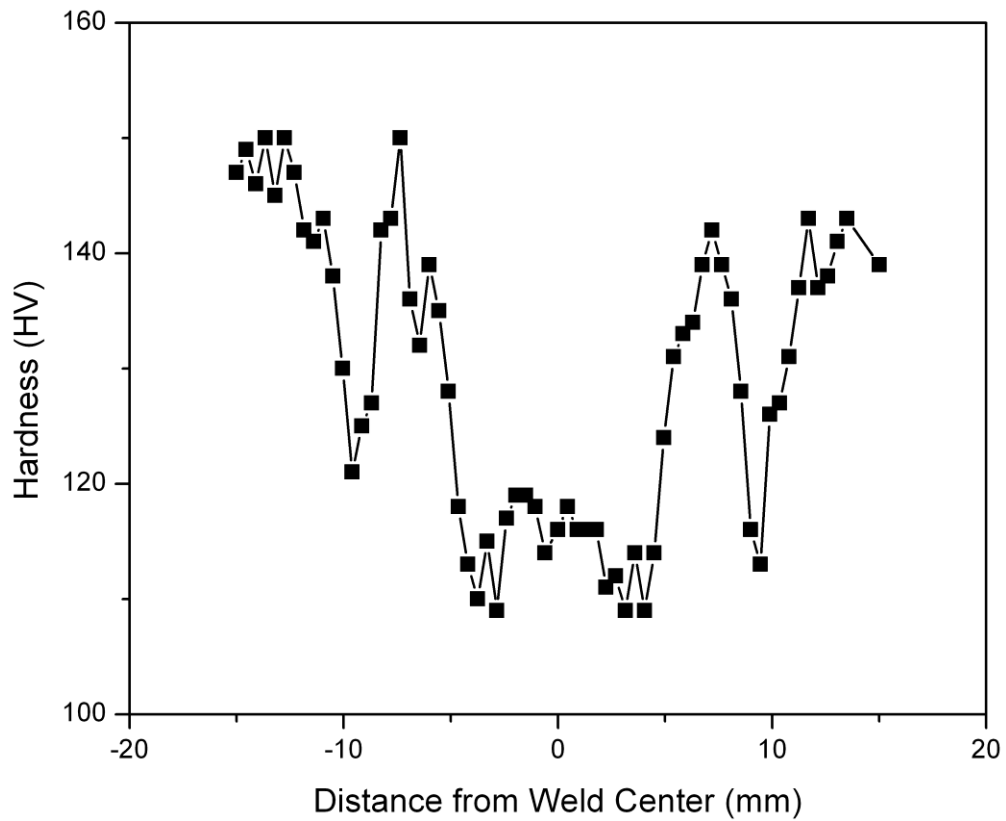


Figure 3.23 Hardness profile across the right of center of CB-179-P1.

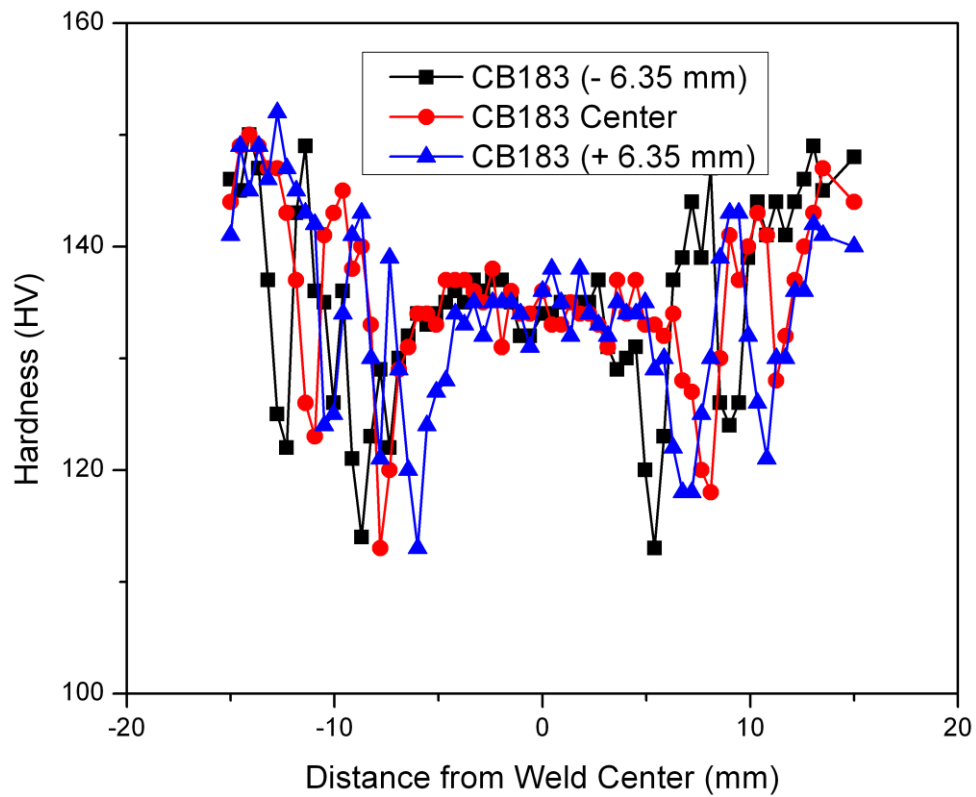


Figure 3.24 Comparative hardness profiles of CB-183-P1.

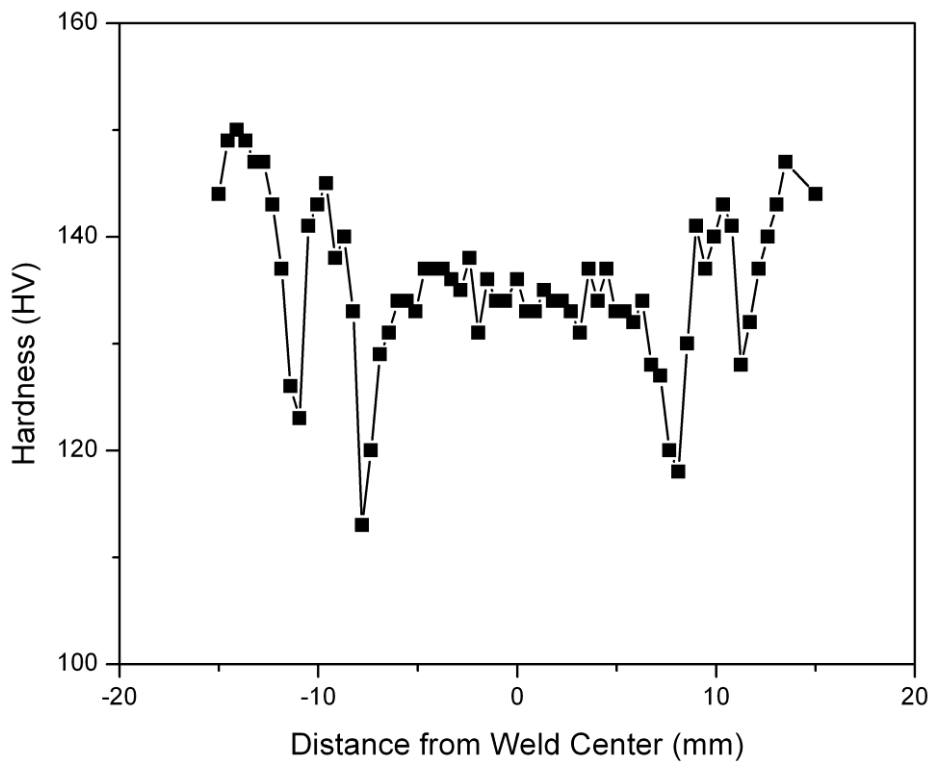


Figure 3.25 Hardness profile across the center of CB-183-P1.

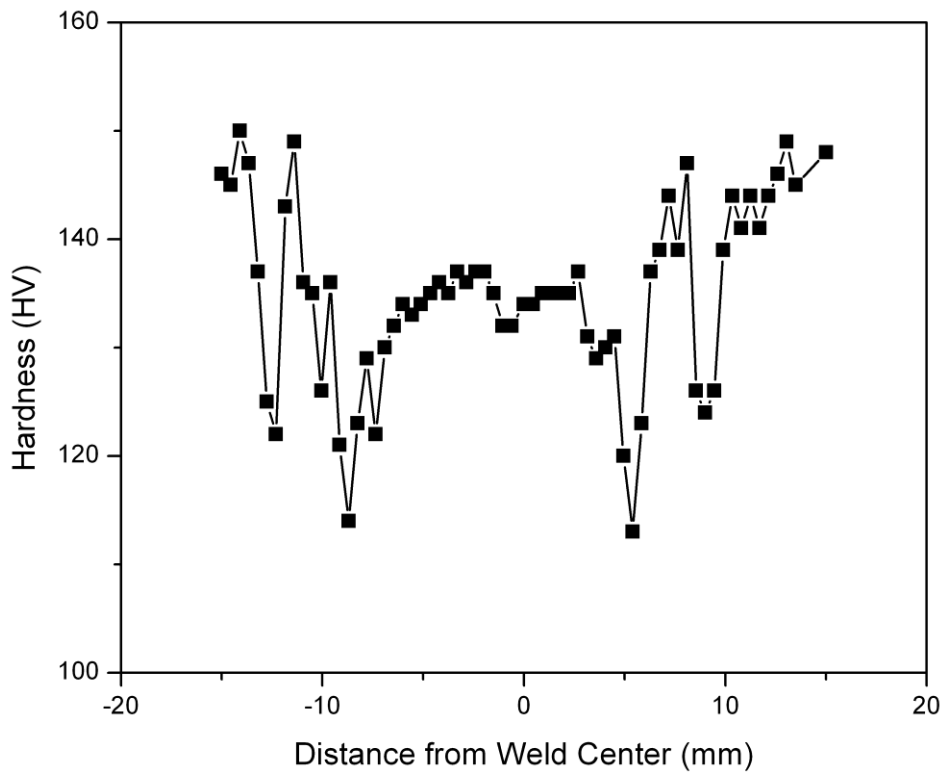


Figure 3.26 Hardness profile across the left of the center of CB-183-P1.

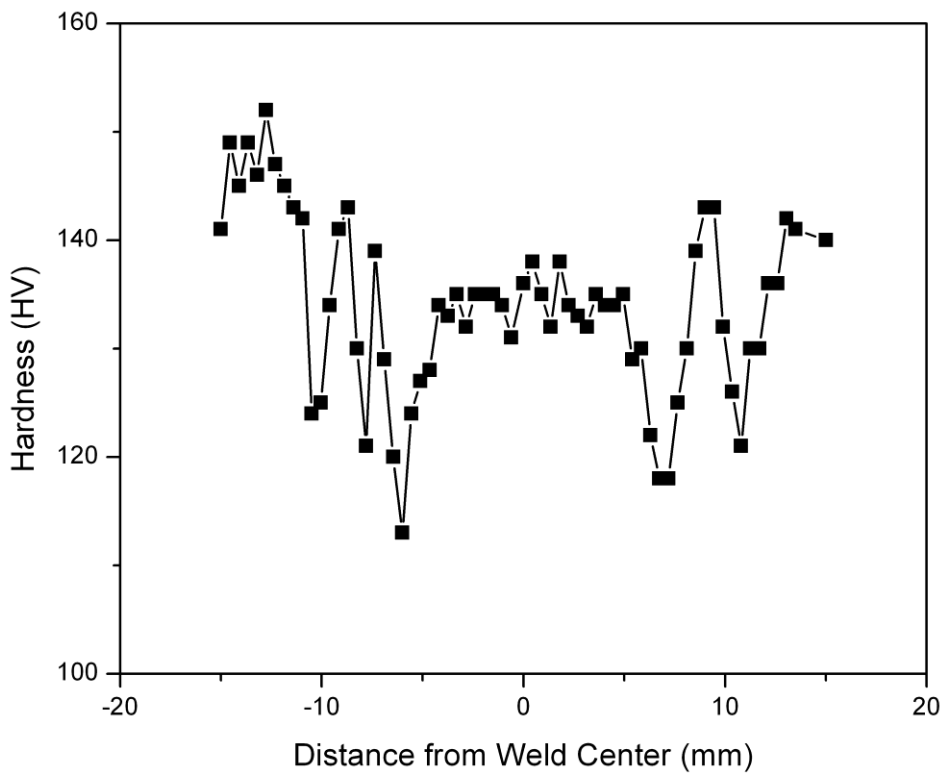


Figure 3.27 Hardness profile across the right of the center of CB-183-P1.

**3.2.3 Tensile Behavior.** Each subset test data table details the ultimate stress, plug size, PWHT condition, test temperature, the side of the panel tested with ARAMIS, discussed later in Section 3.2.4.3, location of failure and description of the physical appearance of the failure. All tensile statistical data was calculated using Excel 2010. Comparative data was calculated using a two-tailed  $t$  test.

**3.2.3.1 101.6 mm Samples.** Twelve 101.6 mm samples were tested at room temperature and in liquid nitrogen (-196°C) with a crosshead displacement of 1.27 mm/min. Subset 1 consisted of six samples containing M3 plugs tested at room temperature. Test data for subset 1 is listed in Table 3.5. Four samples had a post weld heat treatment (PWHT). One of the samples failed in the gripping bolt holes. The strength data from this sample was not included in the statistical evaluation. The average strength of the remaining samples was 360 MPa, with standard deviation of 18 MPa with a coefficient of variation of 4.9%. The PWHT samples had a higher ultimate stress than the non-PWHT samples. Five samples fractured on the retreating side with the exception of the sample failing in the gripping bolt holes.

Subset 2 consisted of six samples containing M5 plugs which were tested at room temperature at a crosshead displacement rate of 1.27 mm/min. Three samples had a post weld heat treatment (PWHT). Two of the samples failed in the gripping bolt holes. The strength data from these samples were not included in the statistical evaluation. Test data for subset 2 is listed in Table 3.6. The average strength of the remaining samples was 361 MPa, with a standard deviation of 7.0 MPa with a coefficient of variation of 1.9%. The PWHT samples had a higher ultimate stress higher than the non-PWHT samples which is consistent with the M3 plugs. This is consistent with the finding that PWHT samples are harder than non-PWHT samples discussed in 3.1.2. With the exception of the two samples that failed at the gripping bolt holes, the



remaining four fractured on the retreating side. The incorrectly machined sample failed at the lowest ultimate stress of 343 MPa.

Sample ID	Ultimate Stress (MPa)	Plug Size	PWHT	Temp	Test View	Location of Fracture	Fracture
CB-179-P1	371	M3	Y	RT	Minor	Bolts	Bolts
CB-179-P2	355	M3	N	RT	Major	Ret	Thru plug ragged
CB-179-P3	377	M3	Y	RT	Major	Ret	Clean thru the plug
CB-180-P1	340	M3	N	RT	Major	Ret	Thru plug ragged
CB-180-P2	380	M3	Y	RT	Major	Ret	Thru plug ragged
CB-181-P3	348	M3	Y	RT	Minor	Ret	Thru plug ragged

Table 3.5 101.6 mm samples with M3 plugs test data subset 1.

Sample ID	Ultimate Stress (MPa)	Plug Size	PWHT	Temp	Test View	Location of Fracture	Fracture
CB-183-P1	369	M5	Y	RT	Major	Ret	Clean around plug
CB-183-P2	356	M5	N	RT	Major	Ret	Thru plug ragged
CB-183-P3	377	M5	Y	RT	Minor	Bolts	Bolts
CB-184-P1	353	M5	N	RT	Major	Ret	Thru plug ragged
CB-184-P2	343	M5	Y	RT	Major	Bolts	Bolts
CB-184-P3	363	M5	N	RT	Minor	Ret	Thru plug ragged

Table 3.6 101.6 mm samples with M5 plugs test data subset 2.

The 3<sup>rd</sup> and 4<sup>th</sup> subsets contained five M3 and five M5 plugs, respectively. These samples were tested in LN<sub>2</sub> and exhibited higher ultimate strength in comparison to subsets 1 and 2 tested at room temperature. These subsets contained samples with and without PWHT cycles. The standard deviation and coefficient of variation were also lower for subsets 3 and 4 in comparison to subsets 1 and 2. Test data for subset 3 is listed in Table 3.7. The average ultimate

strength of the samples tested in LN<sub>2</sub> was 446 MPa, with a standard deviation of 9.5 MPa with a coefficient of variation of 2.1%. This is higher than 360 MPa for the samples tested at room temperature. Two samples in subset 3 were in the PWHT condition. Four of the samples fractured on the advancing side of the weld with three samples fracturing along the weld around the plug raggedly.

Test data for subset 4 is listed in Table 3.8. The average strength of the samples was 440 MPa, with a standard deviation of 7.09 MPa with a coefficient of variation of 1.6%. Three samples in subset 4 were in the PWHT condition with three fracturing on the advancing side with three fracturing clean around the plug and two fracturing along the weld around the plug.

Sample ID	Ultimate Stress (MPa)	Plug Size	PWHT	Temp	Location of Fracture	Fracture
CB-181-P1	454	M3	Y	LN <sub>2</sub>	Adv	thru weld around plug ragged
CB-181-P2	439	M3	N	LN <sub>2</sub>	Adv	along weld around plug ragged
CB-182-P1	442	M3	N	LN <sub>2</sub>	Adv	along weld around plug ragged
CB-182-P2	436	M3	Y	LN <sub>2</sub>	Adv	along weld around plug ragged
CB-182-P3	458	M3	N	LN <sub>2</sub>	Ret	thru weld around plug ragged

Table 3.7 101.6 mm samples with M3 plugs test data subset 3.

Sample ID	Ultimate Stress (MPa)	Plug Size	PWHT	Temp	Location of Fracture	Fracture
CB-185-P1	433	M5	Y	LN <sub>2</sub>	Adv	Clean around plug
CB-185-P3	442	M5	Y	LN <sub>2</sub>	Ret	Clean around plug
CB-186-P1	449	M5	N	LN <sub>2</sub>	Ret	along weld around plug ragged
CB-186-P2*	433	M5	Y	LN <sub>2</sub>	Adv	along weld around plug ragged
CB-186-P3	445	M5	N	LN <sub>2</sub>	Ret	Clean around plug

Table 3.8 101.6 mm samples with M5 plugs test data subset 4. \*Sample miss cut during machining smaller than other samples in sample set subset 4.

**3.2.3.2 215.9 mm Samples.** Eight samples were tested at room temperature at a crosshead displacement of 1.27 mm/min. Test data for subset 1, of the 215.9 mm wide M3 samples is listed in Table 3.9 with statistical data in Table 3.10. All samples are in the PWHT condition with a 1.7 MPa standard deviation and a 0.5% coefficient of variation. All samples fractured on the retreating side of the weld thru plug and plug with one sample showing a ragged plug.

Sample ID	Ultimate Stress (MPa)	Plug Size	PWHT	Temp	Test View	Location of Failure	Fracture
CX01-P2	375	M3	Y	RT	Major	Ret	Some plug showing \Thru Weld plug ragged
CX02-P2	379	M3	Y	RT	Major	Ret	Thru Weld plug ragged
CX03-P2	377	M3	Y	RT	Minor	Ret	Thru Weld plug ragged
CX04-P2	377	M3	Y	RT	Major	Ret	Thru Weld plug ragged

Table 3.9 215.9 mm samples with M3 plugs test data subset 1.

Test Results	Maximum	Minimum	Median	Mean	Std. Deviation	Coefficient of Variation (%)
Ultimate Strength (MPa)	379	375	377	377	1.7	.5

Table 3.10 215.9 mm samples with M3 plugs statistical data subset 1.

Test data for subset 2 of the 215.9 mm wide M5 samples, is listed in Table 3.11 with statistical data in Table 3.12. All samples are in the PWHT condition with a 13.8 MPa standard deviation and a 3.9% coefficient of variation. Two samples had flaws discovered during NDE located within the weld. The flaws are described in Appendix C.

Each sample with flaws fractured on the advancing side of the weld and the two samples with no flaw fractured on the retreating side similar to samples in subset 2. All 4 samples

fractured through the weld and plug. The standard deviation without the flawed samples is 3.1 MPa and a 0.8% coefficient of variation, which is closer to the statistical data of subset 1.

Sample ID	Ultimate Stress (MPa)	Plug Size	PWHT	Temp	Test View	Location of Failure	Fracture
CX07-P1	371	M5	Y	RT	Major	Ret	Thru Weld plug ragged
CX08-P1	349	M5	Y	RT	Major	Adv	Flaw detected Adv side/Broke through plug
CX09-P1	343	M5	Y	RT	Major	Adv	Flaw detected Adv side/Broke through plug
CX10-P1	367	M5	Y	RT	Minor	Ret	Thru Weld plug ragged

Table 3.11 215.9 mm samples with M5 plugs test data subset 2.

Test Results	Maximum	Minimum	Median	Mean	Std. Deviation	Coefficient of Variation (%)
Ultimate Strength (MPa)	371	343	358	358	13.8	3.9

Table 3.12 215.9 mm samples with M5 plugs test data subset 2.

Test Results	Maximum	Minimum	Median	Mean	Std. Deviation	Coefficient of Variation (%)
Ultimate Strength (MPa)	371	367	369	369	3.1	.8

Table 3.13 215.9 mm samples with M5 plugs test data subset 2 without samples with flaws.

**3.2.3.3 215.9 mm Overlap Samples.** The four overlap samples were tested at room temperature with a crosshead displacement of 1.27 mm /min. All samples fractured on the retreating side through the weld and plug with an irregular fracture surface. The samples had a standard deviation in strength of 4.5 MPa with a 1.3% coefficient of variation. The overlap samples have a lower ultimate stress of approximately 68.9 MPa than the standard 215.9 mm

samples. The process parameters (i.e., spindle speed) for the overlap samples were changed from the standard samples and the panels were not in the PWHT condition. Test data is listed in Table 3.14 with a statistical summary in Table 3.15.

Sample ID	Ultimate Stress (MPa)	Plug Size	PWHT	Temp	Test View	Location of Failure	Fracture
CIF37-P1	336	M3	N	RT	Major	Ret	Thru Weld plug ragged
CIF37-P2	329	M3	N	RT	Major	Ret	Thru Weld plug ragged
CIF38-P1	333	M3	N	RT	Major	Ret	Thru Weld plug ragged
CIF38-P2	339	M3	N	RT	Major	Ret	Thru Weld plug ragged

Table 3.14 215.9 mm overlap samples with M3 plugs test data subset 1.

Test Results	Maximum	Minimum	Median	Mean	Std. Deviation	Coefficient of Variation (%)
Ultimate Strength (MPa)	339	329	335	335	4.5	1.3

Table 3.15 215.9 mm overlap samples with M3 plugs statistical data subset 1.

**3.2.3.4 Comparative Tensile Data for All Samples.** A summary of all tensile test results is provided in Table 3.16. Statistical analysis was completed using a two-tailed  $t$  test showing no statistical difference between subsets of samples. At 95% probability, all subsets are compared in Table 3.17 to the 101.6 mm PWHT M3 samples tested at room temperature. Table 3.18 shows results for comparison of the only 215.9 mm sample result tested at room temperature. In Table 3.19 the statistical data for the 101.6 mm samples tested in LN<sub>2</sub> is shown. All samples were compared to the 101.6 mm PWHT M3 subset in the two-tail  $t$  test shown in Table 3.20.

The weld strength efficiency is defined in this study as the ratio of the initial weld to the plug welds omitting the 215.9 mm overlap panels which were that the welds with plugs have an average efficiency of 98.5%.

Sample Size	PWHT	Plug Size	Max. (MPa)	Min. (MPa)	Median (MPa)	Mean (MPa)	Std. Deviation (MPa)	Coefficient of Variation (%)	# in Subset
(a)101.6 mm	Y	M3	380	348	377	369	17.6	4.8	3
(b)101.6 mm	N	M3	355	340	347	347	10.3	2.9	2
(c)101.6 mm	Y	M5	369	369	-	-	-	-	1
(d)101.6 mm	N	M5	363	354	357	358	4.6	1.3	3
(e)215.9 mm	Y	M3	379	375	373	367	1.7	.5	4
(f)215.9 mm	Y	M5	371	343	358	358	13.8	3.9	4
(g)215.9 mm w/out flaws	Y	M5	372	367	369	369	3.1	.8	2
(h)215.9 mm overlap	N	M3	339	329	335	335	4.5	1.3	4

Table 3.16 Comparative statistical data for all samples at room temperature.

Degree of Freedom	Subset compared to	Calculated t value	95% significance*
3	(a)	1.866	3.18
4	(b)	1.047	2.78
5	(d)	0.233	2.57
5	(e)	0.933	2.57
3	(f)	0	3.18
5	(g)	3.82	2.57

Table 3.17 *t*-test comparative data with respect to PWHT 101.6 mm M3 samples at room temperature. \*Distribution of *t* table used from (Montgomery, 2009).

Degree of Freedom	Subset compared to	Calculated t value	95% significance*
6	(e)	1.29	2.45
4	(f)	1.077	2.78
6	(g)	13.43	2.45

Table 3.18 *t*-test comparative data with respect to PWHT 215.9 mm M3 samples at room temperature.

Sample Size	PWHT	Plug Size	Max. (MPa)	Min. (MPa)	Median (MPa)	Mean (MPa)	Std. Deviation (MPa)	Coefficient of Variation (%)	# in Subset
(i)101.6 mm	Y	M3	454	436	445	446	12.7	2.3	2
(j)101.6 mm	N		458	439	445	445	10.2	2.8	3
(k)101.6 mm	Y	M5	433	442	434	436	5.5	1.3	3
(l)101.6 mm	N		445	449	447	447	2.8	0.7	2

Table 3.19 Comparative statistical data for all samples in LN<sub>2</sub>.

Degree of Freedom	Subset compared to (i)	Calculated t value	9% significance*
3	(j)	0.099	3.18
3	(k)	1.27	3.18
2	(l)	.109	4.30

Table 3.20 *t*-test comparative data with respect to PWHT 101.6 mm M3 samples in LN<sub>2</sub>.

Sample Size	Plug Size	Average Ultimate Stress (MPa)	Weld Efficiency (%)
Initial	N/A	370	-
101.6 mm	M3	361	98%
101.6 mm	M5	360	97%
215.9 mm	M3	377	102%
215.9 mm	M5	358	97%

Table 3.21 Weld strength efficiency.

**3.2.4 Strain Data.** Strain data was collected by extensometer, strain gages and with ARAMIS to compare and determine the validity of the ARAMIS system. Strain data was collected on room temperature tests only. Data collected from a 50.8 mm extensometer was obtained by attaching the extensometer along the edge of the test panel, and the extensometer spanned the weld, heat affected zone and base metal. As such, it represents a composite measure of the deformation of the weld and base metal. Strain gages with a gage length of 6.35 mm were placed on the back of the panel at the top and bottom of the plug as shown in Figure 3.28. ARAMIS data was collected and averaged at various locations to compare to the extensometer and strain gage data.

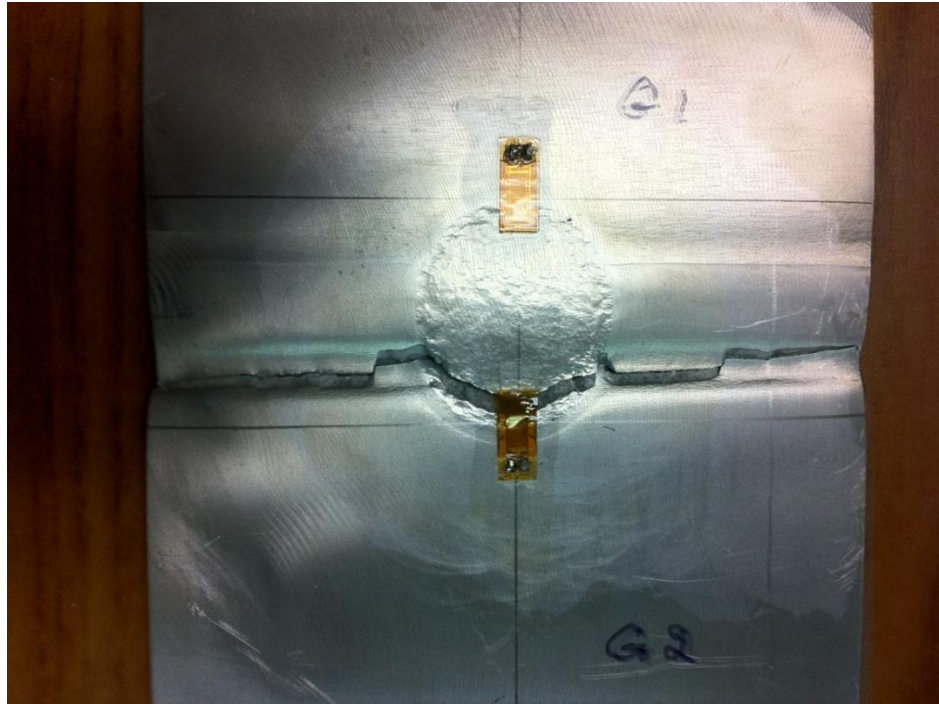


Figure 3.28 Placement of strain gages across major diameter of plug of specimen CB-181-P3.

**3.2.4.1 101.6 mm Samples.** Figure 3.29 shows the stress-strain curves of the extensometer data collected from samples containing M3 and M5 plugs. Seven of the panels responded in the same general manner. The linear elastic response and post yield response for samples were similar. CB-179-P1 and CB-183-P3 demonstrated a different linear response. These samples failed in the bolts. Failure in the bolts was likely the result of a non-uniform load distribution, which generated a non-uniform displacement field across the sample. In a non-uniform displacement field, the strain measured at one location will not match the strain measured at another location. Strain gage data was collected on four 101.6 mm panels. In three of the panels, strain gages were placed on the minor diameter side of the panels, and on the remaining panels, strain gages were placed on the major diameter side.



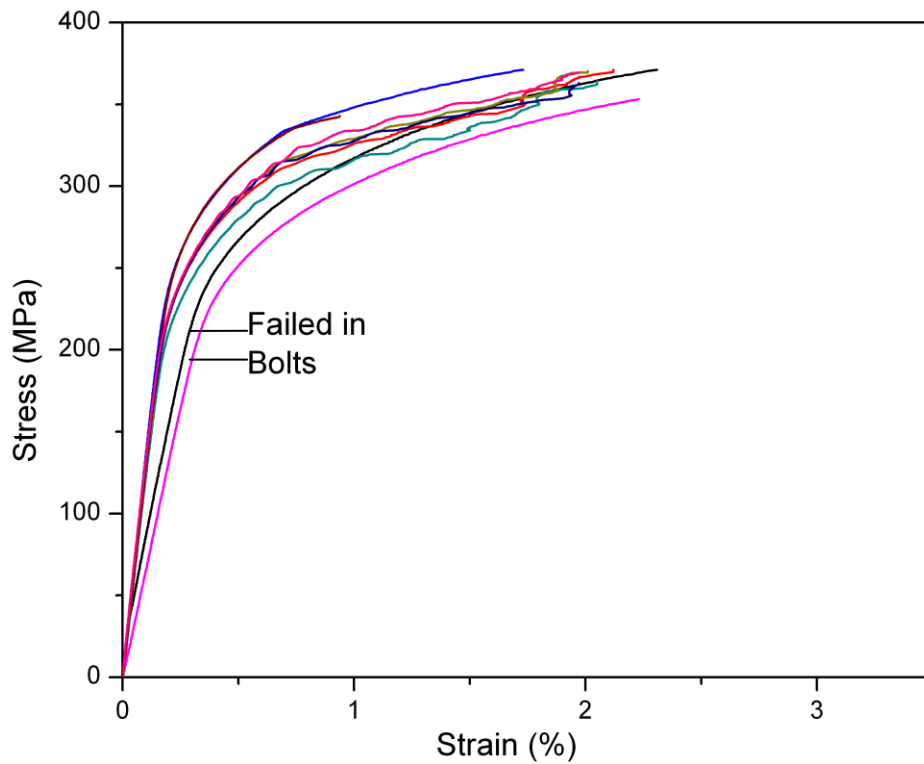


Figure 3.29 Extensometer strain data of 101.6 mm samples.

Figure 3.30 (A) shows the stress-strain curves for all four of the strain gages located at the top of the plugs and Figure 3.30 (B) shows the stress-strain curves for all four of the strain gages located at the bottom of the plugs. The variation in strain behavior represents the strain response of the major and minor side of the plug. The data indicate the major diameter yields before the minor diameter. This is likely due to the increased volume of the soft HAZ associated with the major diameter. Figure 3.31 (A) shows the stress-strain curves for all strain gages located on the minor side of the plug and Figure 3.31 (B) shows the stress-strain curves strain gages located on the major side of the plug.

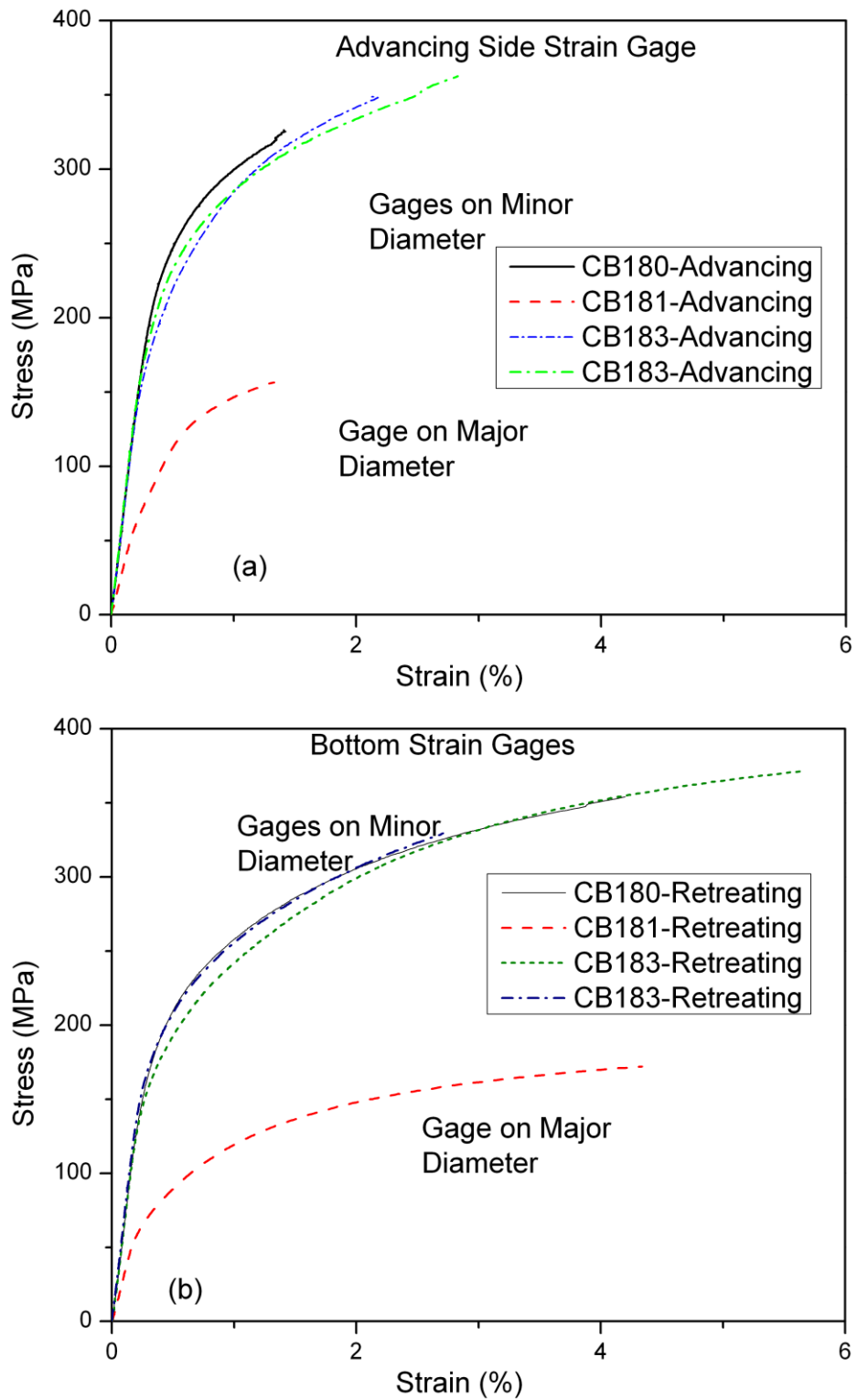


Figure 3.30 (A) Top strain gage and (B) bottom strain gage data of 101.6 mm samples.

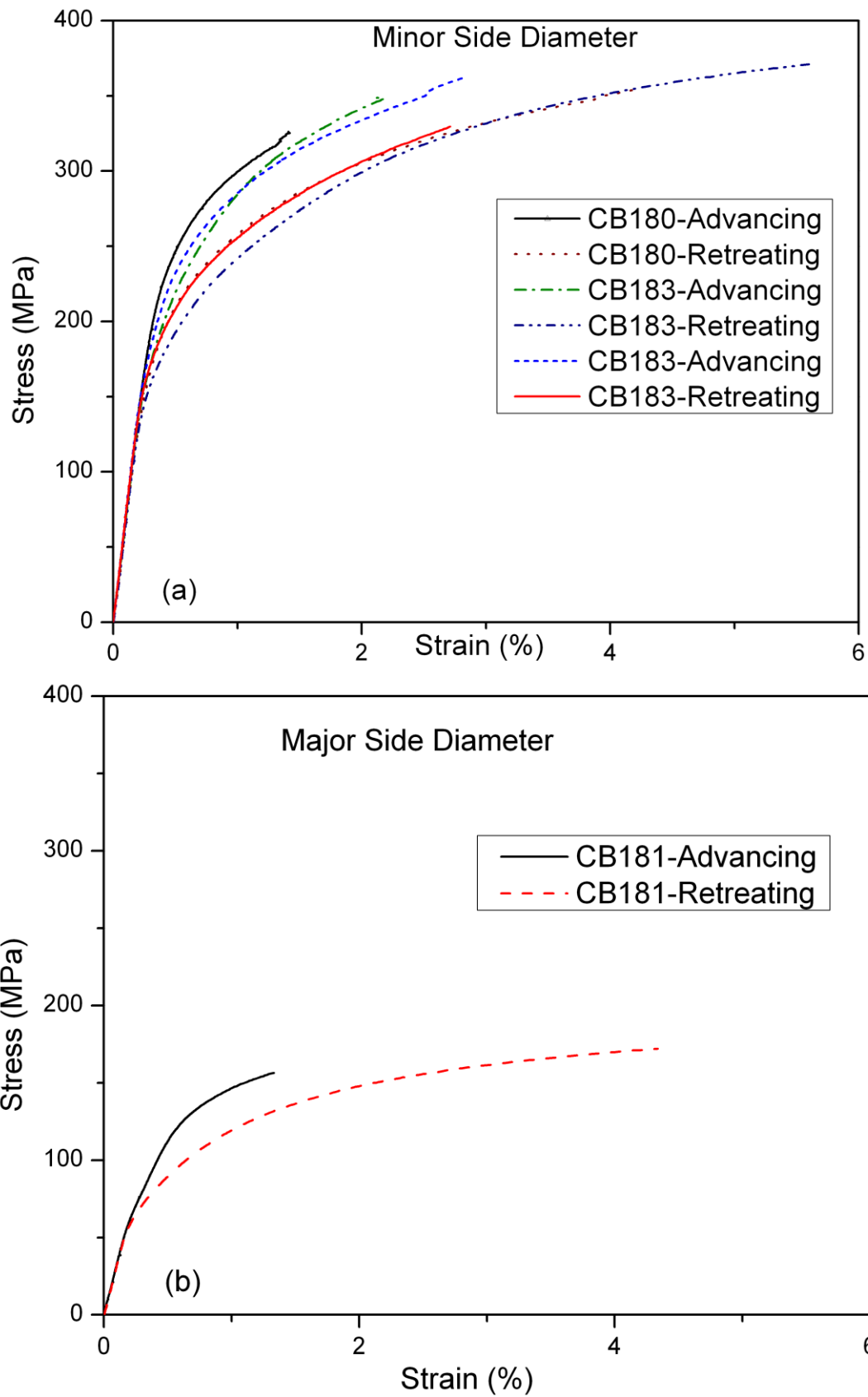


Figure 3.31 (A) Minor side and (B) major side strain gage data of 101.6 mm samples.

**3.2.4.2 215.9 mm Samples.** Figure 3.32 shows the stress-strain curves of external extensometer data collected on four samples. The behavior represents composite response of an initial weld, HAZ and base metal. Extensometer data and ARAMIS data was collected on the standard 215.9 mm samples and only ARAMIS data was collected on the 215.9 mm overlap panels.

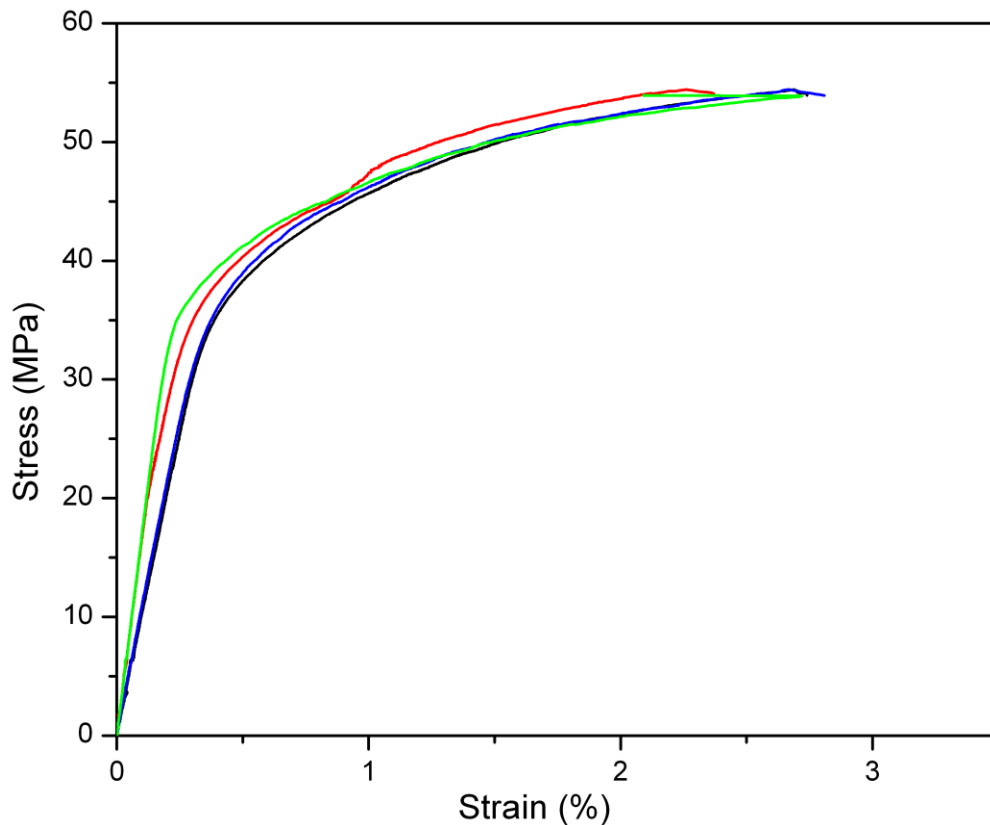


Figure 3.32 Extensometer strain data of 215.9 mm samples.

**3.2.4.3 ARAMIS Strain Data.** ARAMIS virtual gage length depends on facet size, facet step and strain length setting, as well as the field of view and pixel count. The minimum strain length setting is 3 facets. The facet size is the dimension in pixels of the square virtual gage areas. Figure 3.33 shows the facet (black outline) over the strain overlay. The solid red boxes are the starting point to resolving the complete facet field over the sample. From each starting point, facets are calibrated through each stage creating a complete facet field. At any area within

the facet field a point can be placed and strain data calculated at that point. The point lies at the center of the facet field.

Gage length can have a significant influence on reported strain values, particularly in the presence of strong local strain gradients (*Aramis User Manual-Software, 2007*).

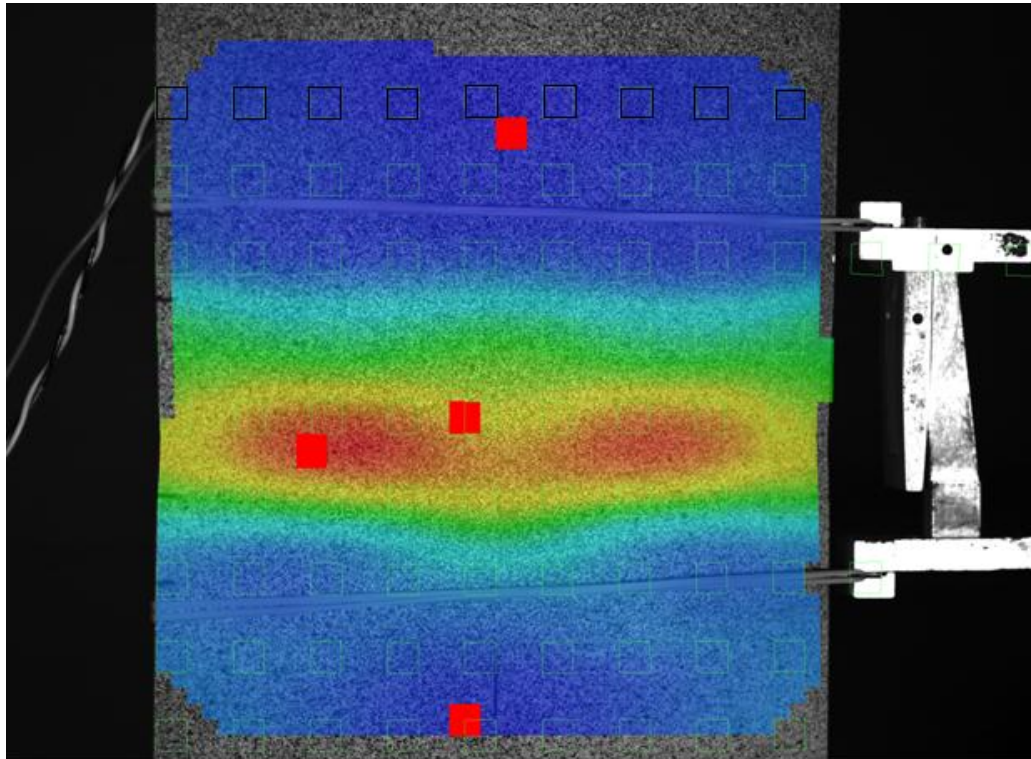


Figure 3.33 ARAMIS facet and strain overlay at failure showing extensometer placement.

In trying to compare ARAMIS to a mechanical strain gage, the first approach was to make the ARAMIS strain gage length match the mechanical gage length as closely as possible. The validity quote is the percentage of adjacent facets that must be valid for data to be displayed when computing strain or filtering. A validity of 55% was used, which represents a 3x3 matrix where at least 5 of the 8 surrounding facets must be valid or the center point cannot be used. Ten 13.11 mm virtual strain gages with a local facet field of 20 x 24 pixels were used in a vertical line between the two ends of the extensometer. The data was averaged and compared to the extensometer data. Figure 3.34 shows the extensometer data plotted with the ARAMIS data.

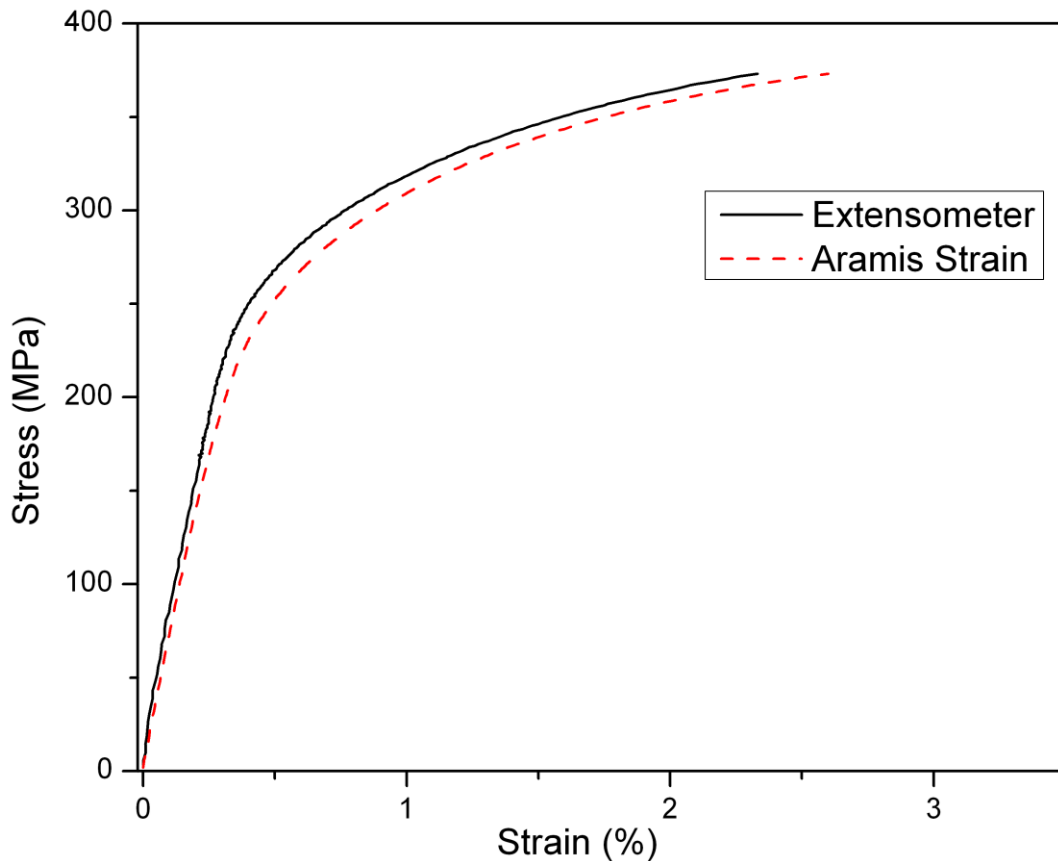


Figure 3.34 Extensometer versus ARAMIS strain data for CB-179-P1.

ARAMIS data was used to generate two 6.55 mm virtual strain gage with a local facet field of 66 x 48 pixels with a 55.0% validity quote. Strain was evaluated at the top and bottom of the plug. Figure 3.35 shows the ARAMIS based strain for the top and bottom of the plug. ARAMIS strain data and mechanical strain gage data are not comparable since the major side and minor side of the plug yields at different rates. The strain images from ARAMIS provide a look at strain development during testing with the visual representation of strain. Figure 3.36 shows the strain representation of CX03-P2 right before failure with an original strain gage length of 6.55 mm. There is an excess of strain located along the retreating side of the panel with delineation around the plug. The panel failed through the weld and through the plug.

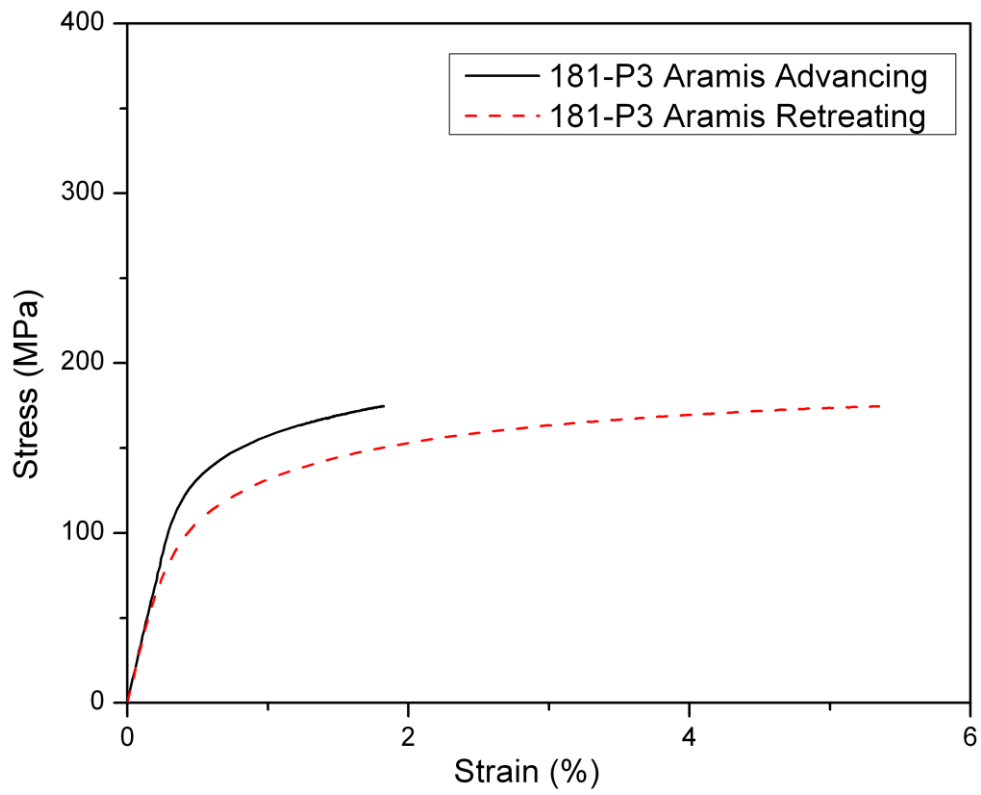


Figure 3.35 ARAMIS strain data for CB-181-P3 on the minor side.

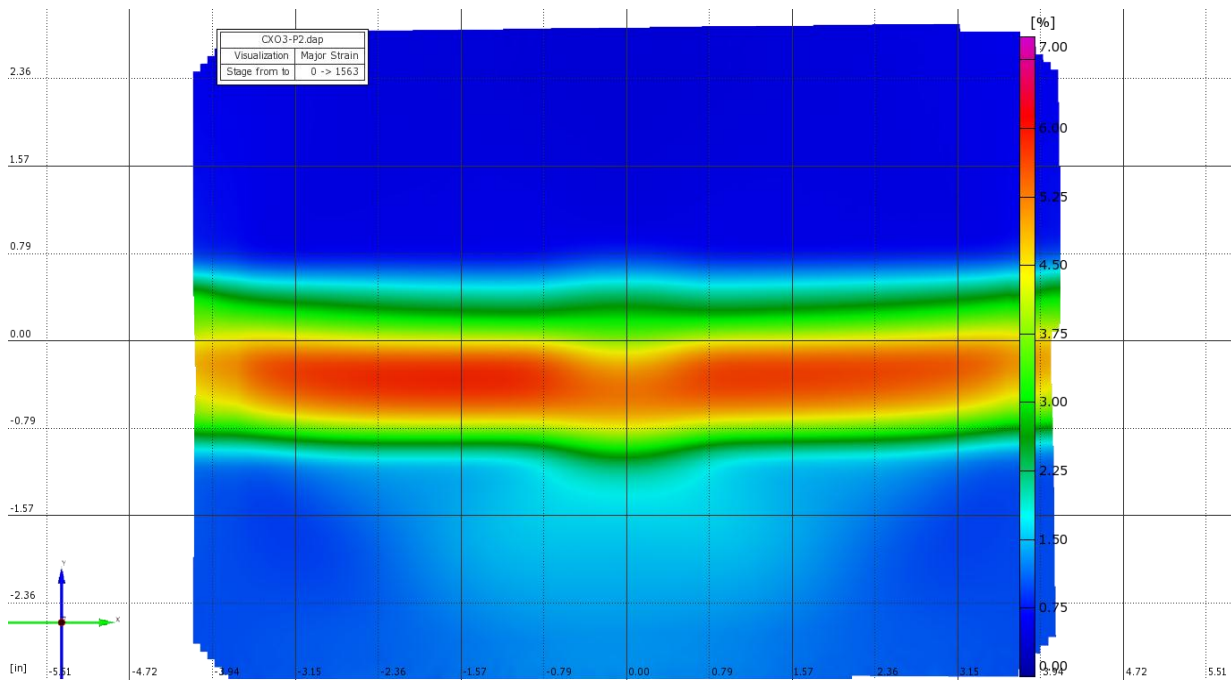


Figure 3.36 ARAMIS strain representation before failure.

**3.2.5 Fractography.** Optical microscopy of the weld after tensile testing was used to examine the fracture surface of the initial welds. Macroscopic images reveal a ductile fracture surface on the retreating side of the weld shown in Figure 3.37. A rough fracture surface is indicative of a bonded weld and plug. Figure 3.38 shows a very rough ductile surface on the surface of the plug fracture area. Figure 3.39 shows the fracture surface of a plug weld with little bond surface between the plug and the weld. This failure along the bond line between the plug and adjacent material may be indicative of improper surface treatment (cleaning) or inadequate processing parameters (spindle speed, pull force or machining tolerance deviations). Figure 3.40 shows the fracture surface of a weld which fractures along the retreating side of the weld and through the plug. The fracture surface is very rough. The fracture exhibits ductile fracture behavior and is shown in Figure 3.41.



Figure 3.37 Microscopy of bonded surface of weld and FPW.





Figure 3.38 Rough ductile surface on the surface of the plug fracture area of the sample that failed through the plug.



Figure 3.39 Fracture surface around plug with little or no bond to weld.

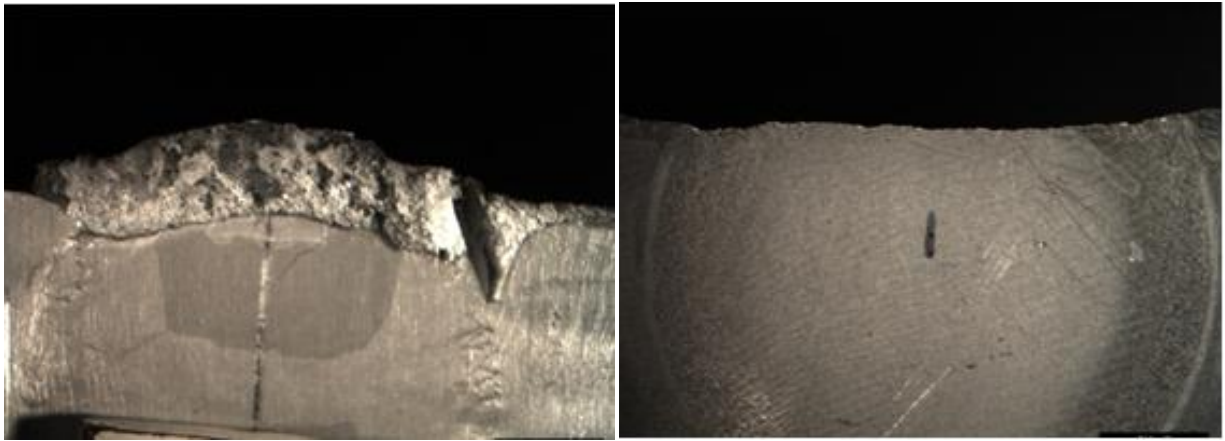


Figure 3.40 Rough fracture surface (A) ragged fracture with partial plug and (B) ragged fracture through the plug.



Figure 3.41 Ductile fracture surface of SR-FSW.

## Chapter 4 Summary

The initial weld microstructure analysis reveals

- fine grained nugget region with a sharp demarcation seen on the advancing side of the weld,
- a fairly diffused flow observed on the retreating side of the weld,
- a displaced weld seam from the advancing side past the thermo-mechanical affected zone (TMAZ) into the nugget region,
- the same hardness for the displaced material as the parent material,
- dynamic recrystallization was observed in the SR-FSW zone and the displaced weld seam region,
- a sharp increase in the hardness value within the nugget region with the samples that were PWHT showing an increase of 58% over the non-PWHT samples,
- and decreased hardness in the HAZ with a further decrease in hardness in the TMAZ.

Other characteristics and trends documented by category are:

Post weld heat treatment (PWHT):

- The PWHT strengths at room temperature are 13.8-20.7 MPa higher than the non-PWHT strength
- PWHT strengths are equal to non-PWHT at cryogenic temperature.
- Non-PWHT had a cryogenic strength enhancement approximately 59.2 MPa
- PWHT had a cryogenic strength enhancement of approximately 57.2 MPa in both the M3 and M5 plugs.

Welds strength data tested at room temperature:

- Initial welds had an average ultimate strength of 370 MPa.
- 101.6 mm M3 samples had an average ultimate strength of 361 MPa  
101.6 mm M5 samples had an average ultimate strength of 360 MPa.
- 215.9 mm M3 samples had an average ultimate strength of 377 MPa.
- 215.9 mm M5 samples had an average ultimate strength of 368 MPa
- 215.9 mm overlap M3 samples had an average ultimate strength of 334 MPa.

Weld Strengths comparison:

- Weld efficiency for the joints is computed by dividing the average ultimate strength of the tested joint by initial weld test joint:
  - 101.6 mm M3 samples had weld efficiency 98%
  - 101.6 mm M5 samples had weld efficiency 97%
  - 215.9 mm M3 samples had weld efficiency 102%
  - 215.9 mm M5 samples had weld efficiency 97%
- Within the subsets of data collected no major statistical significance in strength behavior was observed between the samples tested at room temperature except for the overlap panels which were processed differently than the other panels.
- There is a statistical difference between the data collected at room temperature and at LN<sub>2</sub>.

Failure analysis:

- All of the 215.9 mm samples and most of the 101.6 mm failed along the retreating edge (AA 2219 side) and through the plug instead of around the plug.
- Samples with flaw indications failed about 21 MPa below non-flawed samples. This is logical behavior, but points out the importance of NDE and the sensitivity of plugs to defects.

## ARAMIS analysis

- Strain accumulation was observed in the weld along the retreating side of the initial weld and around the plug.
- ARAMIS data in comparison to extensometer data shows acceptable comparison data.
- The ARAMIS strain data shows the major diameter of the plug yields before the minor diameter. This is a characteristic to the behavior shown with external electromechanical strain gages.

## Chapter 5 References

- Aluminum Alloy Properties. (2009). *Shelmet Precision Casting*. Retrieved from <http://www.shelmetcastings.com/aluminum-alloy-properties.html>
- Aramis User Manual-Software*. (2007). Germany: Gom mbH.
- Besnard, G., Hild, F., & Roux, S. (2006). “Finite-Element” Displacement Fields Analysis from Digital Images: Application to Portevin–LeChâtelier Bands. *Experimental Mechanics*, 46, 789-803.
- Brick, R. M., Gordan, R. B., & Phillips, A. (1965). *Structure and Properties of Alloys: The application of phase diagrams to interpretation and control of industrial alloy structures*: McGraw Hill.
- Cahn, R. W. (1996). Recovery and Recrystallization. In R. W. Cahn & P. Haasen (Eds.), *Physical Metallurgy* (pp. 2400-2500): Elsevier Science BV.
- Carter, R. W. (2004). United States Patent No. 6,758,382.
- Coletta, E. R. (New Orleans, LA), Cantrell, Mark A. (Pearl River, LA). (2002). United States Patent No. 6386419.
- Davis, J. R. (Ed.). (2004). *Tensile Testing*. Materials Park: ASM International.
- Genevois, C., Deschamps, A., Denquin, A., & Doisneau-Cottignies, B. (2005). Quantitative investigation of precipitation and mechanical behaviour for AA2024 friction stir welds. *Acta Materilia*, 53(8), 2447–2458. doi: 10.1016/j.actamat.2005.02.007.
- Handbook for Analytical Methods for Materials*. (2010). Plymouth: Materials Evaluation and Engineering, Inc.
- Hartley, P. J. (2008). Friction Plug Weld Repair for the Space Shuttle External Tank. Huntsville: NASA.
- Hassan, K. A. A., Norman, A. F., Price, D. A., & Prangnell, P. B. (2003). Stability of nugget zone grain structures in high strength Al-alloy friction stir welds during solution treatment. *Acta Materilia*, 51, 1923–1936. doi: 10.1016/S1359-6454(02)00598-0.
- Khaled, T. (2005). An Outsider looks at Friction Stir Welding (pp. 71). Lake Wood.

- Mahoney, M., Rhodes, C., Flintoff, J., Spurling, R. A., & Bingel, W. H. (1998). Properties of Friction-Stir-Welded 7075 T651 Aluminum. *Metallurgical Materials Transaction A*, 29A, 1955-1964.
- MATWEB. (2011a). Aluminum 2014-T6; 2014-T651 Retrieved May 9, 2011, from <http://www.matweb.com/search/DataSheet.aspx?MatGUID=e5de9f1161d34f71a34ae016723d097f>.
- MATWEB. (2011b). Aluminum T87 Retrieved May 9, 2011, from <http://www.matweb.com/search/DataSheet.aspx?MatGUID=86215ca4233a49fdb6b556235fc726b7>.
- McClure, J. (2005). An Investigation of Plug Welding 2195 Aluminum. Huntsville: NASA.
- Metz, D. F., Weishaupt, E. R., Barkey, M. E., & Fairbee, B. S. (2011). A Microstructure and Microhardness Characterization of Friction Plug Weld in Friction Stir Welded 2195 Al-Li. *ASME Journal of Engineering Materials and Technology*, In Press.
- Mishra, R. S., & Mahoney, M. W. (Eds.). (2007). *Friction Stir Welding and Processing*. Materials Park, OH: ASM International.
- Montgomery, D. C. (2009). *Design and Analysis of Experiments* (7th ed.). Hoboken, NJ: John Wiley & Sons.
- Murr, L. E., Trillo, E. A., Pappu, S., & Kennedy, C. (2002). Adiabatic shear bands and examples of their role in severe plastic deformation. *Journal of Materials Science*, 37(16), 3337-3360.
- Nabors, S. A. (2006). Tool for Two Types of Friction Stir Welding *NASA Tech Briefs*. Huntsville, Alabama: Marshall Space Flight Center.
- Oertelt, G., Babu, S., David, S., & Kenik, E. (2001). Effect of thermal cycling on friction stir welds of 2195 aluminum alloy. *Welding Research Supplement*, 71-79.
- Pantleon, W., Francke, D., & Kilmanek, P. (1996). Modelling adiabatic heating during high-speed deformation. *Computational Materials Science*, 7, 75-81.
- Parrington, R. J. (2002). Fractography of Metals and Plastics (Vol. 2(5), pp. 7): Practical Failure Analysis.
- Perez-Prado, M. T., Hines, J. A., & Vecchio, K. S. (2001). Microstructural evolution in adiabatic shear bands in Ta and Ta-W alloys. *Acta Materialia*, 2905-2917.
- Raj, K. H., Sharm, R. S., & Singh, P. (2010). Experimental Studies of Friction Stir Welding. *International Journal of Engineering Studies*, 2(3), 279-288.

- Reed-Hill, R. E., & Abbaschian, R. (1994). *Physical Metallurgy Principles* (3rd ed.). Boston, MA: PWS Publishing Company.
- Sato, Y. S., Park, S. H. C., Michiuchi, M., & Kokawa, H. (2004). Constitutional liquation during dissimilar friction stir welding of Al and Mg alloys. *Scripta Materialia*, 50(9), 1233-1236. doi: 10.1016/j.scriptamat.2004.02.002.
- Schmidt, T., Tyson, J., & Galanulis, K. (2003). Full-Field Dynamic Displacement and Strain Measurement Using Advanced 3D Image Correlation Photogrammetry. *Experimental Technology*, 27(4), 22-26.
- Schmidt, T., Tyson, J., Revilock, J., D. M., Padula II, S., Pereira, J. M., Melis, M., & Lyle, K. (2005). *Performance Verification of 3D Image Correlation Using Digital High-Speed Cameras*. Paper presented at the 2005 SEM Annual Conference, Portland.
- Schneider, J. A., Nunes, J. A. C., & Brendel, M. S. (2008). *The Influence of Friction Stir Weld Tool Form and Weld Parameters on Weld Structure and Properties: Nugget Bulge in Self-Reacting Friction Stir Welds*. Paper presented at the 8th International Symposium on Friction Stir Welding, MARTIM Seehotel Timmendorfer Strand, Germany.
- Shull, P. J. (2002). *Nondestructive Evaluation, Theory, Techniques and Applications*. New York, New York: Marcel Dekker, Inc.
- Somasekharan, A. C. (2005, May). Fundamental Study of Friction Stir Welding of Magnesium Alloys TO 6061-T6 Aluminum and FSW OF Dissimilar Magnesium Alloys
- Space Shuttle Technology Summary: Friction Stir Welding*. (2001). (Pub 8-1263). Huntsville, AL: Marshall Space Flight Center Retrieved from [http://www.nasa.gov/centers/marshall/pdf/104835main\\_friction.pdf](http://www.nasa.gov/centers/marshall/pdf/104835main_friction.pdf).
- Srinivasan, P. B., Arora, K. S., Dietzel, W., Pandey, S., & Schaper, M. K. (2010). Characterisation of microstructure, mechanical properties and corrosion behaviour of an AA2219 friction stir weldment. *Journal of Alloys and Compounds*, 492(1-2), 631-637. doi: 10.1016/j.jallcom.2009.11.198.
- Sullivan, A., & Robson, J. D. (2008). Microstructural properties of friction stir welded and post-weld heat-treated 7449 Aluminum alloy thick plate. *Materials Science and Engineering, A*, 351-360. doi: 10.1016/j.msea.2007.06.025
- Thomas, W. M., Nicholas, E. D., Needham, J. C., Murch, M. G., Templesmith, P., & Dawes, C. J. (1991). US Patent No. 5,460,317.
- Threadgill, P. L., Leonard, A. J., Shercliff, H. R., & Withers, P. J. (2009). Friction stir welding of aluminium alloys. *International Materials Review*, 54, 49-93.



## APPENDIX A BASE MATERIALS INFORMATION

	2219-T87	2014-T6
Density (lb/cu in)	0.103	0.101
Specific Gravity	2.84	2.8
Melting Point	643 °C	638 °C
Modulus of Elasticity	73.1 GPa	72.4 GPa
Shear Strength	280 MPa	290 MPa
Electrical Conductivity	30% of Cu	30% of Cu
Vickers Hardness	149	155
Fatigue Strength	103 MPa @# of Cycles 5.00e+8	124 MPa @# of Cycles 5.00e+8
Aluminum, Al	91.5 - 93.8 %	90.4 - 95.0 %
Chromium, Cr	--	<= 0.10 %
Copper, Cu	5.80 - 6.80 %	3.90 - 5.0 %
Iron, Fe	<= 0.30 %	<= 0.70 %
Magnesium, Mg	<= 0.020 %	0.20 - 0.80 %
Manganese, Mn	0.20 - 0.40 %	0.40 - 1.20 %
Other, each	<= 0.050 %	<= 0.050 %
Other, total	<= 0.15 %	<= 0.15 %
Silicon, Si	<= 0.20 %	0.50 - 1.20 %
Titanium, Ti	0.020 - 0.10 %	<= 0.15 %
Vanadium, V	0.050 - 0.15 %	--
Zinc, Zn	<= 0.10 %	<= 0.25 %
Zirconium, Zr	0.10 - 0.25 %	--

Table A1 Base Material Properties.

## APPENDIX B EXPERIMENTAL APPARATUS

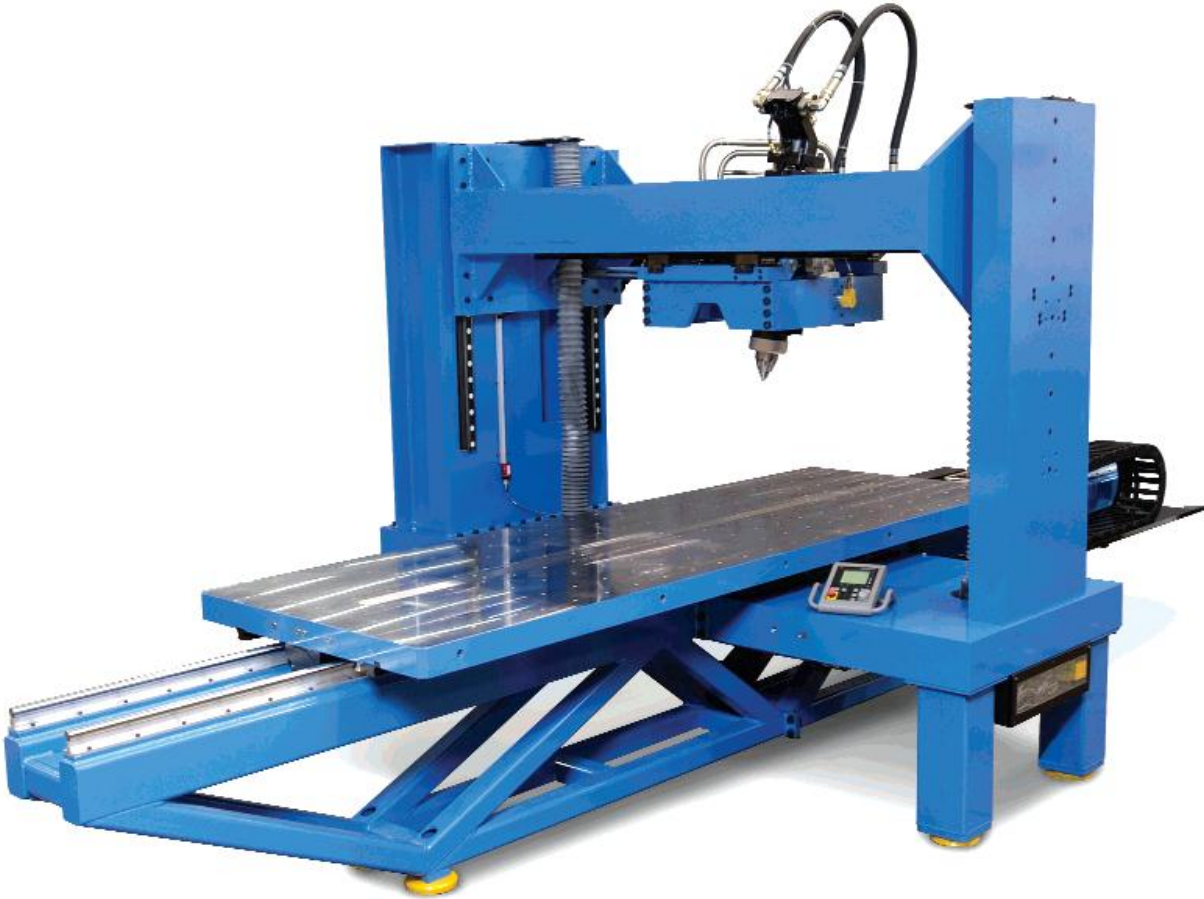


Figure B1 5-axis I-STIR Process Development System (PDS).



Figure B2 ARAMIS cameras used during testing.

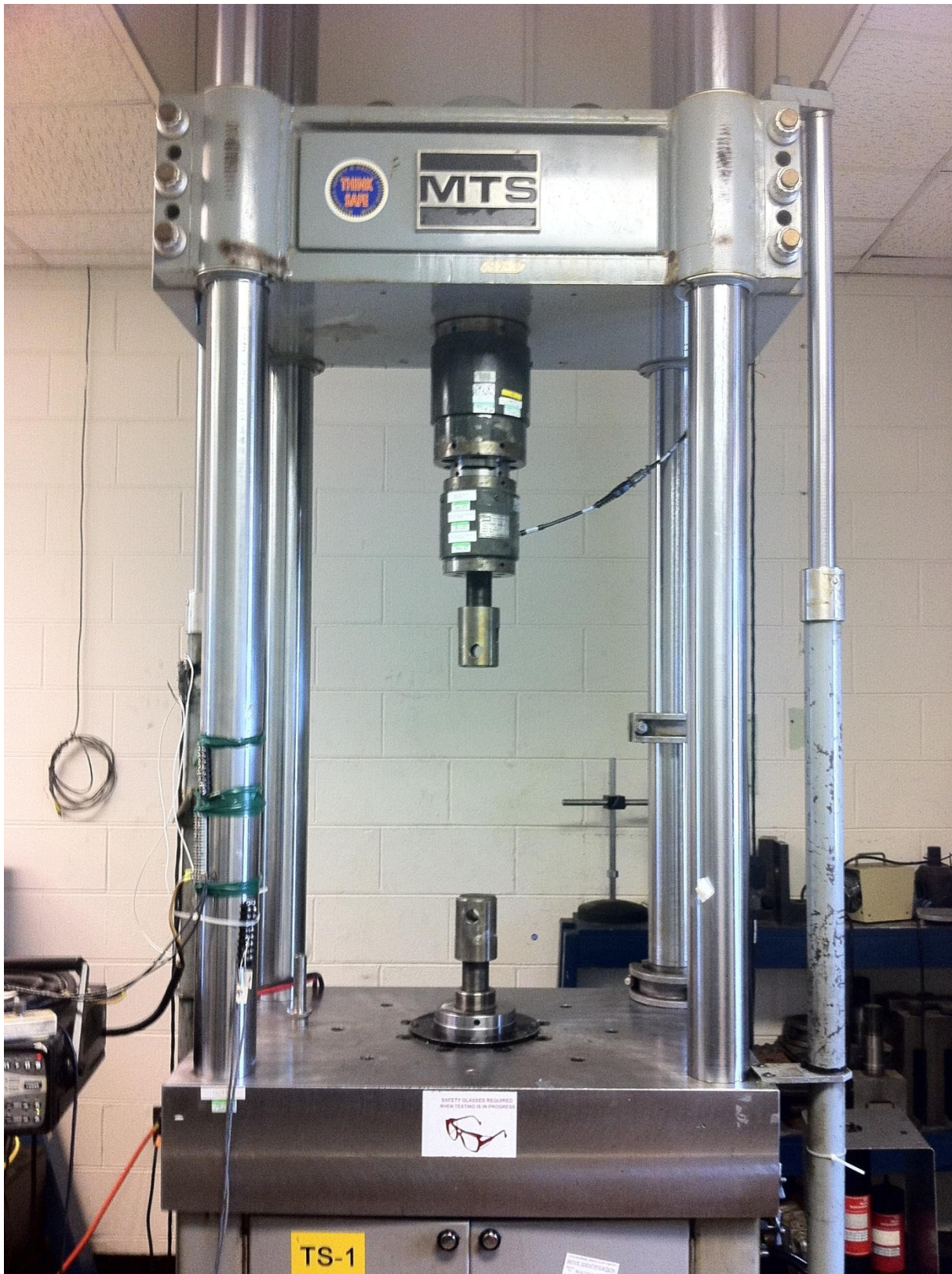


Figure B3 200K tensile test frame used during testing.

## **APPENDIX C NON DESTRUCTIVE EVALUATION IMAGES**

Inspection revealed four panels that exhibited a volumetric indication located on the advancing pin-tool area suggesting a defect in the advancing nugget bulge or a minor wormhole within the volume of the panel. One panel exhibited root flaws and one exhibited crown flaws. The flaws detected in the crown and root areas were undefined in type. The largest flaw reported was located within the weld approximately 5.59 mm from the advancing side of the weld. Flaw severities are reported as a percentage of reflected ultrasonic input energy returned to the transducer. A larger percentage indicates a more severe defect. One flaw had amplitude of 18.04% and was the longest detected in the 510.79 mm panels. This flaw is in 2/3 of the length of the weld. Other samples produced volumetric flaws of 10.98% and 15.59% as shown in Table 3.1. All flaws were found in the 215.9 mm samples. No flaws were detected by phased array ultrasonic inspections of the initial welds in the 215.9 mm overlap samples or the 101.6 mm wide samples. Output of ultrasonic inspection is shown in Figures C1-C3.

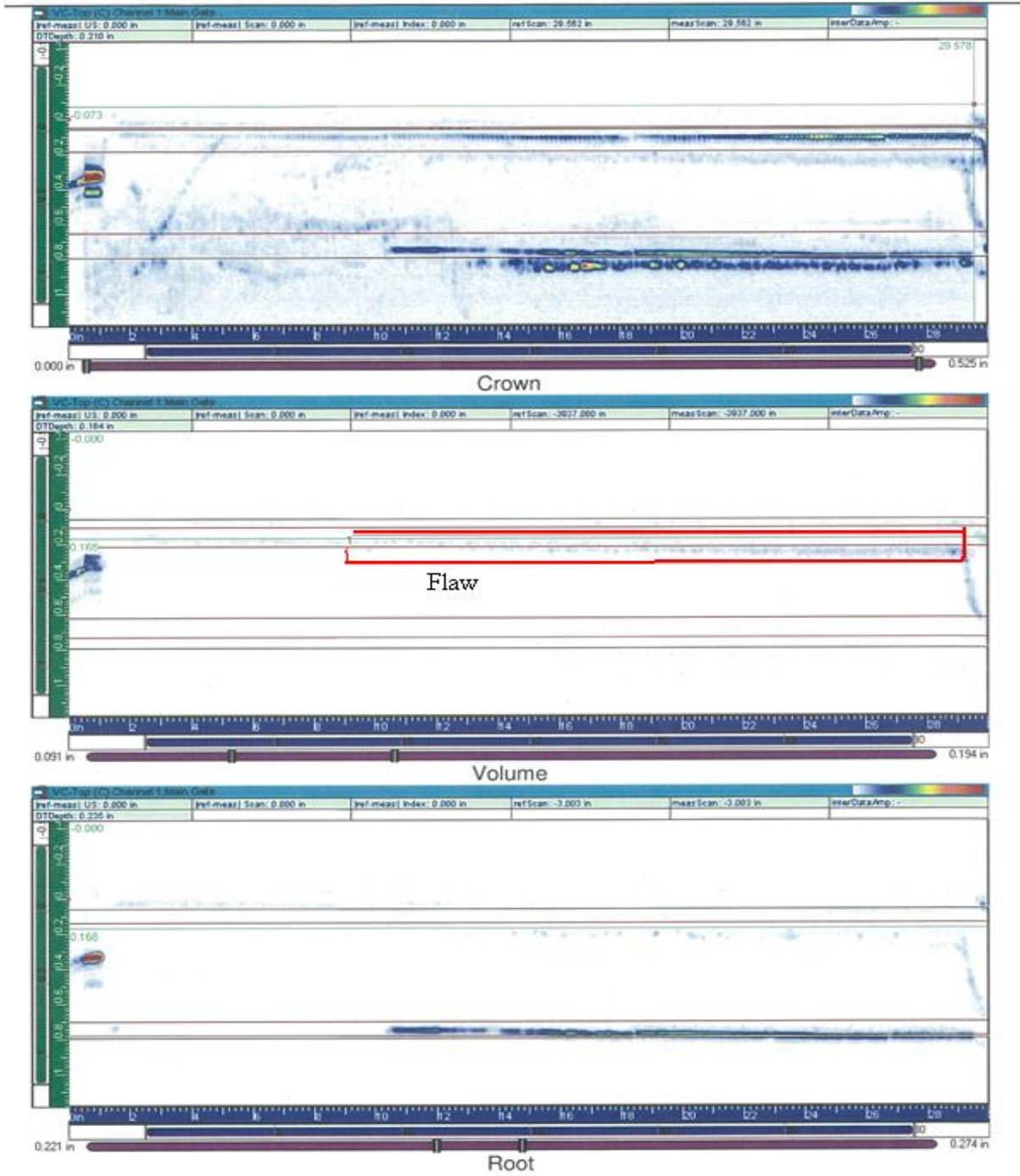


Figure C1 Phased array ultrasonic inspection output showing flaw in the volume of the weld shown. No flaw in the root or crown was detected.

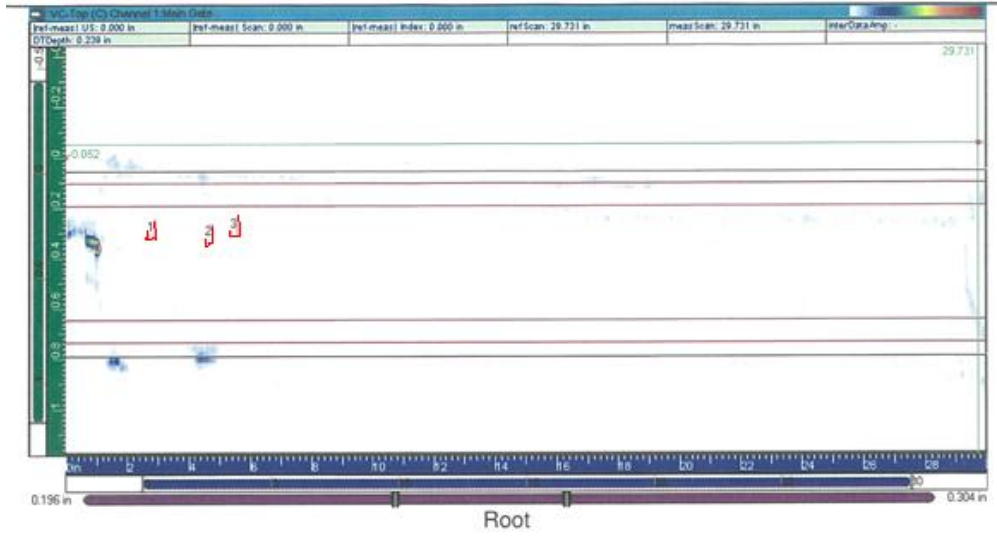


Figure C2 Phased array ultrasonic inspection output showing flaws in the root of the weld.

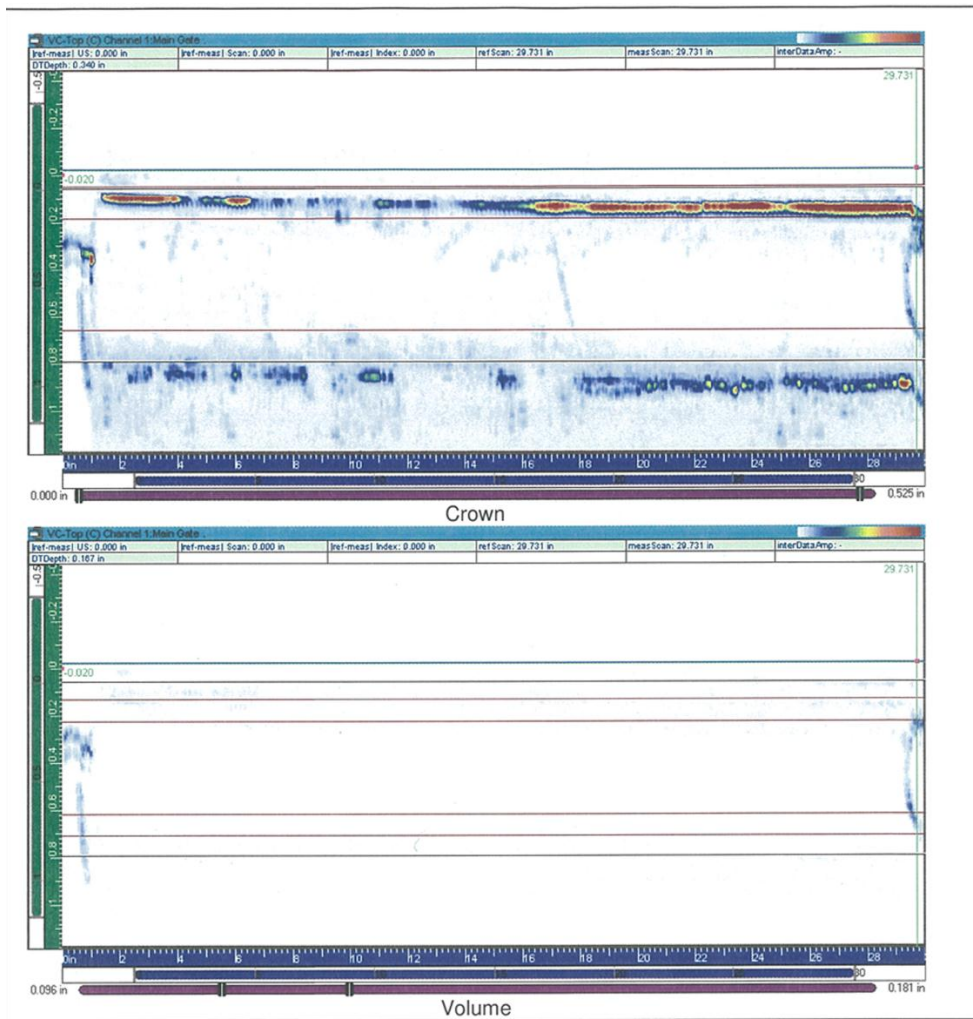


Figure C3 Phased array ultrasonic inspection output showing no flaws in crown or volume.

Figure C4 is a photograph of the round indications measuring 0.508 mm in diameter located in the lower quadrant of the plug. Figure C5 shows several round indications measuring less than 0.254 mm in diameter. Note in Figure C5 the indications lie along the periphery of the plug interface. These indicate a potential lack of fusion at the plug interface which could reduce the strength capability of the plug weld. Figure C6 shows images of no indications on the crown side and Figure C7 shows images of three plug inspections with no indications.



Figure C4 Round indications located lower left quadrant of the plug.





Figure C5 Round indications marked with red marks.



Figure C6 Image showing no indications on the crown side.

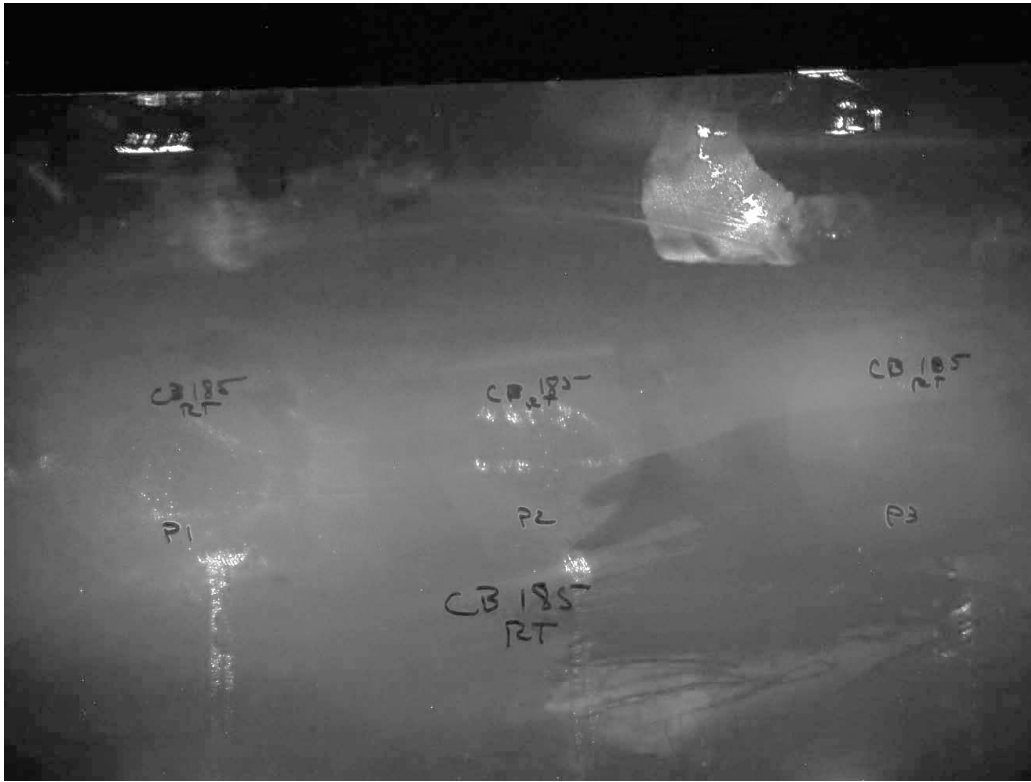


Figure C7 Image showing no indications on the root side.

Eddy current testing indicated a sharp conductivity difference or change observed on the minor side of the plug welds at the friction stir weld to plug weld interface on the overlap panels. The indication produced a response similar in appearance to crack-like indications but not as sharply defined. Figure C8 shows the snapshot image of the screen displaying a slight increase in impedance observed in the plug weld HAZ noted on the crown advancing side of the 215.9 mm sample. Figure C9 shows the snapshot image of the screen displaying no impedance change on the crown retreating side.

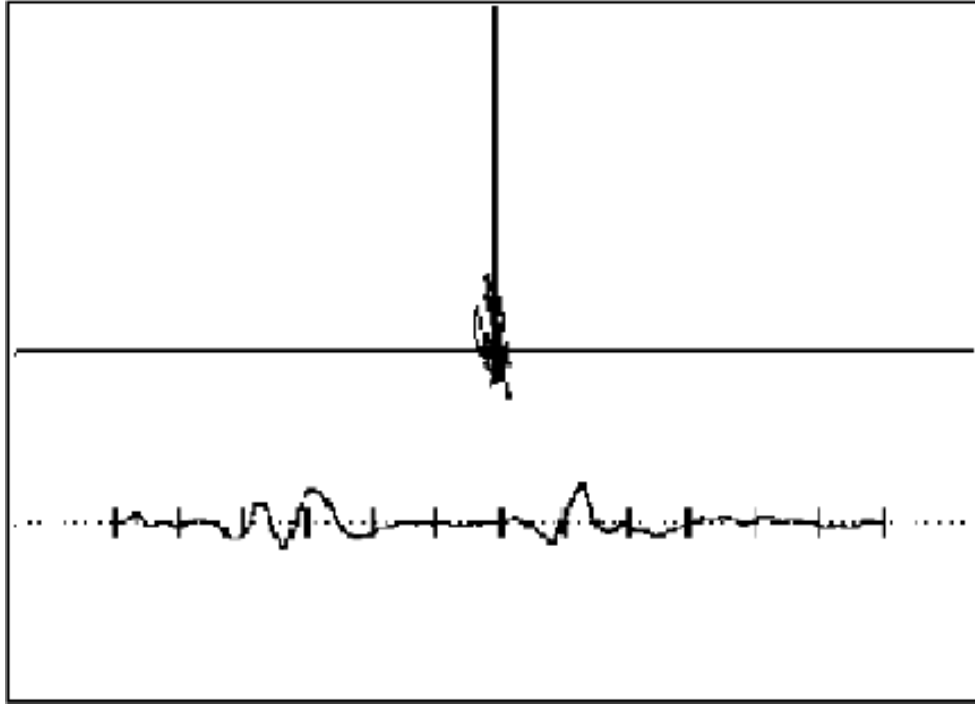


Figure C8 Snapshot of screen displaying Eddy current response in the plug weld HAZ on the crown advancing side. Note slight impedance change.

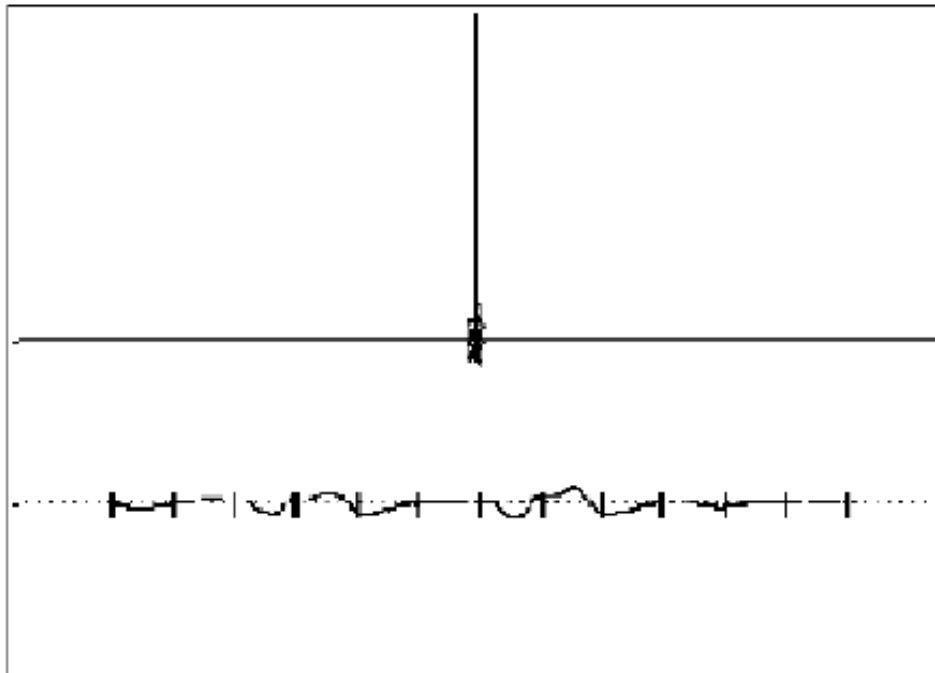


Figure C9 Snapshot of screen displaying Eddy current response in the plug weld HAZ on the crown retreating side. Note no impedance change.

## CURRICULUM VITAE

**K. Renee Horton (US Citizen)**

4016 SW Hunters Ridge Dr, Huntsville, AL 35802

Email: krhorton@alumni.lsu.edu / Phone: (225)939-9526

---

### EDUCATION:

University of Alabama

Tuscaloosa, AL

**PhD Candidate Material Science** – 3.33/4.0 GPA

Jan 2005 – Present

Fundamental study of self-reacting friction stir weld dissimilar aluminum alloys and the friction Plug weld in order to understand the fundamental mechanism and interaction of the materials

Louisiana State University (LSU)

Baton Rouge, LA

**Bachelor of Science, Electrical Engineering** - 2.8/4.0 GPA

May 2002

Area of Concentration: Chip layout design

### PROFESSIONAL EXPERIENCE

**Harriet G. Jenkins Predoctoral Fellow in Residence Marshall Space Flight Center**

Huntsville, AL

Aug 2010 – Present

Fundamental study of self-reacting friction stir weld dissimilar aluminum alloys and the friction plug weld in order to understand the fundamental mechanism and interaction of the materials. Responsible for providing guidance on testing methods and procedures to evaluate alloys welded. Study consists of samples tested with a 3D image correlation system to further investigate strain patterns under tensile testing.

2010 NASA Leadership Academy at Marshall Space Flight Center - Summer Internship

Huntsville, AL

**Research Associate**

May 2010 – Aug 2010

Individual project under Principle Investigator Tina W. Malone that was assigned the task of investigating the 3D deformation and strain at the interface of the friction stir weld and the plug weld using the Aramis image correlation system. Reviews project test plan to define test approach, instrumentation needs, and test fixtures requirements.

Materials for Information Technology Center, University of Alabama

Tuscaloosa, AL

**Graduate Research Associate**

Aug 2005-May 2010

Research conducted under the supervision of J.W. Harrell and Martin Bakker concentrating on growing and characterizing hexagonal closed packed CoCrPt films with a vertical composition gradient and characterizing the effect of the gradient on magnetic switching and thermal stability. To magnetically characterize the films, they must be patterned to suppress multi-domain switching behavior

Dept of Physics, University of Alabama  
**Graduate Teaching Associate**

Tuscaloosa, AL  
Jan 2007-May 2009

Center for Advanced Microstructures and Devices, Louisiana State University

Baton Rouge, LA  
Aug 2003-Dec 2004

**Graduate Research Associate**

Research conducted under the supervision of Dr. Henry at Southern University consisting of investigation of magnetic properties of annealed cobalt nobel Metal shell nanoparticles for GMR Sensors using a superconducting quantum interference device (SQUID) magnetometer.

National Center for Renewable Energy

Boulder, CO  
May 2003-Aug 2003

**Research Associate**

Research consisted of controlling the finished gas and byproduct ratios by altering the initial biomass inputs.

**PROJECT EXPERIENCE:**

**CoCrPt Thin Films used to Extending the Superparamagnetic Limit of Recording Media (UA):** Research concentrates on growing and characterizing hexagonal closed packed CoCrPt films with a vertical composition gradient and characterizing the effect of the gradient on magnetic switching and thermal stability. To magnetically characterize the films, they must be patterned to suppress multi-domain switching behavior.

**Development of a 5 Sputtering gun High Vacuum Deposition System (UA):** Work completed under the supervision of Dr. Gary Mankey. Design, construction and implementation of a 5 sputter gun, with sample interlock exchange system used to sputter deposit thin films. System was designed to reach vacuum levels of  $10^{-8}$  with a rotary pump and a cyro pump. System also included a system to monitor deposition, shutters and viewing ports for monitoring.

**Synthesis and Characterization of Magnetically Manipulated CdSe Quantum Dots and Rods(UA):** Synthesis of CdSe, CdTe and CdS quantum dots used for magnetic manipulation. Characterization completed with XRD, absorption and florescence methods. Assist other research assistants with characterization of synthesized particles.

**SKILLS**

**SOFTWARE:** Microsoft Office, Mathcad, Autocad, Labview, Orginlab, MuPad pro, Scientific Workplace, Adobe Design Standard and Maple, Aramis

**EQUIPMENT:** Phillips and Rigaku X-ray diffraction equipment, Scanning Electron Microscopy, Transmission Electron Microscopy, Optical Microscopy, Tensile Test Machinery, SQUID Magnetometer, Vibrating Sample Magnetometer, Alternating Gradient Magnetometer, Thin Film Deposition Systems and Aramis 3D Image Correlation system

**Fellowships and Awards**

- Goddard Space Flight Center Graduate Student Research Program (GSRP) Fellowship 2004-2007. Includes a \$3000 supply and \$3000 travel budget.

- Southern Regional Educational Board (SREB) Fellowship 2005-2008
- Community Based Partnership Student initiated outreach award \$2000 (2008)
- National Alumni Fellow University of Alabama 2008-2009
- Harriet G. Jenkins Predoctoral Fellowship 2008-2011
- Co-PI NSF grant PHY-0824634 for \$138,180.00 2008
- Argonne National Laboratory Center for Nanoscale Materials User Proposal approved 2010

### **Professional Service:**

- Program Committee (2004 - Present) ; Chair of Women in Physics Committee (2007-Present): Member National Society of Black Physicists
- Member of the 2005 US Delegation Team for the 2nd IUPAP Conf on Women in Physics (2005). Co-Leader US Delegation Team for the 3<sup>rd</sup> IUUPAP WIP (2008)
- AL and GA Science and Everyday Experience coordinator (2007-2009): Delta Sigma Theta Sorority, Inc

### **Presentations**

- K. Renee Horton (2009) Invited. Extending the Superparamagnetic Limit. University of Mississippi, March 3, 2009
- K. Renee Horton (2009) Invited "ICWIP 2008 Report", The Physics Diversity Summit and the Joint Annual Conference of the National Society of Black Physicist and National Society of Hispanic Physicists. Nashville, TN, February 2009
- K. Renee Horton (2008) Invited. Creating a viable Woman's working Group. 3<sup>rd</sup> IUPAP WIP conference. Seoul, Korea
- K. Renee Horton (2008) Invited. Commencement/Founder's day speaker University of Maryland Eastern Shores, Sept. 16, 2008
- K. Renee Horton (2008) Invited. The Eye of the Storm: Balancing my storm of family, career and self. American Physical Society March Meeting. March 11, 2008
- K. Renee Horton (2006). Magnetically Manipulated Quantum Dots (MMQD). NASA Goddard Space Flight Center (GSFC) Graduate Student Research Program Symposium (GSRP). September 22, 2006
- K. Renee Horton (2006). Invited. Women Physicist of color achieving at the intersection of race and gender. American Physical Society March Meeting. March 15, 2006.
- K. Renee Horton (2006). Invited. NSBP International Activities – 2<sup>nd</sup> IUPAP International Conference on Women in Physics in Rio de Janeiro, Brazil. February 18, 2006.
- K. Renee Horton (2004). Invited. Outreach Opportunities in Renewable Energy. Renewable Energy Academic Partnership (REAP) Conference, Coca, FL, August 13, 2004

### **Poster Presentations**

- K. Renee Horton, S. Kang, G. Mankey and J.W. Harrell (2008) Anisotropy Graded Media: Extending the superparamagnetic limit. <sup>(1)</sup>IEEE Magnetics Summer School, Colorado Springs, CO. August 3-8: <sup>(2)</sup>3<sup>rd</sup> IUPAP International Conference on Women in Physics, Seoul, Korea. October 10-12. <sup>(3)</sup>University of Alabama, Materials for Information Technology (MINT) Fall Review. October 12-14, 2008
- K. Renee Horton and J.W. Harrell (2008) Anisotropy Graded Media. Marie Currie PSK-I Surface Interaction Summer School, Costa Brava, Spain. May 12-15.

- K. Renee Horton (2006). Evolution of the MINT Scientific Outreach Program (MINT SOUP) University of Alabama, Materials for Information Technology (MINT) Fall Review. October 22-24, 2006
- K. Renee Horton (2006). Synthesis and Characterization of CdSe-Co Core-Shell Quantum Dots and Rods. University of Alabama, Materials for Information Technology (MINT) Fall Review. October 22-24, 2006
- K. Renee Horton (2005). Women Physicist of color achieving at the intersection of race and gender. Poster- 2<sup>nd</sup> IUPAP International Conference on Women in Physics in Rio de Janeiro, Brazil. May 24, 2005
- K. Renee Horton (2004). Investigation of Magnetic Properties of Annealed Cobalt Nobel Metal shell Nanoparticles for GMR Sensors – NASA Goddard Space Flight Center (GSFC) Graduate Student Research Program Symposium (GSRP). September 22, 2004